

อุปกรณ์แทรกสนามแม่เหล็กความเข้มสูงสำหรับวงกักเก็บอิเล็กตรอน  
พลังงานต่ำ

นางสาวสมใจ ชื่นเจริญ

วิทยานิพนธ์นี้เป็นส่วนหนึ่งของการศึกษาตามหลักสูตรปริญญาวิทยาศาสตรดุษฎีบัณฑิต  
สาขาวิชาฟิสิกส์  
มหาวิทยาลัยเทคโนโลยีสุรนารี  
ปีการศึกษา 2552

**HIGH FIELD INSERTION DEVICES FOR  
LOW ENERGY ELECTRON STORAGE  
RINGS**

**Somjai Chunjarean**

**A Thesis Submitted in Partial Fulfillment of the Requirements for the  
Degree of Doctor of Philosophy in Physics  
Suranaree University of Technology  
Academic Year 2009**

# HIGH FIELD INSERTION DEVICES FOR LOW ENERGY ELECTRON STORAGE RINGS

Suranaree University of Technology has approved this thesis submitted in partial fulfillment of the requirements for the Degree of Doctor of Philosophy.

Thesis Examining Committee

---

(Asst. Prof. Dr. Chinorat Kobdaj)

Chairperson

---

(Dr. Saroj Rujirawat)

Member (Thesis Advisor)

---

(Prof. Dr. Helmut Wiedemann)

Member

---

(Asst. Prof. Dr. Chitrlada Thongbai)

Member

---

(Dr. Somsak Dangtip)

Member

---

(Prof. Dr. Sukit Limpijumnong)

Vice Rector of Academic Affairs

---

(Assoc. Prof. Dr. Prapun Manyum)

Dean of Institute of Science

สนใจ ชื่นเจริญ : อุปกรณ์แทรกสนามแม่เหล็กความเข้มสูงสำหรับวงกักเก็บอิเล็กตรอน  
พลังงานต่ำ (HIGH FIELD INSERTION DEVICES FOR LOW ENERGY  
ELECTRON STORAGE RINGS) อาจารย์ที่ปรึกษา : ดร. สาโรช รุจิรพรรณ,  
166 หน้า.

อุปกรณ์แทรกที่ใช้ทั่วไปได้แก่ วิกเกิลอร์ (Wiggler) Wave-Length Shifter (WLS) และ อันดูลเตอร์แม่เหล็กถาวร (Permanent Undulator) เพื่อเป็นแหล่งกำเนิดแสงซินโครตรอนที่มีค่าพลังงานโฟตอนที่สูงและค่าความสว่างที่สูงมากเมื่อเทียบกับแสงซินโครตรอนที่ปลดปล่อยจากสนามแม่เหล็กสองขั้ว และเนื่องจากการแทรกสอดกันของแสงที่ถูกปลดปล่อยมาจากอิเล็กตรอนที่เคลื่อนที่ในสนามอันดูลเตอร์ในแต่ละครั้งนั้น ทำให้แสงมีความสว่างมากกว่าอุปกรณ์แทรกชนิดอื่น อย่างไรก็ตาม อันดูลเตอร์แม่เหล็กถาวรไม่สามารถผลิตแสงซินโครตรอนที่มีค่าพลังงานโฟตอนในย่านรังสีเอ็กซ์สำหรับวงแหวนกักเก็บอิเล็กตรอนพลังงานต่ำที่ 1.2 GeV ดังนั้นจึงมีความต้องการอันดูลเตอร์แบบตัวนำยิ่งยวด (Superconducting Undulator, SCU) ที่มีความยาวคาบสั้นมากและสนามแม่เหล็กความเข้มสูง เพื่อผลิตแสงซินโครตรอนที่ฮาร์โมนิกสูงๆ ประมาณฮาร์โมนิกที่ 7 เป็นต้นไป อย่างไรก็ตาม ทั้งอันดูลเตอร์แม่เหล็กถาวรและอันดูลเตอร์แบบตัวนำยิ่งยวดจะให้แสงซินโครตรอนที่มีความสว่างมากก็ต่อเมื่อค่าความผิดเพี้ยนของสนามแม่เหล็ก และความยาวคาบหรือเฟส (จากความต่างของระยะทางที่อิเล็กตรอนที่เคลื่อนที่ได้ในแต่ละคาบ) มีค่าน้อยมาก เทียบเท่ากับค่าสนามแม่เหล็กในอุดมคติ เนื่องจากวิธีการ shimming ที่ใช้กับอันดูลเตอร์แม่เหล็กถาวรเพื่อแก้ความผิดเพี้ยนของสนามแม่เหล็กโดยใช้ชิ้นเหล็กวางประกบบนแม่เหล็กที่อุณหภูมิห้องไม่สามารถแก้ความผิดเพี้ยนค่าสนามและความยาวคาบของสนามแม่เหล็กอันดูลเตอร์แบบตัวนำยิ่งยวด ดังนั้นการใช้ขดลวดของตัวนำยิ่งยวด (Correction Coil) พันรอบๆ ขั้วของอันดูลเตอร์และการปรับเปลี่ยนค่าปริมาณเหล็กในขั้วของอันดูลเตอร์เพื่อลดค่าความผิดเพี้ยนของสนามและค่าความยาวคาบจนมีค่าน้อยมากเพื่อให้ได้แสงซินโครตรอนที่ความสว่างเข้าใกล้ความสว่างของแสงซินโครตรอนที่ปลดปล่อยจากอันดูลเตอร์อุดมคติ ที่ฮาร์โมนิกสูงๆ

สาขาวิชาฟิสิกส์  
ปีการศึกษา 2552

ลายมือชื่อนักศึกษา \_\_\_\_\_  
ลายมือชื่ออาจารย์ที่ปรึกษา \_\_\_\_\_  
ลายมือชื่ออาจารย์ที่ปรึกษาร่วม \_\_\_\_\_

SOMJAI CHUNJAREAN : HIGH FIELD INSERTION DEVICES FOR  
LOW ENERGY ELECTRON STORAGE RINGS. THESIS ADVISOR :  
SAROJ RUJIRAWAT, Ph.D. 166 PP.

SUPERCONDUCTING UNDULATOR/FILED AND PHASE ERRORS/  
UNDULATOR FIELD OPTIMIZATION

Insertion devices like multipole wigglers, Wave-Length Shifter (WLS) and undulators are used in synchrotron radiation sources for extending photon energy and enhancement of angular flux density and brilliance of radiation from storage rings. Because of coherent addition of the emitted radiation along an electron trajectory, permanent undulators are the most advanced sources to produce generally high brightness (and angular flux density) of the radiation. In 1.2 GeV Siam Photon Storage ring (SPS), however, this is true only for low photon energies. Therefore a superconducting undulator (SCU) with very short period length and high magnetic field strength is desired to produce high harmonic photon beams reaching into the hard x-rays regime with high angular flux density of the radiation. At high harmonics ( 7<sup>th</sup> and up ), however, the radiation generated by both permanent and superconducting undulators will produce the highest brightness only if the undulator fields and period lengths (phase) are near perfect. Shimming methods, as applied for room temperature permanent magnet undulators, cannot be used for such superconducting magnets. The effect of field and period errors on the photon flux density in higher harmonics will be presented and limiting tolerances will be discussed in this thesis. A variety of different field optimization techniques such as superconductive correction coils and varying iron content of the SCU pole together with some measurements on a test magnet (SCU) will be discussed such an approach and demonstrate their efficiency to ensure photon fluxes

which are close to theoretical expectations. An evaluation to their usefulness as sources for high photon energies with high angular flux density is carried out.

School of Physics

Academic Year 2009

Student's Signature \_\_\_\_\_

Advisor's Signature \_\_\_\_\_

Co-advisor's Signature \_\_\_\_\_

## ACKNOWLEDGEMENTS

First, I would like to express my gratitude to my research advisor, Prof. Dr. Helmut Wiedemann for his guidance and continuous support throughout my thesis in Ph.D program and his patience to teach me not only the physics but also the spiritual attitude. It is not often that one finds an advisor like him that always find the time to listen to my problems and to give advices. Furthermore he also gave me chances to go abroad to learn how to work with expert people. He taught me how to question thoughts and express ideas. His patience and support helped me overcome many critical situations and finish this thesis. (I hope that I would become as a good advisor to my student as Prof. Dr. Helmut Wiedemann has been to me.) He is surely my idol for supervising advisees.

I am deeply grateful to my academic advisor, Dr. Saroj Rujirawat and Assoc. Prof. Dr. Weerapong Pairsuwan for their support and helping me complete the academic paper and thesis.

A special thanks go to Dr. C.H. Hwang for giving me experimental advice treading me about magnetic field measurement techniques, insertion devices and especially winding of a superconductive wire to fabricate a superconducting undulator at National Synchrotron Radiation Research Center (NSRRC), Taiwan. He also introduced me to the magnet group and gave me a chance to work with his team at NSRRC.

I would like to greatly express my gratitude to Dr. J.C. Jan who is working at NSRRC for his kindness to teach me a lot about the ways to test of the superconducting undulators, sharing his experiences and knowledge to me and for his helpful in his encouragement, practical advices, providing facilities and materials for my

thesis experiment. He also looked after me when I was in Taiwan. Although he is very busy, he spent his time to answer my questions dealing with experiment problem by the e-mail. Furthermore I am very appreciate to work with people who are in the magnet group. I would like to say thank you to Ms. P. H. Lin who taught me about code RADIA and how to design the magnets especially the superconducting undulator to optimize the undulator parameters. And I would like to also thank to Mr. F.Y. Lin for his guidance in measuring magnetic field distribution along an elliptical undulator.

I am also grateful to my thesis committee: Asst. Prof. Dr. Chinorat Kobdaj, who is a chairman of my thesis, Asst. Prof. Dr. Chitrlada Thongbai and Dr. Somsak Dangtip, for their kindness, encouragement and giving insightful comments and review my thesis.

I acknowledge the financial support by Synchrotron Light Research Institute (Public Organization) for four years throughout my Ph.D study.

Many friends have helped me stay sane through these difficult years. Their support and care helped me overcome setbacks and stay focused on my study. I greatly value their friendship.

Most importantly, none of this would have been possible without the love and patience of my parents and my sister, who help me for everything and always give me greatest love, best wishes and willpower until this thesis completion.

Somjai Chunjarean

# CONTENTS

	<b>Page</b>
ABSTRACT IN THAI . . . . .	I
ABSTRACT IN ENGLISH . . . . .	II
ACKNOWLEDGEMENTS . . . . .	IV
CONTENTS . . . . .	VI
LIST OF TABLES . . . . .	X
LIST OF FIGURES . . . . .	XI
<b>CHAPTER</b>	
<b>I INTRODUCTION . . . . .</b>	<b>1</b>
<b>II HIGH FIELD INSERTION DEVICES (ID) FOR THE SIAM</b>	
<b>PHOTON SOURCE (SPS) . . . . .</b>	<b>5</b>
2.1 Review characteristic of WLS . . . . .	6
2.2 Effect of the WLS on Beam Dynamics . . . . .	8
2.3 Hard-edge model . . . . .	9
2.4 Betatron function matching . . . . .	11
2.5 Chromaticity compensation . . . . .	15
2.6 Conclusion and discussion . . . . .	17
<b>III MATHEMATIC TOOLS . . . . .</b>	<b>18</b>
3.1 POISSON code . . . . .	19
3.1.1 Basic algorithms for the code . . . . .	20
3.2 RADIA code . . . . .	22
3.2.1 Basic algorithms for the code . . . . .	22
3.3 B2E code . . . . .	23

## CONTENTS (Continued)

	<b>Page</b>
3.4 MATLAB program for field correction . . . . .	25
3.4.1 Mathematic algorithm of field error correction . . . . .	27
Eigenvectors and eigenvalues . . . . .	29
Singular Value Decomposition . . . . .	34
<b>IV SYNCHROTRON RADIATION AND INSERTION DEVICES</b>	<b>37</b>
4.1 Electron motion in an undulator field . . . . .	39
4.2 Undulator radiation . . . . .	41
4.3 Line spectrum . . . . .	47
4.3.1 Angular spectral flux . . . . .	48
4.3.2 Undulator brightness . . . . .	52
4.4 Superconducting undulator with short period . . . . .	55
4.5 Magnetic field and period length errors . . . . .	58
<b>V REVIEW OF SUPERCONDUCTIVITY</b> . . . . .	<b>64</b>
5.1 Theory of superconductivity . . . . .	64
5.1.1 Type-I superconductor . . . . .	66
5.1.2 Type-II superconductor . . . . .	68
5.2 Niobium titanium . . . . .	70
5.2.1 NbTi specification for superconducting undulator . . . . .	73
5.3 Magnetic field design . . . . .	76
5.4 Quench protection . . . . .	83
<b>VI MAGNETIC FIELD MEASUREMENT</b> . . . . .	<b>88</b>
6.1 Introduction . . . . .	88
6.2 Hall probe . . . . .	89

## CONTENTS (Continued)

	<b>Page</b>
6.3 Beam duct . . . . .	98
6.4 Measurement setup . . . . .	99
6.4.1 Vertical test Dewar . . . . .	100
6.4.2 Magnetic training . . . . .	101
6.5 Magnetic field measurement . . . . .	104
6.5.1 Integral field measurement . . . . .	108
Integral field measurement . . . . .	109
Integration of the field profile . . . . .	111
<b>VII FIELD CORRECTION OF UNDULATOR . . . . .</b>	<b>114</b>
7.1 Introduction . . . . .	115
7.2 Field integral correction . . . . .	119
7.3 Shimming method . . . . .	122
7.3.1 Simulation of iron-trim . . . . .	122
7.3.2 Simulation of trim coil . . . . .	125
7.3.3 Experimental setup and result . . . . .	126
7.4 Field correction with additional coils . . . . .	131
7.4.1 Superconducting additional coil around the undulator pole . . . . .	132
Model for a real magnetic field . . . . .	137
7.4.2 Additional coils in the superconducting gap . . . . .	141
7.5 Field correction by modification of the iron pole geometry . . . . .	144
7.5.1 Simulation of iron content in the undulator pole . . . . .	144
7.5.2 Range of validity . . . . .	151
<b>VIII CONCLUSIONS . . . . .</b>	<b>157</b>

**CONTENTS (Continued)**

	<b>Page</b>
REFERENCES . . . . .	162
CURRICULUM VITAE . . . . .	167

# LIST OF TABLES

<b>Table</b>		<b>Page</b>
2.1	Parameters of the 6.4 T Wave-Length Shifter	7
2.2	Hard-edge-model parameter	. . . 10
2.3	Parameters of the SPS ring	. . . 12
2.4	Quadrupole strengths for bared lattice and matched lattice	. . . . . 15
2.5	Sextupole strength for chromaticities correction	16
2.6	Operating currents of the quadrupole magnets for the SPS ring at 1.2 GeV with the 6.4 T Wave-Length Shifter (WLS).	. . . . . 17
5.1	Critical field strength and temperature of materials	67
5.2	Critical field strength and critical temperature of type-II superconductors.	. . . . . 70
5.3	Specification of NbTi at $T_c \sim 10^\circ K$ multifilament superconducting wire.	. . . . . 75
5.4	Designed parameters of pole and coil of SCU prototype	82
6.1	Specification of the HHP-MP Hall sensor	. . 93
6.2	Field errors	107
7.1	Superconducting wire specification for the correction coil	133
8.1	Tunability range of field strength for an actual SCU	159

# LIST OF FIGURES

Figure		Page
2.1	A photon flux density produced from a 6.4 WLS designed at MAX-lab compared with photon flux density from bending magnet and a 6.4 T multipole wiggler with 17 poles for 1.2 GeV storage ring. . . . .	6
2.2	Measured vertical magnetic field component, $B_y$ , along the beam axis (z-axis) of the 6.4 T WLS. . . . .	7
2.3	Betatron functions ( $\beta_x, \beta_y$ ) and dispersion functions ( $D_x, D_y$ ) of one FODO bare lattice for the SPS ring with beam emittance of 41.4 nm-rad at 1.2 GeV electron energy. . . . .	13
2.4	Betatron ( $\beta_x, \beta_y$ ) and dispersion ( $D_x$ ) functions with 6.4 T WLS inserted at the middle of the straight section in the SPS ring. . . . .	13
2.5	A schematic model of the matching simulated with MAD8 by starting with unperturbed optic functions as the bared lattice at matching points and setting matching constrains at the middle of the WLS. . . . .	14
2.6	Betatron and dispersion functions after matching the tunes with quadrupole strengths listed in Table 2.4 . . . . .	14
2.7	Comparison of Dynamic apertures calculated with BETA and PARTICIA (green star) with the WLS for 1.2 GeV SPS ring. . . . .	16
3.1	Flow chat of the POISSON calculation. . . . .	21
3.2	An algorithm of code RADIA used to compute and design magnetic field. . . . .	24

## LIST OF FIGURES (Continued)

Figure		Page
3.3	Electric field (left) detected by an observer and angular flux density (right) as a function of photon energy for 20 period undulator. . . .	25
4.1	Angular flux density spectrum emitted from a bending magnet with a field strength of 1.44 T and electron beam energy of 1.2 GeV. . .	38
4.2	Distortion of pure sinusoidal motion due to the relativistic transverse motion. . . . .	42
4.3	Distribution of dipole radiation field due to odd and even harmonics in the case of a strong undulator in the moving coordinate (left) and in the laboratory coordinate (right). . . . .	43
4.4	Electric field seen by the observer on axis for the electron (left) and associated angular flux density calculated at beam energy of 2 GeV, period length of 48 mm and number of period of 10 with varying values of $K$ . For small values the electric field is nearly sinusoidal corresponding to a single line in the spectrum but for a large value of $K$ the electric field is distorted into a sharp peak resulting in a large number of harmonic lines in the spectrum. . . . .	44
4.5	The electron trajectory on the deflecting plane in the undulator emit radiation at position A and B. . . . .	45
4.6	Electric field (left) seen by the observer off axis and associated angular flux density calculated at a beam energy of 2 GeV (right) with vertical and horizontal opening angle of 0.5 and 0.0 respectively and deflecting strength $K$ of 2.2. . . . .	46

## LIST OF FIGURES (Continued)

Figure		Page
4.7	Fundamental wavelength as a function of changing the parameter $K$ and observation angle $\theta$ for an undulator with period length of 60 mm and 15 mm. Electron beam energy is 1.2 GeV. . . . .	47
4.8	Amplitudes of odd harmonics in the forward direction as a function of the $K$ values. . . . .	49
4.9	An angular integrated spectrum produced by an undulator with a period length of 15 mm and peak field strength of 1.4 T at an electron beam energy of 1.2 GeV and beam current of 200 mA. . .	51
4.10	Peak field in mid plane of a permanent magnet undulator made from $Sm_2Co_{17}$ (red line) and for a hybrid with Vanadium Permendur poles(blue line) as a function of magnetic gap ( $g$ ) and undulator period length. . . . .	55
4.11	Deflecting parameter $K$ of different $g$ in centimeter, as function of undulator period length for a Samarium-cobalt undulator. . . . .	56
4.12	Typical layout of a superconducting undulator (Wollmann, 2008) with iron poles (green), superconductive wire bundles (red), the gap width $g$ and period length $\lambda_p$ . . . . .	57
4.13	Angular flux density as function of a photon energy, up to the 7 <sup>th</sup> harmonic emitted from permanent undulator with period length of 60 mm and field strength of 0.55 T (dash line) and from a superconducting magnet with period length of 15 mm and field strength of 1.4 T (solid line) at electron beam energy and beam current of 1.2 GeV and of 0.2 A, respectively. . . . .	57

## LIST OF FIGURES (Continued)

Figure		Page
4.14	An ideal magnetic field distributed along an undulator with a period length of 15 mm and a peak field amplitude of 1.387 T. . . . .	59
4.15	Ratio of real to ideal angular flux densities for each harmonic of radiation emitted into a forward cone represented with stars as a function of r.m.s field error. Lines are used only to guide the eye. . . . .	60
4.16	Ratio of real to ideal angular flux densities for each harmonic of radiation emitted into forward cone represented with stars as a function of r.m.s period length error. Lines are used only to guide the eye. . . . .	61
4.17	Electron trajectory of 1.2 GeV electron beam when it travels through a real undulator field with a r.m.s field error of 2 %. . . . .	62
4.18	Ratio of real to ideal angular flux densities for each harmonic of radiation emitted into forward cone represented with stars. Real field is generated with adding r.m.s field and phase errors of 1 % and 1 Degree (small dash line), 2 % and 1 Degree (dash-dot line) and of 3 % and 1 Degree (dash-line). Lines are used only to guide the eye. . . . .	63
5.1	Resistance of superconductivity of the mercury. . . . .	65
5.2	Phase diagram of the type-I superconductor. Electrical resistivity $\rho$ in superconducting state is zero. . . . .	67
5.3	Phase diagram of a type-II superconductor. . . . .	69

## LIST OF FIGURES (Continued)

Figure		Page
5.4	(a) Filaments in an actual cable used for RHIC magnets with a filament size of $6 \mu\text{m}$ . (b) Coupling and uncoupling in multifilaments wire. . . . .	73
5.5	A 2-D schematic dimension of NbTi wire with coated insulation. . .	74
5.6	Critical field and critical current relation measured by the manufacturer of a rectangular superconductive wire NbTi with a Cu/Sc ratio of 1.35. . . . .	75
5.7	3-D model of poles of a superconducting undulator with grooves for superconducting wire. Two array of undulator poles are separated with magnetic gap of 5.6 mm. . . . .	76
5.8	Sketch of magnetic flux line generated only vertical magnetic field in the magnetic gap. . . . .	77
5.9	A sketch in 2-D dimension (upper) of undulator poles (lighter part) wound with superconductive NbTi wire (darker part) and 3-D dimension (lower) of the superconducting undulator including coil racetrack. . . . .	78
5.10	Vertical peak field $B_0$ (left axis) and maximum field in superconducting coil $B_s$ (right axis) for a period of 15 mm for gap height of 5.6 mm are plotted as a function of excitation current $I$ . Critical current $I_c$ in the coil plotted under applied magnetic field (right axis) for rectangular wire ( $0.51 \times 0.77 \text{ mm}^2$ ). . . . .	80

## LIST OF FIGURES (Continued)

Figure		Page
5.11	Vertical magnetic field distributed along a beam axis (in z direction) on the axis. A maximum peak field of the main poles is 1.37 T. . .	81
5.12	A difference in field strength by $\Delta B_y/B_y$ of occurring at the transverse position of $\pm 5\text{mm}$ . . . . .	81
5.13	Electron deviations in angle (a) and position (b) passing through the undulator with a period length of 15 mm, a magnetic gap and designed field of 5.6 mm and 1.37 T, respectively. Electron energy is 1.2 GeV. . . . .	83
5.14	A diagram of a passive quench protection circuit. . . . .	85
5.15	A diagram of an active quench protection circuit. . . . .	86
6.1	A flowing current through the Hall probe generates the Hall voltage $V_H$ . . . . .	90
6.2	Packaged transverse Hall sensor Model HHP-MP from AREPOC Ltd. with $350\ \mu\text{m}$ distance between active area and surface. The active area center is marked accurately to $\pm 0.05\ \mu\text{m}$ as per AREPOC information. . . . .	91
6.3	A schematic of the NMR set up. . . . .	92
6.4	Calibration system of the Hall sensor at NSRRC by using the standard NMR probes at room temperature. . . . .	95
6.5	Measured field strengths monitored with five NMR probes for different field levels as a function of the Hall voltage recorded by the Hall voltage output at a current through the Hall sensor of 10 mA. . . . .	95

## LIST OF FIGURES (Continued)

Figure		Page
6.6	The polynomial fit-coefficients of the Hall sensor calibration . . . . .	96
6.7	Comparison of Hall voltage from the Hall sensor in the presence of a magnetic field (a). Differences between measurements and fits are shown as residuals (b), where the control current fed through the Hall sensor is 10 mA at room temperature ( $300\text{ }^{\circ}K$ ). . . . .	97
6.8	Top view (left) and side view (right) of a Hall sensor holder (schematic) in housing made by SS316L steel and positioned by probe guide. . . . .	98
6.9	(a) Beam duct has a cross section like a racetrack shape with an inner aperture of 5 mm and is coated with a copper layer on the inner surface. (b) the beam duct is glued with the magnet array. . . . .	99
6.10	An assembly of the magnet unit (a) and sketch of cross-sectional view of a beam duct (b). . . . .	99
6.11	Main components of the dewar lid in a vertical test dewar for training and field measurement of the SCU magnet with surrounding temperature of $300\text{ }^{\circ}K$ . . . . .	100
6.12	The SCU15 array in the beam duct assembled mainly of components to be used for the training and the field measurement (a) and copper rod using along the magnet array in order to get rid off the heat source for LHe (b). . . . .	102

## LIST OF FIGURES (Continued)

Figure		Page
6.13	The Training process of the SCU magnet in 32 cycles to achieve the maximum field strength of 1.42 T with a limited quench voltage of 0.3 V at 4.2 °K temperature for T6, T2 and T1. The temperature at the bottom and upper extension bus are as high as 5 and 15 °K , respectively. . . . .	103
6.14	The B-I characteristic of the Hall sensor (HHP-MP type). . . . .	104
6.15	Measured field of the SCU15 along the beam axis using a Hall probe at a temperature of 4.2 °K. . . . .	105
6.16	The measured field and period length of the SCU poles at a current of 510 A. . . . .	106
6.17	Field errors normalized to the minimum (black square), to the average (red dots) and to the maximum (blue triangles) field amplitude. . . . .	107
6.18	Period errors $\Delta\lambda_p/\lambda_{p0}$ normalized to the average (blue squares) value of 15.007 mm. . . . .	108
6.19	Stretched wire diagram system. . . . .	110
6.20	Moving direction of the stretched wire to measure the first (a) and second (b) field integral. . . . .	111
6.21	Electron deviation in angle (a; first integral) and position (b; second integral) at an electron beam energy of 1.2 GeV ( $\gamma$ is about 2348). . . . .	112
6.22	Angular flux density calculated with B2E code at beam energy of 1.2 GeV and beam current of 200 A on-axis. . . . .	113
7.1	Field amplitudes (upper) and period lengths normalized to the average field of 1.387 T and 15.007 mm, respectively. . . . .	115

## LIST OF FIGURES (Continued)

Figure		Page
7.2	Magnetic field distribution in the idealized undulator along the beam axis with field amplitude of 1.3870 T and a period length of 15.007 mm. . . . .	116
7.3	Angle (a) and trajectory (b) deviation of the electron beam at an energy of 1.2 GeV passing through idealized undulator. . . . .	117
7.4	Magnetic field distribution with a field strength of 1.3870 T and period length of 15.007 mm including field errors of 5 % (a) and a period length or phase errors of 3.5 degree (b) and both field and phase errors (c). . . . .	118
7.5	Angular photon flux density for the real test magnet compared with the idealized undulator. Note the appearance of even harmonics due to field and phase errors. . . . .	119
7.6	A cross-section of the SCU (schematic) with the long coil energized with a current of 18 A (current density of 40 A/mm <sup>2</sup> ). . . . .	120
7.7	Electron trajectory with (dash line) and without (solid line) the correction of first and second field integrals. . . . .	121
7.8	Comparison of the angular flux density with and without field integral corrections. . . . .	121
7.9	The SCU array with the trim pole (blue), main coil (red) and the SCU pole (gray) as used in RADIA simulations. . . . .	123
7.10	Sketch of the trim pole and the shim coil mounted on the undulator pole used in the RADIA code. . . . .	123

## LIST OF FIGURES (Continued)

Figure		Page
7.11	Field deviations from the ideal field amplitude due to a trim pole attached to the 21 <sup>st</sup> pole. The trim pole width and length match the width and length of the SCU pole but the thickness of the trim poles vary from 2 mm (black), 5 mm (red), 10 mm (blue), 15 mm (green) to 20 mm (pink). . . . .	124
7.12	Field correction as a function of trim pole height. Dots represent simulated results and solid lines represent a 4 <sup>th</sup> degree polynomial fit to the measurements. . . . .	125
7.13	Relative field amplitude changes due to an iron trim pole with coil as simulated in RADIA. The shim coil mounted at the 20 <sup>th</sup> pole is powered with currents of 10 A and 15A. . . . .	126
7.14	Setup of the trim iron and coils (a) varying height of the iron-trim and profiles of the trim coils, (b) assembly of the iron trim pole winding with iron heights of 5, 25 and 25 mm mounted at the 6 <sup>th</sup> , 18 <sup>th</sup> and 35 <sup>th</sup> , respectively on the beam duct. . . . .	127
7.15	Field measurement without shimming (blue solid line) and with trim-iron shimming (red solid line) presented in the upper part. Field deviations normalized to the non-shimming field amplitude are presented in the lower part. Trim iron of height 5 mm, 25mm and 15 mm are attached on the pole number 6 <sup>th</sup> , 18 <sup>th</sup> and 35 <sup>th</sup> , respectively. . . . .	128
7.16	Comparison between experiment and simulated results of trim-iron shimming at the pole number 6, 18 and 35. . . . .	129

## LIST OF FIGURES (Continued)

Figure		Page
7.17	Comparison of the field errors normalized to the average values before (blue dots) and after (red dots) correction. The average field amplitudes before and after correction with the trim poles are 1.3870 T and 1.3899 T. . . . .	130
7.18	Comparisons of period length changes normalized to the average values with and without correction by coil trimming. The average period lengths with and without shimming are 15.007 mm and 15.124 mm, respectively. . . . .	130
7.19	Superconducting undulator (SCU15, schematic) in two dimensions with the Amperian loop producing a vertical magnetic field. . . . .	132
7.20	Racetrack of the superconductive NbTi wire with 0.1 mm diameter. . . . .	133
7.21	Critical current of the NbTi wire with 0.1 mm diameter measured by the manufacturer (dots) and by a quadratic polynomial fit (solid line). The critical current at 1.4 T and 4.2 °K is 20.34 A. . . . .	134
7.22	Field variations due to a correction coil powered by a current of 20.34 A. The correction coil is wound around the pole # 21. . . . .	134
7.23	Required current as a function of desired field correction. The correction coil has a diameter of 0.1 mm and 15 turns. . . . .	135
7.24	Comparison of the absolute magnetic field amplitude (a) and period length (b) with and without correction coils. The magnetic field is measured at 510 A. . . . .	137

## LIST OF FIGURES (Continued)

Figure		Page
7.25	Real magnetic field profiles as measured at an excitation current of 510 A and simulation with different current densities in the main coils corresponding to the field errors. The average field of the generated and measured magnetic fields are 1.3845 T and 1.387 T, respectively. . . . .	139
7.26	Field (upper) and period length (bottom) errors normalized to a field of 1.387 T and 15.002 mm period length. . . . .	139
7.27	(upper) Angular deviation with (dashed) and without (solid) correction and (bottom) electron beam trajectory with (dashed) and without (solid) correction at 1.2 GeV. . . . .	140
7.28	Relative reduction of the angular photon flux density calculated with B2E for the measured field (dots) and corrected field with correction coils (squares). . . . .	141
7.29	Pole slice of superconducting undulator with correction coil placed in the gap. The diameter of the coil wire is 0.1 mm and the current feed through the coil is 20 A. . . . .	142
7.30	Field changes caused by a correction coil in the undulator gap . . .	142
7.31	Field deviations caused by a correction coil placed at the top of the pole surface. The total cross-section is $0.1 \text{ mm}^2$ and the correction current is 30 A. . . . .	143
7.32	Cross-section of the SCU15 with slit into backside of the poles for a pole length (z) of 2.85 mm and pole width (x) of 99.86 mm. . . .	145

## LIST OF FIGURES (Continued)

Figure		Page
7.33	Changes in field amplitude caused by implementing slits into undulator poles. The slit length is fixed at 1.35 mm while the height (depth) is varied. . . . .	145
7.34	Field changes at the corrected pole (the 21 <sup>st</sup> ) for different slit depths. Dots represent field amplitude changes calculated by POISSON. . . . .	146
7.35	Comparisons of slit depths in a range of about 13 mm to 19 mm related to the field changes between a simulation (stars) and interpolation (line). . . . .	147
7.36	Comparison of expected field corrections for various slit depths as calculated with RADIA (dots) and POISSON (dots). . . . .	148
7.37	Comparison of peak field deviations related to the average and minimum peak field of $B_0 = 1.3505$ T and $B_0 = 1.3521$ T with and without slit correction, respectively. . . . .	148
7.38	The period length with and without field corrections by slits in the undulator poles. The average values of the period lengths before and after correction are 15.007 mm and 15.002 mm, respectively. .	149
7.39	Electron trajectory with and without field error correction with slits.	149
7.40	Improvement of the angular flux density after slit correction in comparison to the uncorrected undulator. . . . .	150

## LIST OF FIGURES (Continued)

<b>Figure</b>		<b>Page</b>
7.41	Variation of r.m.s field errors and allowable r.m.s field errors as a function of field excitation for an undulator which has been corrected at a field of 1.35 T. . . . .	152
7.42	Angular flux density (upper) and brightness (below) of photon radiation emitted from a superconducting undulator with field errors corrected in the SPS 1.2 GeV storage ring. The undulator parameter K is varied within acceptable limits as discussed in the text. .	153
7.43	Angular flux density relative to ideal (dash line) expectations in the forward direction for a measured field (dots), corrected field with correction coils (squares) and corrected field with slits (stars). . . .	155
8.1	A comparison of angular flux density emitted from an ideal (dotted line) and from actual SCU with field correction (solid line) consisting of 200 periods in the 1.2 GeV SPS storage ring. . . . .	159

# CHAPTER I

## INTRODUCTION

Electron storage rings are often used as a source of electromagnetic radiation. This radiation, called synchrotron radiation, is emitted in a wide range of photon energies from microwaves up to maximum photon energies as determined by electron energy and magnetic field and is used for basic and applied research. Synchrotron radiation is emitted from a moving source and is therefore highly collimated in the forward direction in the laboratory system. To characterize the radiation we define the quantities of brightness and angular flux density. The brightness of the photon beam is simply the density of photons in 6-dimensional phase space. A more practical quantity is the angular flux density which is the photon brightness multiplied with the source cross section. The brightness is measured in units of  $[\text{photons}/\text{s}/\text{mrad}^2/\text{mm}^2/0.1\% \text{ BW}]$ , where “BW” stands for energy band width of the photon beam. It is customary to express the brightness to 0.1 % BW. The intensity of synchrotron radiation is higher by many orders of magnitude than conventional sources like VUV lamps or X-ray tubes. In addition, synchrotron radiation is polarized which is often unuseful for scientific applications. Synchrotron radiation is therefore widely used as a powerful tool for basic and applied science in areas like material sciences, chemistry, biology, archeology, geology, protein crystallography and surface science to name just a few. For instance, in the hard X-ray regime diffraction, scattering, absorption and reflection spectroscopy are used to determine atomic and molecular arrangements and investigate material properties at that scale. Whenever the atomic and molecular arrangements are of interest we can use synchrotron radiation as a diagnostic tool. In view of these

broad applications for modern technology, more than 50 synchrotron radiation facilities are in use worldwide and new ones are being designed and constructed. Synchrotron radiation has been first observed indirectly in 1945 by J. Blewett at General Electric (GE) and later in 1947 through a new glass vacuum chamber at the 70 MeV GE synchrotron (Elder et al., 1947) in Schenectady, New York state. First, synchrotron radiation was used parasitically from accelerators built for high energy physics research. With growing demand on applications, dedicated synchrotron radiation sources based on bending magnets were build which we call now  $2^{nd}$  generation radiation. To provide more orders of magnitude of higher flux density and brightness compared with bending magnet radiation and expanding the photon energies for low and medium energy storage rings,  $3^{th}$  generation sources were developed by designing for magnet-free sections in the magnet arrangement of storage rings so that insertion devices could be added to the ring. Insertion devices are magnetic instruments which cause the electron beam to emit synchrotron radiation in such a way as not cause a net deflection of the particle beam. This neutral impact on the electron beam path allows in principle the use of specialized and high fields such as in a wavelength shifter, undulator, wiggler and superconducting multipole wigglers. The electron beam dynamics is strongly perturbed by such high field insertion devices and compensating measures must be developed to retain beam stability. Linear perturbations of the betatron functions and tunes can be compensated by adjusting nearby quadrupole magnets and steering magnets are used to preserve an acceptable Closed Orbit Distortion (COD). Non-linear perturbations may reduce the dynamic aperture are compensated as best as possible with changes in strength of sextupole magnets. Eventually, most perturbations are corrected and the unperturbed configuration of the storage ring restored by betatron and dispersion matching.

Due to weak perturbations of the electron beam dynamics and constructive

interference effects on-axis, permanent undulators are the most advanced sources of high brightness radiation. Therefore, undulators are widely used in high and medium energies storage rings but not in low energy storage rings as the Siam Photon Source (SPS) at 1.2 GeV. The magnetic field strength in the undulator at a given period length is limited by material properties. In order to overcome this limitation and reach high photon energies, a small period length and superconducting magnet technology is desired. Yet, as the period length is reduced, the undulator strength parameter  $K$  will also decrease and the photon beam intensity at higher harmonics becomes too low. The undulator strength parameter  $K$  needs to be equal to at least  $K = 2-3$  to get significant radiation in higher harmonics, which are desired to reach high photon energies. To compensate the loss of strength due to shorter periods we must be able to increase the magnetic field leading us to a superconducting undulator. A prototype of a superconducting undulator (SCU) was fabricated at NSRRC with a period length of 15 mm and a field strength 1.4 T. The magnetic field distribution along the SCU magnet was measured at a magnetic gap of 5.6 mm. We will use this magnet as a reference for performance and correction possibilities.

Even with sufficient undulator strength, high brightness photon beams at higher harmonics can be produced only when the magnetic field distribution of the SCU is almost perfect. In reality, due to construction tolerances, field and phase errors exist which strongly affect the intensity especially at high harmonics of the photon radiation. Thus, in order to reach high brightness from a real SCU, techniques must be developed to correct magnetic field and phase errors. This is done to equalize all undulator periods resulting in almost ideal brilliance even at high harmonics of radiation. A well known shimming technique for field errors to correct permanent magnet undulators cannot be used for superconducting undulators like the SCU. Therefore, different techniques such as additional superconductive

correction coils and varying iron content of poles of SCU are proposed. These techniques will be used to correct field errors in the SCU and their effectiveness will be evaluated by simulation.

In the first part of this thesis, a shimming method used for permanent undulators is investigated and experimentally tested to compensate changes in field amplitudes known as field errors of the SCU. In the second part, additional superconductive correction coils are used by a simulation with the code RADIA to correct field errors along the SCU. The correction coils are energized with separated power supplies. Although this method is a very powerful correction for both field and period length errors, cost of the power supplies for each correction coil is prohibitively expensive. In addition, all connections between the superconductive wires must reach into a liquid He-dewar at  $4.2 \text{ }^\circ\text{K}$  becoming a major heat source to boil-off liquid helium in the dewar. Thus, we propose a more passive correction by varying the iron content of the SCU poles. Due to saturation effects in the iron, field correction can be achieved by reducing their amplitudes to a minimum level throughout the magnet to obtain a small r.m.s field error. This variation of iron content can be achieved by manufacturing hollow magnet poles which then are filled with iron pieces as desired.

Acceptable field and phase errors should be less than 1 % and 1 degree, respectively in order to achieve an angular flux density as high as 90 % of ideal as will be discussed in Chapter IV. Although we cannot offer a direct technique to correct phase errors, we will see that the correction of field errors also will lead to a sufficient correction of period length (phase) errors. Advantages and disadvantages of each correction concept are discussed and summarized in Chapter VII. We use codes like RADIA and MATLAB to simulate the field correction concepts and logical corrections for the SCU as summarized in Chapter III.

# CHAPTER II

## HIGH FIELD INSERTION DEVICES (ID) FOR THE SIAM PHOTON SOURCE (SPS)

Often synchrotron radiation is obtained from bending magnets but in low energy storage rings such as the Siam Photon Source (SPS) at 1.2 GeV , hard X-rays cannot be produced at a desirable intensity. Since the beam energy of the SPS storage ring cannot be readily increased beyond 1.2 GeV, higher magnetic fields must be utilized to reach X-ray photon energies of 2-5 keV at acceptable intensities. An insertion device such as a superconducting multipole wiggler, Wavelength Shifter (WLS) or undulator can be used. Due to the strong magnetic field strength of the multipole wiggler or WLS in a low energy storage ring, they have strong influence on many aspects, either linearly or non-linearly, of beam dynamic. The linear effects include close orbit distortion (COD), vertical betatron tune shifts, betatron/dispersion mis-matching and increased energy loss per turn while non-linear effect can reduce of the dynamic aperture. Therefore, to install a wiggler or WLS at a straight section in the storage ring, all perturbations should be compensated by adjusting the strengths of nearby quadrupole magnets. Non-linear effect can be compensated in the nearby sextupole magnets. Matching of the betatron and dispersion functions in nearby unit cells and readjustment of the overall tunes restoring almost perfectly the configuration have to be done. In this chapter, we will discuss methods to compensate such perturbations caused by a 6.4 T WLS on the storage ring optics.

## 2.1 Review characteristic of WLS

A Wave-Length Shifter (WLS) comprises three ordinary dipole magnets with a high field in the central pole and lower fields at side poles to compensate the electron beam deflection caused by the central field. Only the central field serves as the source of synchrotron radiation which a spectrum like that of a bending magnet. Since the width of the photon energy spectrum directly depends on field strength and energy of the electron beam, the photon energy emitted from the WLS is higher than that emitted from a bending magnet with similar photon flux density (or brightness). Figure 2.1 shows a comparison of the photon flux density produced from a 6.4 T WLS, 6.4 T multipole wiggler (SMPW) with 17 poles and the 1.44 T bending magnet at electron energy of 1.2 GeV.

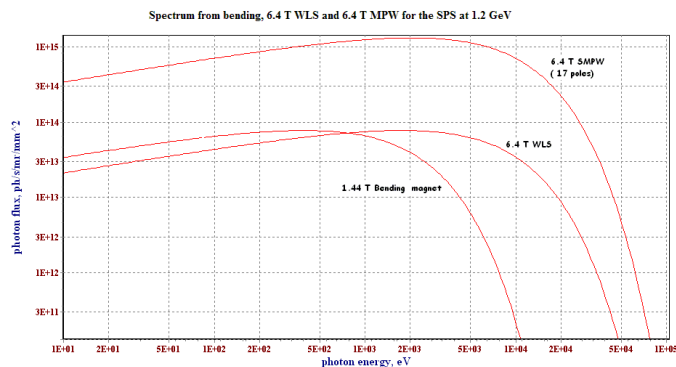


**Figure 2.1** A photon flux density produced from a 6.4 WLS designed at MAX-lab compared with photon flux density from bending magnet and a 6.4 T multipole wiggler with 17 poles for 1.2 GeV storage ring.

A Wave-Length Shifter (WLS) was donated to NSRC, which was designed and fabricated at MAX-lab (Soderlund, 1998), has a central and side fields of 6.4 T and 3.7 T, respectively. The side fields are opposite field direction on either side to reach a zero value of the overall deflection angle of the electrons moving through the WLS. A period length of 278 mm has been measured (Wallen, 1998)

**Table 2.1** Parameters of the 6.4 T Wave-Length Shifter

Peak field at central pole	6.44 T
Peak field at side poles	3.7 T
Period length of central pole	278.34 mm
Period length of side pole	239.78 mm
Pole gap	36 mm
Over all length	398 mm
Excitation current	250.1 A

as shown in Figure 2.2. According to the field measurement both first and second field integrals are close to zero. It means that the deviation in angle and position of the electron beam moving through the WLS are quite small and close to zero as designed.

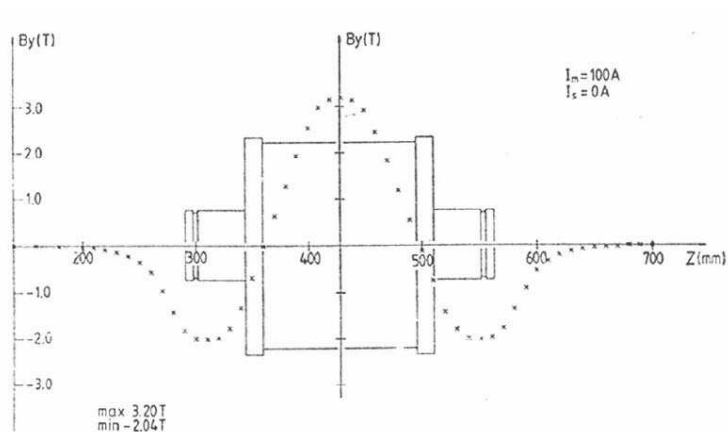


**Figure 2.2** Measured vertical magnetic field component,  $B_y$ , along the beam axis (z-axis) of the 6.4 T WLS.

Major parameters obtained from field measurements at an excitation current of 250.1 A of the 6.4 T Max-WLS are listed in Table 2.1. To avoid a change in geometry, the optics of the storage ring must be adjusted when the WLS is

installed at some location in the storage ring. Matching of the betatron and dispersion functions is required to restore the beam optics to the original values in the rest of the storage ring without the WLS. This is required for beam stability and to avoid photon beam instability for other users when the WLS field is turned on or changed.

## 2.2 Effect of the WLS on Beam Dynamics

This problem is rather serious for a low energy ring because the energy of the electron beam is small while the field strength of the WLS is strong. The WLS will introduce an intrinsic focusing property in the vertical plane (y-axis) due to wiggling of the electron in the deflecting plane (x,z) due to the periodic sinusoidal field distribution along the reference path. The electron path is not parallel to the reference path and the pole faces of the wiggler, being a series of rectangular dipole magnets, are not at 90 degrees to the electron path. As a result, a transverse field component (Wiedemann, 2007) appears to the electron deflecting it into the vertical plane. Since the horizontal field varies linearly with amplitude, a vertical focusing occurs in the wiggler magnet. The integrated focusing field gradient per half wiggler pole results in an integrated quadrupole strength described by

$$k_y l = -\frac{1}{8} \left( \frac{ceB_0}{cp} \right)^2 \lambda_p = -\frac{1}{f_y}, \quad (2.1)$$

or a focal length  $f_y$  for each half pole. Equation 2.1 can be expressed in terms of bending radius  $\rho_0$  and wiggler period length  $\lambda_p$  by

$$\frac{1}{f_y} = \frac{\lambda_p}{8\rho_0^2}. \quad (2.2)$$

This focusing property in the wiggler (and WLS) causes a change in vertical betatron tune which is the number of electron oscillations per orbit. Here, the tune

shift estimated with a quadrupole strength change by

$$\Delta\nu_y = \frac{1}{4\pi} \sum_{i=1}^N \beta_{y,i}(s) \Delta k l_i = \frac{1}{4\pi} \sum_{i=1}^N \frac{\beta_{y,i}}{f_i} \quad (2.3)$$

From Equation (2.2) and (2.3), the tune shift resulting from the WLS can be rewritten as

$$\begin{aligned} \Delta\nu_y &= 2 \cdot \frac{1}{4\pi} \cdot \frac{\beta_y}{f_{central}} + 4 \cdot \frac{1}{4\pi} \cdot \frac{\beta_y}{f_{side}} \\ &= \frac{1}{4\pi} \cdot \frac{\beta_y}{8} \left( 2 \frac{\lambda_{p,central}}{\rho_{0,central}^2} + 4 \frac{\lambda_{p,side}}{\rho_{0,side}^2} \right), \end{aligned} \quad (2.4)$$

where the factor 2 relate to two end fields for the central pole and the factor 4 to the four end fields of both end poles. The betatron function of the electron beam can be greatly perturbed due to these end fields. If the vertical betatron function at a location of the WLS is large, then the tune shift also is large and thereby altering the beam optics in the whole storage ring. The brilliance in the synchrotron radiation may be reduced and large betatron functions may reduce the dynamic aperture. In order to minimize a change in the betatron function, the WLS should be located at places of low betatron functions. However the effect of the WLS on the beam optics should be eliminated all together and the optics should be restored to the original one outside the WLS section. Within a narrow region on either side of the WLS, we apply local correction measures that can be worked out with a code like MAD8 (Grote and Iselin, 1991).

### 2.3 Hard-edge model

Before discussing matching, we introduce a hard-edge model to approximately describe an actual distribution of the magnetic field of the WLS which can then be used in MAD8. The hard-edge model is appropriate to describe the linear properties of the WLS or wiggler magnet. We would like to derive a hard edge model which meets three conditions (Wiedemann, 1998) the deflecting angle

**Table 2.2** Hard-edge-model parameter

Parameter	Central pole	Side pole
Magnetic field strength, $B_0$ [T]	6.32	-3.69
Radius of half pole of actual WLS, $\rho_0$ [m]	0.63316	-1.0844
Deflecting angle of half pole, $\vartheta$ [rad]	0.06996	-0.03519
WLS period length, $\lambda_p$ [mm]	278.34	239.78
Radius of half pole of Hard-edge model, $\rho_h$ [m]	0.8062	-1.3808
Half pole length of Hard-edge model, $l_h$ [m]	0.05640	0.04859

and edge focusing and quantum excitation or damping. Since we have only two parameters, we settle on meeting the deflecting angle and focusing. The deflecting angle can then be expressed by following

$$\vartheta = \frac{l_h}{\rho_h} = \frac{\lambda_p}{2\pi\rho_0} = \frac{K}{\gamma} \quad (2.5)$$

From (2.2) and (2.5), parameters of the Hard-edge model are

$$\begin{aligned} \rho_h &= \frac{4}{\pi}\rho_0 \\ l_h &= \frac{2}{\pi^2}\lambda_p \end{aligned} \quad (2.6)$$

where  $\rho_h$  and  $l_h$  are the bending radius and the length of the half pole of the Hard-edge model. The parameters of the Hard-edge model and actual WLS can be calculated and summarized in Table 2.2. From Equation (2.4), the tune shift in the vertical component can be estimated due to the edge focusing property from the WLS field. However this focusing does not introduce tune change in deflecting plane (x,z). Following the actual WLS parameter listed in Table 2.2, the vertical tune shift due to field strength of two side and one central poles is about 0.0715.

## 2.4 Betatron function matching

To allow insertion device in the lattice of a storage ring, the periodicity of the lattice will be broken because the optic functions are perturbed by the WLS. The optics in the part of the ring outside the insertion device should not be changed. To do this, the optics changed by the WLS effect must be matched to give the same optic functions at matched point as the original unperturbed configuration (bare lattice). The matching points are at the beginning and the end of the location of the WLS and have the optic functions the same with the bare lattice as listed in Table 2.3. The lattice of the SPS ring (Kwankasem, 2007) is Double Bend Achromat (DBA) lattice consisting of four fold symmetry with four long straight sections and the betatron and dispersion functions shown in Figure 2.3. The middle of the straight sections has low vertical betatron function where the WLS has to be inserted. The main parameters of the SPS listed in Table 2.3 are used to restore to the unperturbed optic functions by the matching with MAD8. The WLS described and parameters of its Hard-edge model is inserted in the middle of a magnet free straight section to investigate distortions of the betatron functions as shown in Figure 2.4.

The WLS not only causes a large distortion of the vertical betatron function, but also a vertical tune  $\nu_y$  shift from 2.823 to 2.906 while the horizontal tune  $\nu_x = 4.750$  remains the same as in the unperturbed lattice. The tune shift  $\Delta\nu_y = 0.083$  appears only in the vertical plane as expected. A compensation scheme to restore the unperturbed optic functions, is studied with MAD8. To match the optics, the magnetic field strength of quadrupoles adjacent to the WLS are adjusted by iteration to find a good solution to matching constraints. Therefore, the number of the quadrupoles needed for matching depends on the constraint parameters. We set the constrains in the middle of the insertion device where we require for

**Table 2.3** Parameters of the SPS ring

Electron energy (Upgrade), E	1.2 GeV
Circumference, C	81.3 m
Magnet Lattice	DBA
Betatron tunes, $\nu_x, \nu_y$	4.750, 2.823
Betatron functions in the middle of a straight section	17.115, 3.208 m
$\alpha_x, \alpha_y$	0.0, 0.0
Horizontal dispersion (displacement of Ref path), $\eta_x$	0.806 m
Natural chromaticities, $\xi_x, \xi_y$	-8.736, -7.744
Natural emittance	41.4 nm-rad

symmetry that  $\alpha_x = \alpha_y = \eta'_x = 0.0$ , where  $\eta'_x$ . The  $\alpha_{x,y} = \frac{1}{\beta}_{x,y}$  and  $\eta'_x$  is the slope of the dispersion function at the location of the WLS. In MAD, the matching starts and stops in adjacent straight sections with unchanged lattice functions including betatron, dispersion functions,  $\alpha_x$  and  $\alpha_y$  listed in Table 2.3 and shown in Figure 2.5.

After some iterations to match the lattice functions, it is seen that the goal is reached very closely, by changing the strength of three quadrupoles labeled with QF1W, QD2W and QF3W to fit the three constraints. These quadrupole strength gives the horizontal and vertical betatron tunes  $\nu_x = 4.750$  and  $\nu_y = 2.963$ . Eventually the tunes can be restored close to those of the bare lattice by adjusting the strength of all four quadrupole families in the rest of the ring. All the quadrupole strengths for the optics matching are presented in Table 2.4 compared with the strengths of the four quadrupole families for the lattice function without the WLS (bare-lattice).

Figure 2.6 shows the restored betatron functions after matching and global

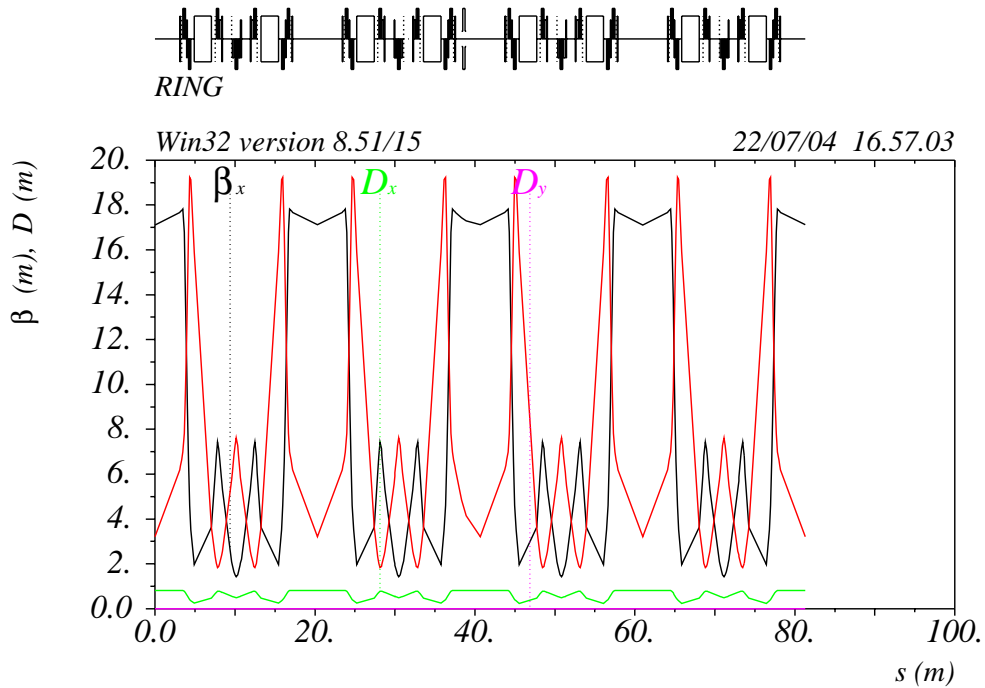


**Figure 2.3** Betatron functions ( $\beta_x, \beta_y$ ) and dispersion functions ( $D_x, D_y$ ) of one FODO bare lattice for the SPS ring with beam emittance of 41.4 nm-rad at 1.2 GeV electron energy.

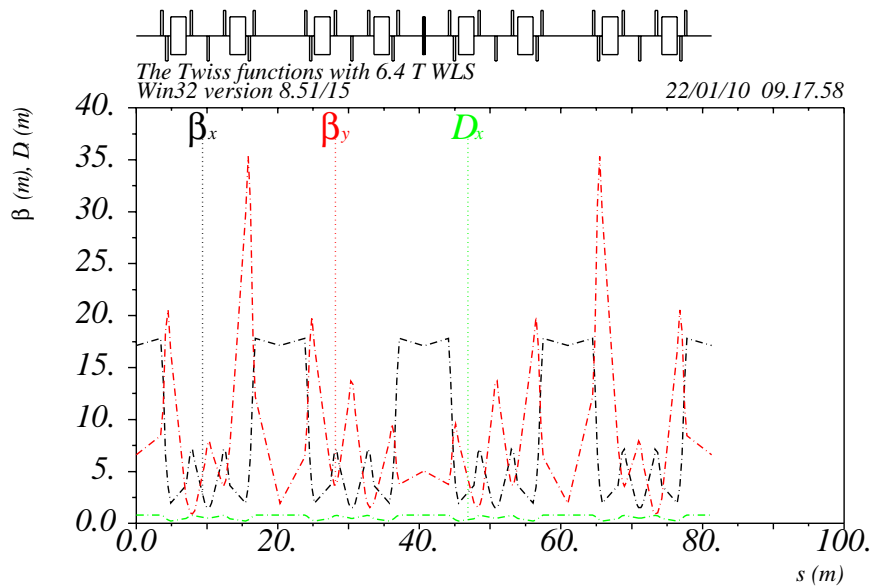


**Figure 2.4** Betatron ( $\beta_x, \beta_y$ ) and dispersion ( $D_x$ ) functions with 6.4 T WLS inserted at the middle of the straight section in the SPS ring.

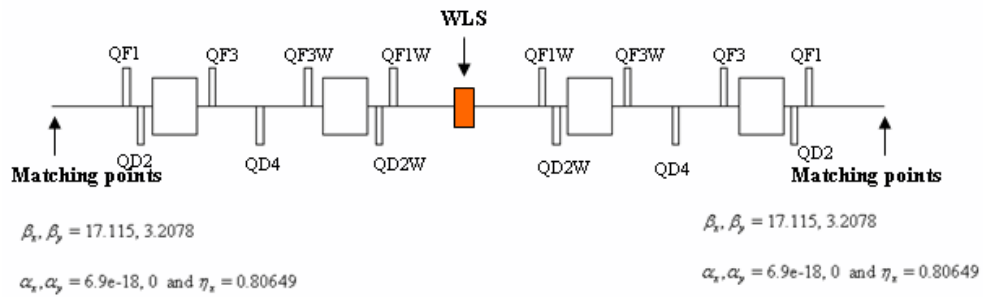


**Figure 2.5** A schematic model of the matching simulated with MAD8 by starting with unperturbed optic functions as the bared lattice at matching points and setting matching constrains at the middle of the WLS.

tune adjustment. As a result we can keep the vertical betatron function to less than 20 m and also completely compensate the tune shift.

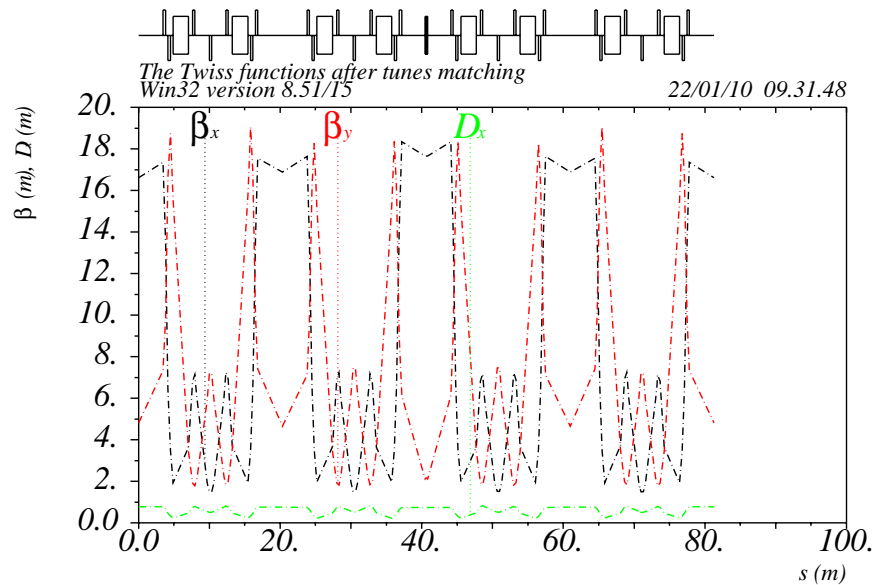


**Figure 2.6** Betatron and dispersion functions after matching the tunes with quadrupole strengths listed in Table 2.4

**Table 2.4** Quadrupole strengths for bared lattice and matched lattice

Quadrupole strength, $m^{-2}$		
Quadrupole	Bare-Lattice	Matched-Lattice
QF1	2.4319	2.4174
QD2	-2.6096	-2.5447
QF3	2.3884	2.3864
QD4	-1.7439	-1.7759
QF1W	-	2.3889
QD2W	-	-2.7116
QF3W	-	2.4586

## 2.5 Chromaticity compensation

Although the optics perturbation due to the WLS field can be compensated and the operating point can be restored close to the original lattice, the WLS still has an effect on the reduction of the dynamic aperture. Therefore, to correct the chromaticity to zero values, codes like BeamOptics (Wiedemann, 2002) and MAD8 are used to tune the sextupole strengths. Since the calculation of the chromaticity in BeamOptics includes some higher order terms compared to MAD8, different sextupole strengths are required in BeamOptics to correct the chromaticities. Table 2.5 shows the strength comparison of two sextupole families, SF and SD, used to correct chromaticities with the BeamOptics and MAD8 code. The dynamic aperture after chromaticities correction with the sextupole strength in Table 2.5 has been calculated with codes BETA and PARTICIA (Wiedemann, 2002) to compare the simulated results. In BETA the WLS is represented with the Hard-edge model while in PARTICIA a sinusoidal field is used for particle tracking. As a

**Table 2.5** Sextupole strength for chromaticities correction

Sextupole	Strength $m^{-3}$ -MAD	Strength $m^{-3}$ -BeamOptics
SF	22.258	22.632
SD	-22.883	-26.775

result, shown in Figure 2.7, we can see that the dynamic aperture calculated with PARTICIA and BETA are approximately the same and most of electron tracking are within a physical aperture defined by the vacuum chamber. In addition to the effect of the WLS on the dynamic aperture, it also introduces an emittance blowup of about 36 % compared to the bare lattice. The natural emittance of the perturbed lattice with the WLS is increased from 41.4 to 56.1 nm.rad. After tracking the electron beam, we can see that the electron beam can survive.

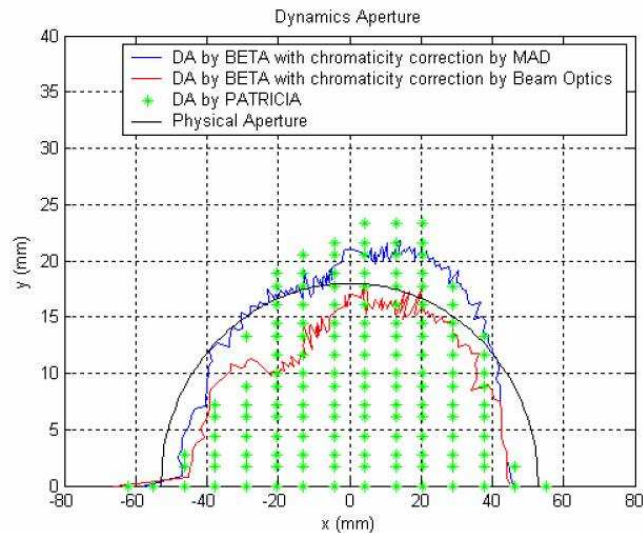


**Figure 2.7** Comparison of Dynamic apertures calculated with BETA and PARTICIA (green star) with the WLS for 1.2 GeV SPS ring.

**Table 2.6** Operating currents of the quadrupole magnets for the SPS ring at 1.2 GeV with the 6.4 T Wave-Length Shifter (WLS).

Magnet	Field strength $m^{-2}$	Field [T/m]	Operating Current [A]
QF1	2.4174	9.6763	365.1
QD2	-2.5447	-10.1858	380.1
QF3	2.3864	9.5522	374.4
QD4	-1.7759	-7.1085	278.4
QF1W	2.3889	9.5622	360.8
QD2W	-2.7116	-10.8539	405.0
QF3W	2.4586	9.8412	385.8

## 2.6 Conclusion and discussion

From the B-I characteristics of the quadrupole magnets supported from SORTEC and beam rigidity to circulate the electron beam with bending radius and magnetic field of 2.78 m and 1.44 T, respectively, the operating current of quadrupole and sextupole magnets used for the lattice functions matching and global tunes can be summarized in Table 2.6. We have discussed the perturbations caused by the installation of a 6.4 T WLS into the 1.2 GeV SPS. Applying appropriate correction measures it is shown that the perturbations can be compensated almost perfectly by adjusting nearby quadrupoles. This capability encourages us to consider other high field insertion devices which would produce desirable radiation characteristics since we are now confident that their impact on the storage ring beam optics can be handled even at low energies.

# CHAPTER III

## MATHEMATIC TOOLS

The design and performance of the test magnet (SCU) has been simulated in two or three dimensions with the codes POISSON (Swatloski, 1993) and RADIA (Elleume et al., 1997), respectively. Field simulation can be performed by using both codes but POISSON will show the magnetic flux density in iron and generate magnetic field in two dimensions while the 3-D code RADIA will enable one to investigate magnet fields from small shapes and sizes of the magnet pole. Although both programs are based on different mathematics, they are useful to design the magnet to obtain optimized parameters for design. Eventually, the magnetic field along the beam axis calculated with RADIA and POISSON is used to compute an angular photon flux density at a given electron energy with B2E (Elleume and Marechal, 1991). This code transforms directly the electron trajectory in a given magnetic field into the electric field of the radiation. For an undulator magnet the photon radiation is quasi-monochromatic as will be described in Chapter IV. The characteristics of the radiation from the undulator are a consequence of the pure periodic magnetic field variation along the undulator. This describes an ideal undulator without field and period length errors according to design. Radiation of the electrons traveling through the ideal periodic magnetic field reaches a high brightness or photon flux density for each high harmonics of the photon beam. In practice, the magnetic field is almost but not completely periodic due to field and phase errors causing a reduction of the flux density especially at high harmonics. In order to achieve a high photon flux density at high harmonics, a perfect undulator without errors is required. Field and phase errors are changes in field amplitudes

and period lengths along the undulator. After determining a correction method, these errors will be compensated by using the MATLAB program. The MATLAB program written by the author in this thesis is based on a linear algebra technique to obtain the best corrections to the errors in the undulator. This is known as a Singular Value Decomposition (SVD). It creates a pseudo-inverse matrix to extract information in order of significance. This chapter will describe all mathematic tools used for the design of real undulators.

### 3.1 POISSON code

The POISSON code was written and developed by Ronald F. Holsinger and Klaus Halbach and maintained by a government funded program. The code supported by Lloyd M. Yong and James H. Billen is based on a two dimensional problem for calculating static magnetic and electric fields. The program is required to carry out tedious analysis requiring point by point calculation of two dimension field distribution called Finite Element Method (FEM). The POISSON code solves the Maxwell's steady state magnet equation in an integral form in two dimensions. Maxwell's equation will be equivalent to an energized form of Poisson's equation in two dimensions when boundary conditions are taken into account. To generalize the Poisson equation an assumption of the magnetic field vector  $\vec{B}$  in term of a curl of the vector potential  $\vec{A}$  is applied. With application of a boundary in the problem, we have to have a qualitative idea how the field behaves at the boundary. There are two boundary types, the Dirichlet  $A_b = c$  where the field lines are parallel to the boundary and the Neumann  $\frac{\partial A_b}{\partial n} = 0$  boundaries, where the field are orthogonal to the boundary. By solving the Poisson's equation [Poisson code] described with

$$aA_b + b\frac{\partial A_b}{\partial n} = c \quad (3.1)$$

in two dimensional grids generated by defining the boundaries of coils, yoke and pole of the magnet, the static magnetic field can be calculated by successive point over relaxation (SPOR) method which is efficient for problems with a rapid converge.

In the POISSON, a basic magnet theory is used to obtain results presented an edited list of the vector potentials and field component values in rectangular regions. The values of vector potential are interpolated around an arc of good field region to determine the boundary conditions for solutions of the field distribution in two dimensions. The mesh size can be limited and then provide a finer mesh for defining of pole tip configuration. Usually the code will start with uniform triangular meshes until sides of the mesh match the boundary condition and interface between different physical materials as close as possible. Properties of each physical material such as copper iron and air or vacuum can be defined in the code. The code generates the mesh by calling the LATTICE command. To prepare input data for LATTICE, AUTOMESH command is called in order to obtain more physically meaningful data and make input simple. Eventually the mesh and physical properties are used to find the vector potential  $A(x, y)$  at all mesh points by calling POISSON.

### **3.1.1 Basic algorithms for the code**

The POISSON code run follows a flow chart shown in Figure 3.1 starting from a text input file. The input file must define and describe the boundary geometry and desired output format. To generate a temporary file with the same name as the input file and designation \*.T35, AUTOMESH must be run. This command is used to construct a logical mesh and generate x,y coordinates for straight lines, arcs and segments of hyperbolas and prepare an input data for LATTICE com-

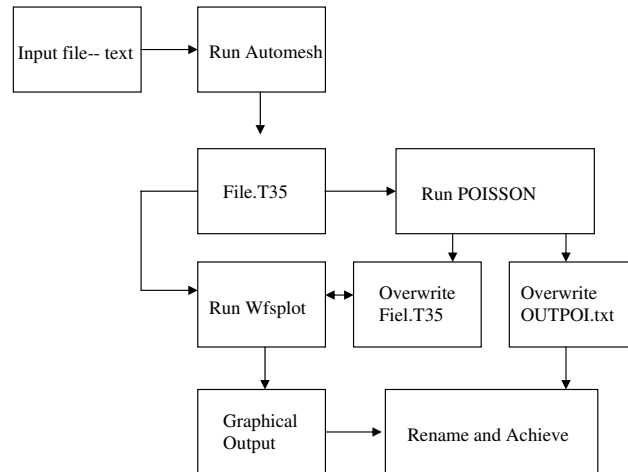


**Figure 3.1** Flow chat of the POISSON calculation.

mand. Filename.T35 is a source for either POISSON or PANDIRA or Wfsplot. If the Wfsplot is run before the POISSON, a graphical output displays geometry of the input without the meshes while Wfsplot is run after POISSON calculation, the output presents a vector equipotential superimposed on the outline of the input geometry. Finally POISSON's output is written in a text file OUTPOL.txt or OUTPAN.txt consisting of B-H relation of selected steel used in the computation, vector potential, field and field gradient distribution in regions specified in the input file. The POISSON is only one of many codes available for magnet calculations. The output from the code is written in a text file containing a summary of the input data and a table of the field component and the field gradients. These output data are used to calculate the vertical field component of accelerator magnets and insertion devices. However, it can be used to design the magnet with optimized pole size and pole tip, calculate derivatives of the potential, stored energy and perform harmonic analysis of the potential. Using the two-dimension analysis tool, an operation is so simple and also saves time and it provides more accurate results than three dimensional codes.

## 3.2 RADIA code

Many commercial codes in three dimensions are developed with a sophisticated operation with adding three dimensions of mesh to model magnets based on Boundary Integral Method (BIM) method (Tortschanoff, 1984; Chubar et al., 1998). A RADIA (Chavanne et al., 1998) code developed at ESRF is a 3D-code used to solve physical and technical problems in many fields especially for development of insertion devices such as wiggler and undulator magnets. The RADIA code is essentially a 3D magnetostatics code to solve boundary magnetostatics problems with magnetized and current-carrying volumes using the boundary integral approach or BIM. The code is written in C++ language with a set of functions and interfaced to Mathematica.

### 3.2.1 Basic algorithms for the code

Based on finite volume integrals to solve the 3D magnetostatic problems by a relaxation procedure (Chubar et al., 2004), RADIA can successfully complement the FEM method. The 3D magnetostatics are formulated in terms of integral equations with respect to magnetization reciprocally interacting volumes. The volumes are separated into number of elementary polyhedrons with constant magnetization vectors. By uniform magnetized polyhedron according to the magnetization vectors, magnetic field can be created at any point. Result will be performed by analytic  $3 \times 3$  matrix with a large matrix in memory which represents mutual interactions between the objects. This is known as interaction matrix. Eventually magnetization in each small object are obtained iteratively by a sequence of multiplications of the interaction matrix with instant magnetization vector taking into account. This is called a relaxation process. Analytical formulas are used at calculation of components of the interaction matrix and the field after the relaxation.

The analytical formulas for the magnetic field are used to avoid any segmentation of free space between magnetized volumes which is required in FEM and minimized segmentation density for iron of geometries. After the relaxation process, both the magnetic field and field integral can be calculated anywhere in space and by using the analytical formulas, this may be give a high precision on the field integral In RADIA, several types of objects can be created and then combine them together to solve the problem. Basic type of objects is source objects capable of creating magnetic fields. This includes magnetized volumes, current coils of several shapes and container objects. The magnetized volumes can be divided into small objects of the same kind with independent magnetization. Furthermore space transformations; translation rotation around an arbitrary axis, plane symmetry, translation and field inversion are next type of objects. Several space transformations can be combined into a new space transformation. The field, created by the object which the space transformation is applied, is calculated first in an object's frame then transform back to the laboratory frame. After creating all the objects, they are link together to build a model of magnet. Examples of input files dealing with accelerator magnets including wiggler and undulator are available free download on website. A simple algorithm of the RADIA can be summarized as shown in Figure 3.2.

### 3.3 B2E code

The B2E code (called “B to E ”) is a software developed at ESRF by an insertion device group to calculate the synchrotron radiation spectrum emitted from insertion devices. This program requires only a magnetic field (ideal or measured) distributed along the magnets to calculate the electron trajectory propagating inside the periodic magnetic field. From the trajectory of a single electron, transverse

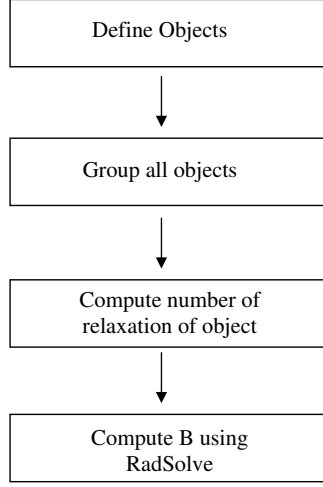


**Figure 3.2** An algorithm of code RADIA used to compute and design magnetic field.

electric fields ( $E_x, E_z$ ) (Elleume and Onuki, 2003) in the near or far field can be produced and expressed by

$$\vec{E}(x, y, z, \omega) = \frac{ie\omega N}{4\pi\epsilon_0 c^2} \sum_{n=1}^{\infty} (-1)^{n(N-1)} \int_{-\infty}^{\infty} \int_{-\infty}^{\infty} \vec{h}_n(\theta_x, \theta_y) \frac{\sin(\pi N((\omega/\omega_1) - n))}{\pi N((\omega/\omega_1) - n)} \times \exp\left(i\frac{\omega}{c} \left(\theta_x x + \theta_z z + s \left(1 + \frac{\theta_x^2}{2} + \frac{\theta_z^2}{2}\right)\right)\right) d\theta_x d\theta_y \quad (3.2)$$

where  $\vec{h}_n(\theta_x, \theta_y)$  represents a contribution to the electric field on the n-th harmonics of the radiation spectrum in direction  $(\theta_x, \theta_y)$ . As this result an angular flux density of the radiation can be computed in term of  $\vec{h}_n(\theta_x, \theta_y)$  and sinc function. An angular flux density of the radiation from an undulator and also from other insertion devices can be calculated as shown in Figure 3.3.

The B2E code is simple to use and is developed to operate with commercial front-end software Igor Pro. Because of dealing with long waves of data and graphical analysis, WINGZ which is a front-end software for the RADIA code is not preferred so that Igor is widely used. Moreover B2E is used for correcting field

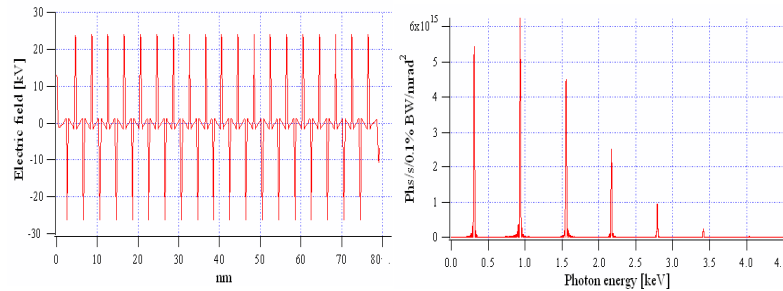


**Figure 3.3** Electric field (left) detected by an observer and angular flux density (right) as a function of photon energy for 20 period undulator.

integrals to adjust close to ideal field integrals. Computation is done for the peak to peak field fluctuations, electron angles and trajectory, computing and graphing of electric field of the pulse of radiation generated by an electron, computing of 4 Stokes spectra components and associated polarization rates of the radiation pulse produced by a single electron as well as electron beam with finite size, angular spread and energy spread, photon radiation from measured magnetic field and simulated field data with analytical estimates as sinusoidal, tapered undulators and wigglers. Usually the RADIA code is more appropriate to optimize design of the insertion devices for specific application and of accelerator magnets. However RADIA cannot be used to predict a reduction on the angular flux density of the photon beam due to magnetic field errors or any absence of periodicity in the field. Both B2E and RADIA codes are good tools depending on the nature of the specific problem under consideration.

### 3.4 MATLAB program for field correction

A program written in MATLAB will be used to apply correction techniques to correct magnetic field amplitude errors in undulators. The goal of optimization is defined in the program. This is usually done by means of a cost function. Usually

the cost function is a positive value or zero. This function measures differences between conditions that we have and desired conditions. Therefore, in the program, values of the cost function should be decreased monotonically as we approach the goal. The program will run with several iterations until this value vanishes. A typical cost function  $f$  is a quadratic difference between the actual data  $y_i$  and desired  $y_0$  and described by

$$f = w \sum_{i=1}^N (y_i - y_0)^2 \quad (3.3)$$

where  $w$  is a weighting factor which is a positive value. The weighting factor has been used in each iteration. At large  $f$  is caused by an error and therefore to completely compensate the error when all  $y_i$  are equal to  $y_0$ . We can choose other cost function that has similar properties, such as

$$f = w \sum_{i=1}^N |y_i - y_0| \quad (3.4)$$

However this is not easy to work with if one want to perform some gradient search type method, as it is easier to take the derivative of (3.3). Generally, a completely perfect undulator without errors is never achieved. Thus the goal of the optimization problem is only to find the set of parameters that give the lowest value of the cost function. One of the first things that have to be done is to determine the cost function for the field correction of the undulator. The cost function should describe well the physics of the correction. Here we use the r.m.s field error to be the cost function to correct the field amplitude deviations. The r.m.s field error is described with

$$f \rightarrow \sigma_{rms-B} = \sqrt{\frac{\sum_i^N (B_i - B_0)^2}{N}} \quad (3.5)$$

The desired ideal field  $B_0$  depends on the correction techniques. Some of the techniques can only decrease the field amplitude while others as correction coils

can decrease and increase the field depending on the direction of the correction current flowing through the coils. However, to achieve the goal, the r.m.s field error will be reduced to small value as possible. To reach that, the r.m.s field error in each iteration of the program is weighted with a factor of 0.9. This factor can be reduced more to close to the lowest r.m.s field error. For example if we apply a factor of 0.5 to each iteration then after iteration, a remaining error is Iteration 0: r.m.s field error = 1.0

Iteration 1: r.m.s field error =  $1.0 \times 0.5 = 0.5$

Iteration 2: r.m.s field error =  $0.5 \times 0.5 = 0.25$

Iteration N: r.m.s field error =  $0.5^N = \frac{1}{2^N}$

Finally the program will stop the iteration when the difference in field amplitudes or the r.m.s field error in successive iteration is less than some value determined by acceptable errors which provide the highest photon flux density at each harmonic of the radiation. In this study the photon flux density will be kept 90 % of ideal photon flux density at each harmonic. Chapter IV will describe more about the acceptable error at each harmonics. Therefore to reach high photon flux density at all harmonics, the r.m.s field error should be less than 0.1 % normalized to ideal field amplitude.

### 3.4.1 Mathematic algorithm of field error correction

Here we assume that the correction method for field errors by using correction coils and varying iron content of the undulator pole is a deterministic problem. If the problem is deterministic, then we can solve this problem by standard techniques of linear algebra (William, 2007). An algorithm of the program can be described in a simple way. If now we consider a small undulator with three poles and three locations of correction. Each correction technique has different effect on

the undulator field. Such the correction coils and inserted slits into back site of undulator poles produce localized change in the field amplitudes. For the correction coil technique, three correction coils for each pole are required with independent excitation current through the coils. Now we start correction at the first pole, perturbation on the field amplitude is not exactly localized, therefore there are changes in the field strength at all three poles. These changes are described with  $a_{11}$ ,  $a_{21}$  and  $a_{31}$ . Since the field strength is linearly dependent on strength of correction coil (and iron content in the pole), if the correction coil has strength  $s_1$ , changes in field strengths at the  $i^{th}$  pole as

$$b_1 = a_{11}s_1$$

$$b_2 = a_{21}s_1$$

$$b_3 = a_{31}s_1$$

Because this problem is assumed to be linear, the field strength changes at each pole is sum of the perturbations due to each correction coil. Thus the field changes of all poles caused by the correction coil strengths  $s_1$ ,  $s_2$  and  $s_3$  are

$$b_1 = a_{11}s_1 + a_{12}s_2 + a_{13}s_3$$

$$b_2 = a_{21}s_1 + a_{22}s_2 + a_{23}s_3$$

$$b_3 = a_{31}s_1 + a_{32}s_2 + a_{33}s_3$$

These equation can be expressed in matrix form by

$$b = As \tag{3.6}$$

where the correction field  $b$  and  $s$  are column vector

$$b = \begin{pmatrix} b_1 \\ b_2 \\ b_3 \end{pmatrix}, s = \begin{pmatrix} s_1 \\ s_2 \\ s_3 \end{pmatrix}$$

and  $A$  is the matrix

$$A = \begin{pmatrix} a_{11} & a_{12} & a_{13} \\ a_{21} & a_{22} & a_{23} \\ a_{31} & a_{32} & a_{33} \end{pmatrix}$$

From calculation, we know the values of elements of the matrix  $A$ . If the correction coil is added at the different poles, the values of  $b$  of field can be calculated by using (3.6). However we would like to know the correction strength of the coil (or iron content) to use to compensate field error  $b$  at each pole. Therefore, we have to deal with an inversion of the matrix  $A^{-1}$ . Because of identity matrix  $I$ , the matrix  $A$  is invertible that is

$$AA^{-1} = A^{-1}A = I$$

We multiply both sides of equation (3.6) by  $A^{-1}$ , thus

$$s = A^{-1}b \tag{3.7}$$

Finally the strength of the correction coil at each pole  $i^{th}$  can be computed by finding the inverse of the matrix  $A$ .

### **Eigenvectors and eigenvalues**

The solution technique given above is sufficient to solve a deterministic linear problem, however we find another method to solve this problem by using eigenvectors and eigenvalues. First we determine the eigenvectors and eigenvalues of the problem and then project the vectors onto the eigenvectors and allow the linear matrix  $A$  to operate on these eigenvectors. Finally we reconstruct the vectors from the eigenvectors, which are now multiplied by their eigenvalues, to get final solution. This method is useful for explanation a Singular Value Decomposition (SVD) which is used and discussed later. The SVD is a method to find solution of

a linear system in a least square sense and diagonalize a problem in a given matrix and provide a singular or near to the singular solving singular matrix.

With an assumption that the matrix  $A$  is invertible, eigenvector  $v$  is a vector such that a product of  $AV$  is multiple of  $v$ , that is

$$Av = \lambda v \quad (3.8)$$

The eigenvector  $v$  of  $A$  has eigenvalue  $\lambda$  thus, this expression rewrite as

$$(A - \lambda I)v = 0 \quad (3.9)$$

This has a solution only if

$$\det(A - \lambda I) = |A - \lambda I| = 0 \quad (3.10)$$

From (3.10), the eigenvalues are solved and substitute into (3.9) to find the eigenvector  $v$  corresponding to that eigenvalue. If the vector  $s$  in Equation (3.6) is a multiple of an eigenvector  $v$ ,  $b$  is also a multiple of  $v$ . So that

$$b = c\lambda v$$

In the linear problem defined by the matrix  $A$ , eigenvectors are the natural basis vectors of the problem. The eigenvectors are orthogonal to each other and any vector in the problem can be decomposed into a unique of the eigenvectors. As this reason,  $b$  is a multiple of an eigenvector and

$$b = dv$$

Since  $A$  only takes eigenvectors into eigenvectors,  $s$  must also be multiple of  $v$ . We calculate

$$\begin{aligned} As &= b \\ &= dv \\ &= d\lambda^{-1}Av \end{aligned}$$

$$\text{or } A(s - d\lambda^{-1}v) = 0$$

Because  $A$  is invertible, therefore

$$s = d\lambda^{-1}v$$

For  $\lambda \neq 0$ , if  $v$  is an eigenvector of the forward problem, such as given in Equation 3.6 with eigenvalue  $\lambda$  then  $v$  is also an eigenvector of the inverse problem given in Equation 3.7 with its eigenvalue of  $\lambda^{-1}$ .

For example, we consider an undulator which has two poles and a field error correction with strengths of two correction coils  $s_1$  and  $s_2$ . A correction coil in position  $s_1$  produces a field strength of say 3 and 2 in the first and second poles, respectively. The correction of unit strength in position  $s_2$  produces a field strength of 1 in the first pole and 2 in the second pole. Therefore a matrix  $A$  is

$$A = \begin{pmatrix} 3 & 1 \\ 2 & 2 \end{pmatrix}$$

The problem in the matrix form is

$$\begin{pmatrix} b_1 \\ b_2 \end{pmatrix} = \begin{pmatrix} 3 & 1 \\ 2 & 2 \end{pmatrix} \begin{pmatrix} s_1 \\ s_2 \end{pmatrix}$$

We can find eigenvalues of  $A$  by using (3.9) as

$$\begin{pmatrix} 3 - \lambda & 1 \\ 2 & 2 - \lambda \end{pmatrix} v = 0$$

Eigenvalues of the eigenvector  $v$  are

$$\lambda_1 = 4$$

$$\lambda_2 = 1$$

The eigenvector  $v_1$  corresponding to eigenvalue  $\lambda_1 = 4$  is

$$\begin{pmatrix} -1 & 1 \\ 2 & -2 \end{pmatrix} \begin{pmatrix} v_{11} \\ v_{21} \end{pmatrix} = 0$$

Then it gives  $-v_{11} + v_{21} = 0$ . Normalizing this vector therefore, we obtain

$$v_1 = \begin{pmatrix} v_{11} \\ v_{21} \end{pmatrix} = \begin{pmatrix} \frac{\sqrt{2}}{2} \\ \frac{\sqrt{2}}{2} \end{pmatrix}$$

As similar with the eigenvalue  $\lambda_2 = 1$ , a normalized eigenvector  $v_2$  is

$$v_2 = \begin{pmatrix} v_{21} \\ v_{22} \end{pmatrix} = \begin{pmatrix} \frac{\sqrt{5}}{5} \\ -\frac{2\sqrt{5}}{5} \end{pmatrix}$$

A matrix  $V$  constructed by two column vector  $v_1$  and  $v_2$  can be written by following

$$V = \begin{pmatrix} v_{11} & v_{21} \\ v_{21} & v_{22} \end{pmatrix} = ( v_1 \quad v_2 )$$

Now if the matrix  $A$  operate on the eigenvector  $V$ , then we obtain

$$\begin{aligned} AV &= A_1( v_1 \quad v_2 ) \\ &= ( \lambda_1 v_1 \quad \lambda_2 v_2 ) \\ &= ( v_1 \quad v_2 ) \begin{pmatrix} \lambda_1 & 0 \\ 0 & \lambda_2 \end{pmatrix} \\ &= V\Lambda \end{aligned}$$

where  $\Lambda$  is a diagonal matrix of the eigenvalues of the matrix  $A$  and  $V$  is invertible.

We use this relation into (3.6) we get

$$\begin{aligned} As &= b \\ &= AVV^{-1}s \\ &= V\Lambda V^{-1}s \end{aligned}$$

It has shown that

$$A = V\Lambda V^{-1} \tag{3.11}$$

and also

$$\Lambda = V^{-1}AV$$

Eventually we can solve the strength of the correction coils  $s$  corresponding to the changes in field strength  $b$  at each pole with using this method and substitution (3.11) into (3.6). By solving the strength of the correction coil corresponding to the field changes at the  $i^{th}$  pole, we obtain

$$s = V\Lambda^{-1}V^{-1}b \quad (3.12)$$

Now we require problems with an invertible problem matrix  $A$  and non-zero eigenvalues. This requires, first of all, that the matrix is square; otherwise an inverse of a matrix is not even defined. A square matrix  $A$  exists when the number of the problem inputs equal the number of problem outputs. If these two numbers are different, the matrix will be a rectangular matrix. Second, all of the columns of the matrix must be linearly dependent. Each column can be thought of as a vector of the problem. It means that the vector must be able to be represented by a combination of the column vectors of the matrix. If the vectors are linearly dependent, then there are vectors that cannot be represented by a linear combination to the column vectors. In our example, there are three correction coils to compensate the field errors at three poles, thus the response matrix for the correction is 3 by 3 and the matrix is square. If a correction coil of unit strength in position  $s_1$  produce fields  $b_1^T = [2, 1, 0]$ , one in  $s_2$  produces  $b_2^T = [1, 1, 1]$  and one in  $s_3$  produces  $b_3^T = [0, 1, 2]$ , the equation relating strengths

of the correction coils to the field produced is

$$\begin{aligned}
 b &= (b_1 \ b_2 \ b_3) s \\
 &= \begin{pmatrix} 2 & 1 & 0 \\ 1 & 1 & 1 \\ 0 & 1 & 2 \end{pmatrix} s \\
 &= As
 \end{aligned} \tag{3.13}$$

where  $A$  is the response matrix. This means that the columns are linear dependent. Furthermore the rows are linearly dependent as well.  $A$  has one redundant dimension; the dimension of  $A$  is 3, however its rank is 2. The reduced rank means that the field strengths at all three poles are unable to be specified independently.

### Singular Value Decomposition

We can find the best solution to the inverse problem in the least square sense by using Singular Value Decomposition (Gilbert, 1988; Sebek, 2009). If there are several solutions that may exist because the problem is underdetermined, SVD will find the shortest vector that solves the equation. In our case of equation 3.13 given a desired solution  $b_{des}$ , there are an infinite number of combinations of the vectors  $b_1, b_2, b_3$  that result in  $b_{des}$ . The SVD uses the combination that is the shortest. If there are no solution to the desired vector, then the SVD will find the closes possible solution to this vector. The SVD is practical method used to solve a problem dealing with correction of field errors of undulator to obtain a uniform field amplitude along the undulator. Here if the correction coils charged with different current is used at each pole of the undulator, we have one correction per pole. This means that the vector  $s$  has dimension as the vector  $b$ . Thus the matrix  $A$  is a square matrix. With using the SVD, the best fit solution will give us the desired field correction to obtain a desired value of r.m.s field error as described

in (3.5). However if we can only place one correction coil on some of the poles and nothing on others, then we do not have enough degree of freedom to correct the error. In this case the best fit solution of the SVD will find the solution that is closest to the desired field correction in the sense that given the location of the correction coil.

Usually the SVD works with symmetric matrices. A square and symmetric matrix  $AA^T$  and  $A^T A$  can be constructed from any arbitrary matrix  $A$ . Any  $m$  by  $n$  matrix  $A$  can be factored into a product of three matrices

$$A = V_1 \Lambda V_2^T \quad (3.14)$$

where  $V_1$  and  $V_2$  are square orthogonal matrices and  $\Lambda$  is a diagonal matrix.  $V_1$  is an  $m$  by  $m$  matrix, the columns of which are the eigenvectors of  $AA^T$  and  $V_2$  is an  $n$  by  $n$  matrix, the columns of which are eigenvectors of  $A^T A$  and  $\Lambda$  is an  $m$  by  $n$  diagonal matrix, the diagonal elements of which are the square roots of non-zero eigenvalues of both  $AA^T$  and  $A^T A$ . Therefore  $\Lambda \Lambda^T$  is an  $m$  by  $m$  diagonal matrix with  $\lambda_i^2$  non-zero diagonal elements and  $\Lambda^T \Lambda$  is an  $n$  by  $n$  diagonal matrix with the same diagonal elements.

If the problem can be described by a square or non-degenerate matrix, we can use the matrix inversion such as Equation 3.7 or 3.12. However if the response matrix of the problem is symmetric, the matrix can be factored with

$$b = V \Lambda V^T s \quad (3.15)$$

but for the SVD method, the matrix is factored with Equation 3.14. If the response matrix  $A$  is invertible, these two factorizations should be equal. However if  $A$  is either rectangular or otherwise, not invertible, the SVD is required to solve the problem of the field correction. The SVD factorization typically arranges the eigenvectors such that the eigenvalues in the matrix  $\Lambda$  are sorted from largest

to smallest. Because these eigenvalues are square roots of non-negative numbers, therefore they are real number also and non negative. To inverse the matrix  $A$  in MATLAB when  $A$  is not invertible, we now use the *pseudo-inverse* of  $A$  to find the best approximation to obtain the small r.m.s field error. The pseudo-inverse is expressed with

$$pinv(A) = V_2 \Lambda^{-1} V_1^T$$

where  $\Lambda^{-1}$  is  $n$  by  $m$  matrix with non-zero elements only on diagonal. For diagonal elements of  $\Lambda$  such that  $\lambda_i \neq 0$ , the corresponding diagonal element of  $\Lambda^{-1}$  is  $\lambda_i^{-1}$ . For diagonal element of  $\Lambda$  which are zero, the corresponding elements of  $\Lambda^{-1}$  are also zero. Therefore, there are no undefined elements of the pseudo-inverse. The pseudo-inverse matrix forces the eigenvalues of the inverse matrix to zero for eigenvectors which cannot contribute to the best fit of the problem.

# CHAPTER IV

## SYNCHROTRON RADIATION AND INSERTION DEVICES

Radiation from moving electrons at uniform velocities is known as the Coulomb regime, drops off very fast, like  $1/r^2$  where  $r$  is the distance from the electron. But here, we are interested in radiation far away from the source. The radiation regime, where radiation drop off like  $1/r$ . Radiation in this regime is generated by accelerated charges. Such acceleration exists in a storage ring where electrons are deflected (accelerated) by a magnetic field. In order to store and guide the electrons circulating in a storage ring, transverse magnetic fields from bending magnets are required. The magnetic field introduces transverse acceleration or a change in the transverse velocity generating an electric field ( $E$ ) which is orthogonal to the magnetic field ( $B$ ). The radiation can be produced both from bending magnets and insertion devices. The radiation spectrum emitted from bending magnets covers a broad spectrum of wavelength from microwaves to the hard x-ray region and is characterized by the so called critical photon energy at which the intensity falls off exponentially. The critical photon energy  $\varepsilon_c = \hbar\omega_c$  is given by

$$\varepsilon_c[keV] = 0.665E^2[GeV^2]B[T] \quad (4.1)$$

At the SPS ring with the electron beam energy and current of 1.2 GeV ( $\gamma = 2348$ ) and 0.2 A, an emitted radiation from bending magnet with field strength and radius of 1.44 T and 2.78 m, respectively with the critical photon energy  $\varepsilon_c = 1.37$  keV is shown in Figure4.1. We can see clearly that the radiation spectrum from the

bending magnet covers over broad spectrum in VUV to X-ray regime. However at the critical photon energy the radiation emitted from the bending drops off exponentially.

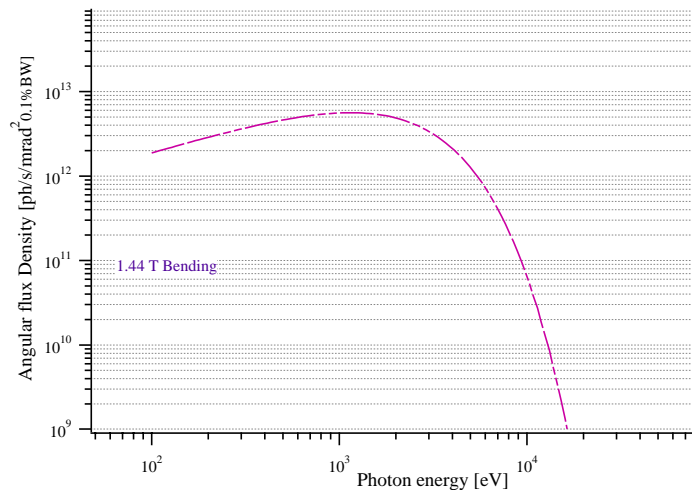


**Figure 4.1** Angular flux density spectrum emitted from a bending magnet with a field strength of 1.44 T and electron beam energy of 1.2 GeV.

To reach hard x-rays, high beam energy and high magnetic fields are required. However, the magnetic strength of bending magnets cannot be varied freely because of the geometry of the storage ring. Thus, to get flexibility, insertion devices such as multipole wigglers, Wave-Length Shifters (WLS) and undulators have been developed and can be inserted into a straight section of the storage ring. Such insertion devices must not alter the overall deflection of the beam and are therefore characterized by the requirement that

$$\int_{-\infty}^{\infty} B_y \cdot dz = 0$$

Consisting of a series of short dipole magnets with alternating magnetic fields, both undulators and wigglers can provide high angular flux density of the radiation. Due to interference of the emitted photons in the undulator, the radiation is quasi-monochromatic and the brightness scales like  $N^2$  where  $N$  is the number of the

undulator periods.

#### 4.1 Electron motion in an undulator field

The magnetic field in the undulator is approximated as a pure sinusoidal function and defined with

$$B_y(z) = B_0 \sin\left(\frac{2\pi z}{\lambda_p}\right) \quad (4.2)$$

where  $\lambda_p$  and  $B_0$  are undulator period length and peak field amplitude of the undulator, respectively. In the presence of magnetic fields the electrons travels along the z-axis with velocity  $v = (v_x, 0, v_z)$ . This motion is a result from the Lorentz force.

$$\vec{F} = \dot{\vec{p}} = \gamma m \dot{\vec{v}} = e(\vec{v} \times \vec{B})$$

where  $\gamma = E/E_0$ ,  $E_0$  and  $m$  are electron rest energy and mass, respectively. From this result we can get

$$\dot{v}_x = -\frac{e}{m\gamma} v_z B_y$$

and

$$\dot{v}_z = \frac{e}{m\gamma} v_x B_y$$

Using the chain rule and assumption that  $v_z \approx \beta c$  is constant, the time variable can be replaced by the variable  $z$  and the equation of electron motion in the undulator is written by

$$\begin{aligned} \frac{d^2}{dz^2} x(z) &= -\frac{e}{m\gamma\beta c} \cdot B_y = -\frac{eB_0}{m\gamma\beta c} \sin\left(\frac{2\pi z}{\lambda_p}\right) \\ \frac{d}{dz} x(z) &= \frac{e}{m\gamma\beta c} \cdot I_1 = \frac{eB_0\lambda_p}{2\pi m\gamma\beta c} \cos\left(\frac{2\pi z}{\lambda_p}\right) \end{aligned} \quad (4.3)$$

$$x(z) = -\frac{e}{m\gamma\beta c} \cdot I_2 = \frac{eB_0\lambda_p^2}{4\pi^2 m\gamma\beta c} \sin\left(\frac{2\pi z}{\lambda_p}\right) \quad (4.4)$$

The first field integral describes the deflecting angle of the electron trajectory

$$I_1 = -\int_{-\infty}^{\infty} B_y(z) dz \quad (4.5)$$

and the second field integral the displacement of the electron trajectory.

$$I_2 = \int_{-\infty}^{\infty} dz \int_{-\infty}^z B_y(\alpha).d\alpha \quad (4.6)$$

In an ideal case, the electron beam moves through the undulator with zero deflecting angles at entrance and exit. Following this condition at  $z=0$ , the maximum deflecting angle within the undulator is

$$\begin{aligned} \frac{dx}{dz} = \alpha(z) &= \frac{K}{\gamma} \cos\left(\frac{2\pi z}{\lambda}\right) \\ \alpha_{\max}(z) &= \frac{K}{\gamma} \end{aligned} \quad (4.7)$$

With a deflecting parameter  $K = \frac{eB_0\lambda_p}{2\pi mc}$  and  $\beta \approx 1$ , it can be written as

$$K = 0.934\lambda_p[cm]B_0[T] \quad (4.8)$$

An undulator is characterized by  $K \leq 1$  because of the weak magnetic field and the electron beam traveling through the undulator field is weakly deflected within an angle of  $\pm 1/\gamma$  resulting in non-relativistic motion in transverse plane. Therefore, the radiation is emitted into a narrow cone with a typical opening angle for the radiation of  $\pm 1/\gamma$ . The continuous sinusoidal trajectory of the electron corresponds to the emission of monochromatic radiation into a line spectrum with a narrow frequency spread. Because of the finite number of undulator periods  $N$  the radiation is quasi-monochromatic with a relative spectral bandwidth defined by

$$\left(\frac{\Delta\lambda}{\lambda}\right) = \frac{1}{N} \quad (4.9)$$

If  $K$  is increased either by increasing the undulator period length  $\lambda_p$  or the magnetic field  $B$ , the electron will be deflected with a larger angle. Thus, each half period of oscillation seems to be the source of the radiation resulting in radiation spread within a larger angle  $K/\gamma$ . We can detect emitted radiation only near the peaks of the oscillation corresponding to position of magnet poles. Because of strong

acceleration by the magnetic field, the electric radiation field is strongly peaked resulting in containing more harmonics of the radiation. As in a wiggler magnet, radiation is emitted with a large opening angle  $\vartheta > \pm\frac{1}{\gamma}$ , so the radiation consists of large number of harmonics which, at high harmonics, merge together. As a consequence, the radiation is very broad similar to that from a bending magnet.

## 4.2 Undulator radiation

The magnetic field in the undulator is weak guiding the electron trajectory into a pure sinusoidal motion. An observer in the electron frame sees electric radiation fields generated in a continuous sinusoidal fashion corresponding to an oscillation given by the Lorentz contracted period length in the electron frame. The source of the radiation, being the electron, is moving toward the observer and the radiation wavelength observed in the rest (laboratory) reference frame appears contracted by the Doppler effect. This results in a frequency shift of the radiation spectrum. The frequency depends on the angle  $\theta$  between electron velocity and observation direction. If we observe the radiation on axis the radiation frequency is Doppler shifted by a factor of  $1/2\gamma$  and the observed undulator radiation frequency is

$$f_1 = \frac{2\gamma^2 c}{\lambda_p}$$

where  $f_1$  is the fundamental frequency on axis in the laboratory frame. If we detect the radiation emitted off-axis ( $\theta \neq 0$ ), the frequency is red-shifted to a lower value. The frequency expressed in term of the observation angle is then

$$f_1 = \frac{f_1^*}{\gamma(1 - \beta\cos\theta)} = \frac{c}{\lambda_p(1 - \beta\cos\theta)} \quad (4.10)$$

where  $\beta \equiv \frac{v}{c}$ . For small angles we can use a Taylor expansion  $\cos\theta = 1 - \frac{\theta^2}{2} + \dots$  and get the fundamental frequency at any observation angle as

$$f_1 = \frac{2c\gamma^2}{\lambda_p(1 + \gamma^2\theta^2)}$$

Correspondingly, the radiation spectrum has a wavelength of

$$\lambda_1 = \frac{\lambda_p}{2\gamma^2}(1 + \gamma^2\theta^2) \quad (4.11)$$

At this result, it can be noted that the radiation wavelength is increased by a factor of  $1 + \gamma^2\theta^2$ . Thus to reach a high frequency, it is necessary to detect the radiation on-axis. If the field strength is further increased ( $K$ ), the electron is deflected transversely with a large oscillation amplitude and we have a composite of transverse and longitudinal acceleration as shown in Figure 4.2. Thus an observer only detects radiation near the peak of the electron trajectory as a periodic train of short pluses. Due to the symmetric distortion of the transverse component there

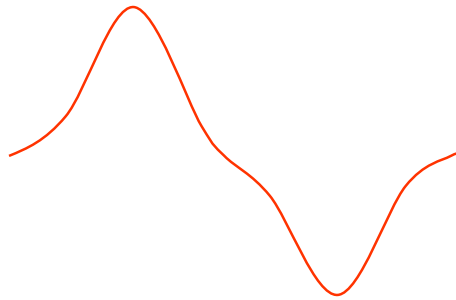


**Figure 4.2** Distortion of pure sinusoidal motion due to the relativistic transverse motion.

are only odd harmonics. However, each transverse period consists of two longitudinal oscillations having a path like a figure of eight. The longitudinal motion occurs at twice the frequency of the transverse motion causing even harmonics to appear. Finally, the radiation line spectrum for a stronger undulator is composed of two series of harmonics, one includes the odd harmonics and the other one the even

harmonics. The odd harmonics are concentrated on the axis within an opening angle of  $\pm 1/\gamma$  but the even harmonics are distributed in a ring off axis as shown in Figure 4.3. If  $K$  is further increased the electric field becomes more distorted in

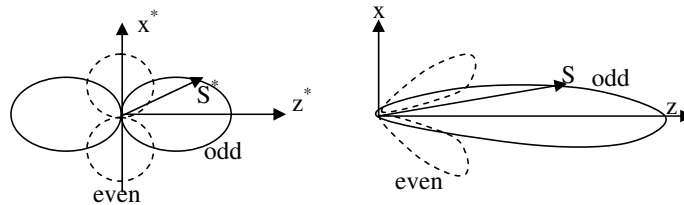


**Figure 4.3** Distribution of dipole radiation field due to odd and even harmonics in the case of a strong undulator in the moving coordinate (left) and in the laboratory coordinate (right).

the transverse plane forming a sharp peak and the radiation spectrum will contain more and more harmonics. Figure 4.4 shows a comparison of the electric field distortion with increasing field strength or the  $K$  value.

As a consequence at very large  $K$  the number of harmonics is so large that the radiation spectral lines merge together into a continuous spectrum like the radiation spectrum from a bending magnet, Wave-Length Shifter and wiggler magnet. A wiggler produces a line spectrum just like an undulator and is therefore just a strong undulator. For the wiggler magnet, the emitted radiation mostly used at very high harmonics due to the high value of  $K$ . To reach the hard x-ray regime of the radiation emitted from the undulator,  $K$  should be larger than 2-3. In practice each half of the oscillation period of the electron trajectory emits radiation within an angle of  $\pm 1/\gamma$ . This will lead to interference of the radiation only on-axis. The interference of two wavefronts of the radiation is shown in Figure 4.5, where the electron moves through the undulator with the average longitudinal velocity  $\bar{\beta}_z$  while following a sinusoidal path. The electron emits a photon at A and in the time  $\tau = \lambda_p/c\bar{\beta}_z$  it travels to B where it also emits a photon. During

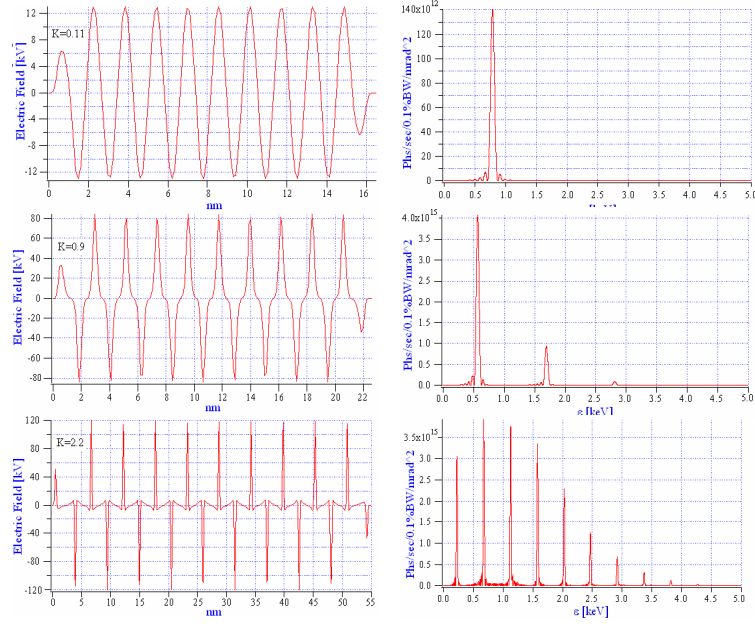


**Figure 4.4** Electric field seen by the observer on axis for the electron (left) and associated angular flux density calculated at beam energy of 2 GeV, period length of 48 mm and number of period of 10 with varying values of  $K$ . For small values the electric field is nearly sinusoidal corresponding to a single line in the spectrum but for a large value of  $K$  the electric field is distorted into a sharp peak resulting in a large number of harmonic lines in the spectrum.

this time the first wavefront travels the distance

$$S_{ph} = \lambda_p / \bar{\beta}_z$$

with an angle  $\theta$  to the  $z$ -axis. Thus, the two wavefronts are separated by a spacing  $d$  defined by

$$d = S_{ph} - \lambda_p \cos\theta \quad (4.12)$$

Therefore, constructive interference of radiation emitted from different points occurs when the spacing is an integer number of the wavelength

$$n\lambda_n = \lambda_p \left[ \frac{1}{\bar{\beta}_z} - \cos\theta \right] \quad (4.13)$$

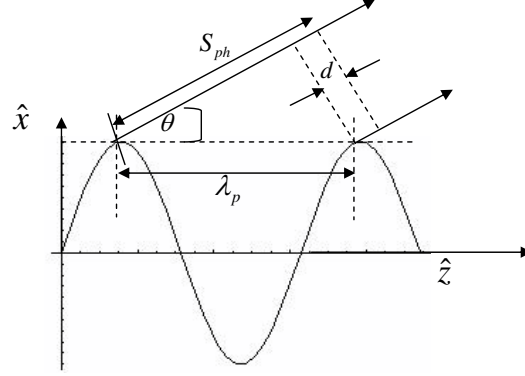


**Figure 4.5** The electron trajectory on the deflecting plane in the undulator emit radiation at position A and B.

The average velocity (James, 2004) in forward direction is simply as

$$\bar{\beta}_z \sim \beta - \frac{K^2}{4\beta\gamma^2} \sim 1 - \frac{1}{2\gamma^2} - \frac{K^2}{4\beta^2\gamma^2}$$

and using this expression in (4.13) with the Binomial expansion  $(1 - x)^{-1} = 1 + x$  we obtain

$$\begin{aligned} n\lambda_n &\sim \lambda_p \left[ \left( 1 + \frac{1}{2\gamma^2} + \frac{K^2}{4\beta^2\gamma^2} \right) - \cos\theta \right] \\ &\sim \lambda_p(1 - \cos\theta) + \frac{\lambda_p}{2\gamma^2} + \frac{\lambda_p K^2}{4\beta^2\gamma^2} \end{aligned}$$

From the identity of  $1 - \cos\theta = 2\sin^2(\theta/2)$  and for small angle  $\sin\theta \sim \theta$  this expression becomes

$$\lambda_n = \frac{\lambda_p}{2\gamma^2 n} \left( 1 + \gamma^2 \theta^2 + \frac{K^2}{2} \right) \quad (4.14)$$

In practical units the emitted radiation wavelength corresponding to the photon energies for the  $n^{\text{th}}$  harmonics are expressed by

$$\lambda_n[\text{\AA}] = 13.056 \frac{\lambda_p[\text{cm}]}{nE^2[\text{GeV}^2]} \left( 1 + \frac{K^2}{2} + \gamma^2 \theta^2 \right) \quad (4.15)$$

$$\varepsilon_n[\text{eV}] = 950 \frac{nE^2[\text{GeV}^2]}{\lambda_p[\text{cm}] \left( 1 + \frac{K^2}{2} + \gamma^2 \theta^2 \right)} \quad (4.16)$$

From (4.15) and (4.16) we can see clearly that the radiation emitted off-axis with the angle is red-shifted to longer wavelengths of the radiation and the photon energy (frequency) shifts to lower values. Furthermore, even harmonics appear on the line spectrum as shown in Figure 4.6 when the observation angle is off-axis. Only little comparably peaks of the even harmonics appear on the angular flux density spectrum. It means that most of the emitted radiation is concentrated only on the axis generated mainly by the odd harmonics. As we know, the radiation of the odd harmonics, to reach the hard x-ray regime with the high flux density or brightness, should be observed on-axis or in the forward direction  $\theta = 0$ . Furthermore  $K$  and the observation angle  $\theta$  is a function of the fundamental wavelength of the radiation (and wavelength of the other harmonics) as shown in Figure 4.7. The radiation wavelength strongly depends on the undulator period length  $\lambda_p$ ,  $K$

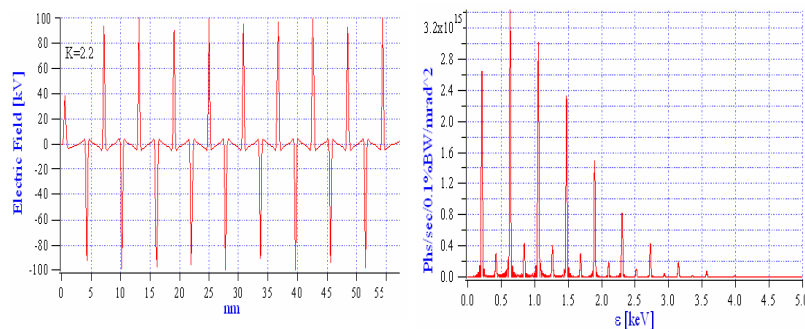


**Figure 4.6** Electric field (left) seen by the observer off axis and associated angular flux density calculated at a beam energy of 2 GeV (right) with vertical and horizontal opening angle of 0.5 and 0.0 respectively and deflecting strength  $K$  of 2.2.

and  $\theta$ . Thus, to get high photon energies, we should observe the radiation on-axis, optimize  $K$  and the period length. Due to a quadratic increase of the radiation wavelength with  $K$  especially for long  $\lambda_p$ , a reduction of the period length leads the shorter wavelengths and high photon energies. However, a reduction of  $\lambda_p$  has

been limited because a finite magnetic gap  $g$  must be provided for the vacuum chamber. As the period length becomes smaller than the gap the magnetic field drops off significantly. Eventually, the  $K$ -parameter should be sufficiently high to allow short period length and the generation of higher harmonics (up to 7<sup>th</sup>) of the photon radiation.

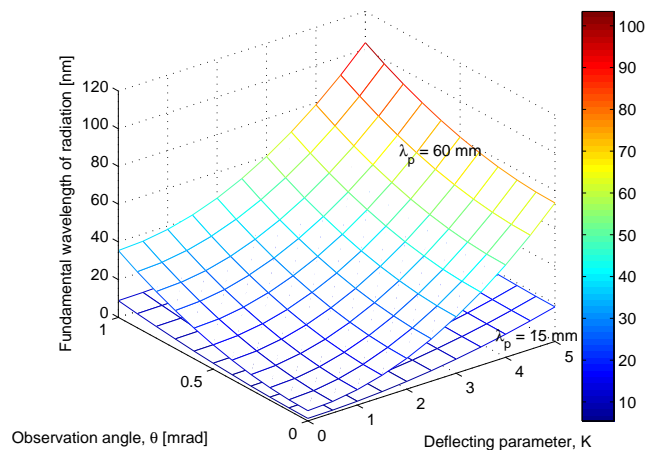


**Figure 4.7** Fundamental wavelength as a function of changing the parameter  $K$  and observation angle  $\theta$  for an undulator with period length of 60 mm and 15 mm. Electron beam energy is 1.2 GeV.

### 4.3 Line spectrum

A major property of undulator radiation is its narrow width of spectral lines. It means that we consider only an actual harmonic with an actual frequency of the radiation spectrum produced by  $N$  periods of electron oscillation passing through the undulator. Now we consider only the radiation emitting in forward direction  $\vartheta = 0$  therefore, only odd harmonics are confined within the small angle  $\pm 1/\gamma$ . Due to the finite number of oscillations, the spectrum is not quite monochromatic

but has a line width for the  $n^{th}$  harmonic defined as

$$\frac{\Delta\omega_n}{\omega_n} = \frac{1}{nN}$$

### 4.3.1 Angular spectral flux

The total number of photons  $N_{ph}$  emitted into a spectral band width per unit solid angle and time known as angular spectral flux is expressed in terms of a Bessel's function. Based on this condition and identity of the Bessel function (Wiedemann, 2007) the angular flux on-axis for a single electron passing through the undulator is defined by

$$\frac{d\dot{N}_{ph}(\omega)}{d\Omega}\Big|_{\theta=0} = \alpha\gamma^2 N^2 \frac{\Delta\omega}{\omega} \frac{K^2}{(1 + \frac{1}{2}K^2)^2} \sum_{n=1}^{\infty} n^2 \left( \frac{\sin \pi N \Delta\omega_n / \omega_1}{\pi N \Delta\omega_n / \omega_1} \right)^2 J J^2 \quad (4.17)$$

where  $\alpha$  is the fine structure constant and the  $JJ$ -function is defined by

$$\alpha = \frac{e^2}{4\pi\epsilon_0\hbar c}$$

$$J J^2 = \left[ J_{\frac{1}{2}(n-1)} \left( \frac{nK^2}{4 + 2K^2} \right) - J_{\frac{1}{2}(n+1)} \left( \frac{nK^2}{4 + 2K^2} \right) \right]^2 \quad (4.18)$$

This equation can be written in terms of amplitudes of the harmonics given by

$$A_n(K) = \frac{n^2 K^2}{(1 + \frac{1}{2}K^2)^2} J J^2 \quad (4.19)$$

The amplitude of the harmonic is plotted in Figure 4.8 for different  $n^{th}$  harmonics. Since for large  $K$  the function  $A_n(K)$  drops rapidly, the angular flux also decreases. To reach high harmonics (up to  $5^{th}$ ) of the radiation the  $K$  value should be at least 2-3 due to reaching maximum value of the amplitude of the harmonic (the  $3^{rd}$ ,  $5^{th}$ ,  $7^{th}$  and the  $9^{th}$ ). If we would like to achieve the  $13^{th}$  harmonic, the  $K$  should be more than 3 to obtain a high  $A_n(K)$  however, for the low energy storage ring, increasing the  $K$  may be not useful to reach the hard-x-rays. Moreover it is really hard to reach that  $K$  value with a short period length of the undulator.

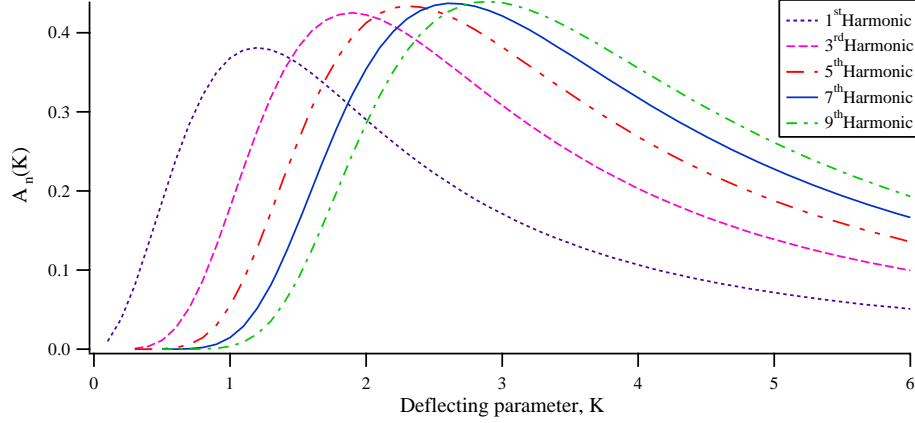


**Figure 4.8** Amplitudes of odd harmonics in the forward direction as a function of the  $K$  values.

The spectral line width at each harmonic is determined by the sinc function  $\sin(\pi Nx)/(\pi Nx)$  where  $x$  is  $\Delta\omega_n/\omega_1$ . The sinc function is sine wave with decaying amplitude like  $1/\pi Nx$ . The spectral width gets narrower with increasing number of undulator periods. Since Equation 4.17 describes the angular flux on-axis for a single electron, to get the total angular photon flux, it has to be multiplied by the number of electrons per second which is  $I/e$  where  $I$  is the electron beam current in the storage ring. Thus we can express the total angular flux on-axis in terms of number of photons per second by dividing by the energy of each photon  $h\omega/2\pi$ . Eventually this is written in terms of a relative bandwidth  $d\omega/\omega$  as

$$\frac{d\dot{N}_{ph}(\omega)}{d\Omega d\omega/\omega}\Big|_{\theta=0} = \frac{e^2 N^2 \gamma^2 I}{4\pi \epsilon_0 c} \frac{2\pi}{e h} \left( \frac{\Delta\omega}{\omega_1} \right) A_n(K) \quad (4.20)$$

In practical unit, the number of photons per solid angle per second on-axis is

$$\frac{d\dot{N}}{d\Omega}\Big|_{\theta=0} = 1.74 \times 10^{14} N^2 E^2 I A_n(K) \quad (4.21)$$

in units of photons per second per  $\text{mrad}^2$  per 0.1 % bandwidth. We note that the photon flux density in the forward direction is proportional to the square of the undulator periods  $N$ . From the sinc function, an r.m.s opening angle in the

vertical axis for each harmonic  $n$  can be defined as

$$\vartheta_n = \frac{1}{\gamma} \sqrt{\frac{1 + K^2/2}{(nN - 1)}}$$

A typical opening angle denoted by  $\sigma_{r'}$  is estimated with an assumption that the angular flux distributes like a Gaussian or normal distribution. Therefore it gives

$$\sigma_{r'} = \frac{1}{\sqrt{2}} \vartheta_n \approx \frac{1}{\gamma} \sqrt{\frac{1 + \frac{1}{2}K^2}{2nN}} \quad (4.22)$$

Based on the assumption that the photon flux density drops to zero when we observe the radiation with an angle exceeding the typical opening angle, thus the r.m.s opening angle will allow an aperture of a pin hole or slit which are used to extract the photon radiation into beamline. For  $K \approx 1$  the opening angle (or pin hole aperture) is

$$\sigma_{r'} = \frac{1}{\gamma \sqrt{nN}}$$

Correspondingly a solid angle defined by the opening angle is used to compute the total photon intensity for the  $n^{\text{th}}$  harmonic within the bandwidth  $\frac{\Delta\omega_n}{\omega_n}$ . Thus total photon flux for the  $n^{\text{th}}$  harmonic in the forward direction is

$$\dot{N}_{ph}(\omega_n)|_{\vartheta=0} = \pi\alpha N \frac{I}{e} \left(\frac{\Delta\omega}{\omega_n}\right) \left(\frac{1 + K^2/2}{n}\right) A_n(K) \quad (4.23)$$

In the practical unit of the photons per second per 0.1 % bandwidth, Equation 4.23 gives the flux emitted into the forward cone as

$$\dot{N}_{ph}(\omega_n)|_{\vartheta=0} = 1.43 \times 10^{14} N I A_n(K) \quad (4.24)$$

In practice, the radiation has to pass a finite aperture of a pin hole before reaching the observer in the forward direction. The pin hole is also important to characterize the radiation. If the pin hole aperture is very narrow, the line spectrum is well defined with the sinc function while the electron beam divergence is ignored. Some even harmonics may exist on the spectrum and also the odd

harmonics of the line spectrum are shifted when the observation angles are off-axis. However somehow we observe the radiation emitted through a large aperture, an angle integrated spectrum (Elleaume and Onuki, 2003) is introduced to exhibit an almost continuous spectrum with spikes at location of the harmonic lines. The angle integrated spectral flux calculated in a finite opening angle  $\theta = \pm 1/\gamma$  for a deflecting parameter  $K = 1.96$  is shown in Figure 4.9. Since radiation of the odd

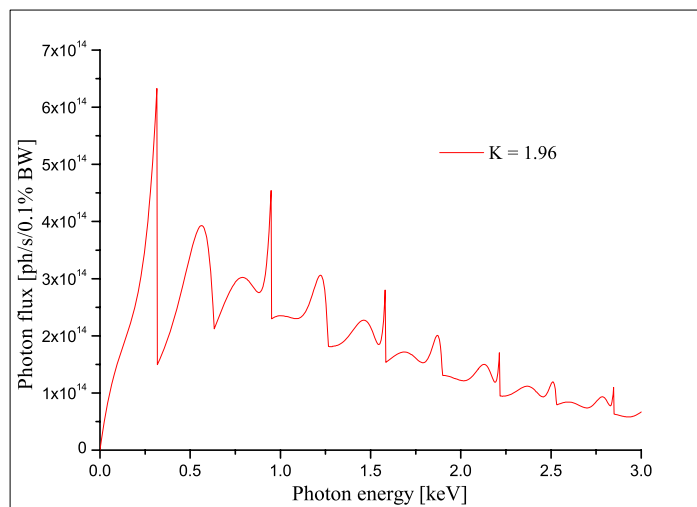


**Figure 4.9** An angular integrated spectrum produced by an undulator with a period length of 15 mm and peak field strength of 1.4 T at an electron beam energy of 1.2 GeV and beam current of 200 mA.

harmonics is distributed over all opening angles we observe at an angle  $\theta = \pm \vartheta$  radiation at a wavelength

$$\lambda_1 = \frac{\lambda_p}{2\gamma^2} \left( 1 + \frac{1}{2}K^2 + \gamma^2\vartheta^2 \right)$$

where  $\vartheta$  is the angle with respect to the axis. The term  $\gamma^2\vartheta^2$  is proportional to a quadratic term of the angle  $\vartheta$ . Thus there is red shift occurring not only for  $+\vartheta$  but also for  $-\vartheta$  causing the shift to the lower energies and an asymmetry of the spectral radiation distribution occurs. On-axis the angular integrated spectrum appears at the location of the fundamental harmonic as a sharp line. Because the

distribution of the even harmonics as a ring off axis with the angle of  $1/\gamma$ , the observation angle becomes

$$\theta = \frac{1}{\gamma} \pm \vartheta$$

The  $\gamma^2\theta^2$  can be approximated by following

$$\gamma^2\theta^2 \approx 1 + 2\frac{\vartheta}{\gamma}$$

Due to the linear relation, the term  $\gamma^2\theta^2$  can be red or blue shifted on the energy spectrum resulting in a symmetric distribution of the angular integrated spectrum when the observation angles are integrated around the even harmonics. Peaks of the harmonics ( $n = 1,3,5,..$ ) cannot be seen clearly even though they are not as sharp as they are observed through the pin hole on-axis. Because of the finite pin hole the emitted radiation does not appear like exactly harmonic lines. Although the pin hole is very narrow, the even harmonics may exist with spikes on the spectrum and the odd harmonics appearing not like a line spectrum due to the finite electron beam emittance and electron beam divergence. Therefore the emitted radiation is observed at an angle occurring by the electron trajectory with respect to the axis of the undulator. Both theoretical and experimental expectations agree well in the characterization of the radiation lines spectrum from undulators.

### 4.3.2 Undulator brightness

The photon flux density in phase space is called the spectral brightness being the number of photons per second, per unit solid angle and per unit source area. Normally, the brightness is widely used to measure the radiated photons because it determines exactly the properties of a source. Moreover the brightness is a sensible source to source comparisons because it is invariant in longitudinal position. The spectral brightness of the undulator radiation is simply the photon

flux in the forward cone divided by a volume of the phase space and defined as

$$B = \frac{\dot{N}_{ph}(\omega)}{4\pi^2 \Sigma_x \Sigma_y \Sigma_{x'} \Sigma_{y'}} \quad (4.25)$$

where effective horizontal  $\Sigma_x$  and vertical  $\Sigma_y$  source size and horizontal  $\Sigma_{x'}$  and vertical  $\Sigma_{y'}$  divergences are defined

$$\begin{aligned} \Sigma_x &= \sqrt{\sigma_x^2 + \sigma_y^2} \\ \Sigma_y &= \sqrt{\sigma_y^2 + \sigma_r^2} \\ \Sigma_{x'} &= \sqrt{\sigma_{x'}^2 + \sigma_{r'}^2} \\ \Sigma_{y'} &= \sqrt{\sigma_{y'}^2 + \sigma_{r'}^2} \end{aligned}$$

with horizontal  $\sigma_x$  and vertical  $\sigma_y$  electron beam sizes and  $\sigma_{x'}$ ,  $\sigma_{y'}$  electron beam divergences. Based on an approximation to the fundamental mode of an optical resonator which is known as Gaussian laser mode (Kim, 1986), the phase space area is

$$2\pi\sigma_r\sigma_{r'} = \frac{\lambda}{2} \quad (4.26)$$

with the photon beam size (Clarke, 2004)  $\sigma_r = \frac{1}{4\pi}\sqrt{\lambda L}$ . Thus the photon beam opening angle is  $\sigma_{r'} = \sqrt{\frac{\lambda}{L}}$ , where  $L$  is the undulator length. The brightness of the undulator radiation will scale with the square of the number of undulator periods  $N$  if only the electron beam size and the divergences in both planes are small and so  $\Sigma_x, \Sigma_y \sim \sigma_r$  and  $\Sigma_{x'}, \Sigma_{y'} \sim \sigma_{r'}$  where the photon divergence is proportional to  $1/\sqrt{N}$ . Finally the brightness can be approximated by

$$B \simeq \frac{\dot{N}_{ph}(\omega)}{4\pi^2 \sigma_r^2 \sigma_{r'}^2} \propto N^2 \quad (4.27)$$

when the photon flux is proportional to the number of the undulator periods  $N$  only and  $\sigma_{r'}^2 \propto 1/N$ .// At high  $K$  values there are many harmonics of the radiation emitted on-axis and to achieve a high photon energy, the parameter  $K$  should be at least 2-3. Furthermore, at these  $K$  values we can obtain high spectral photon

flux of the radiation for each harmonic caused by maximum amplitudes of the harmonics  $A_n(K)$ . To tune the parameter  $K$ , both magnetic field and undulator period length are adjusted however we have to keep in mind that a goal of the tenability is to achieve the x-ray. Thus a reduction on the undulator period length is very reasonable to reach that. Due to a limitation on saturation in iron pole of a permanent undulator, the magnetic field strength cannot be increased up to high field with reduction on the period length at the  $K$  value about 2-3. Generally, the undulator is made from magnetic material such as Samarium-cobalt ( $Sm_2Co_{17}$ ) or Vanadium Permendur (SmCo). The  $Sm_2Co_{17}$  compound has a remanent field of 0.85-1.05 T. For the SmCo using in a hybrid insertion devices composed of hard and soft magnetic materials with the remanent field of 0.9 T. Therefore the maximum magnetic field strength is limited by the magnetic properties of the material. Figure 4.10 performs the peak field achievable of the Samarium-cobalt and the hybrid insertion device by using empirical formula. For an undulator made from Samarium-cobalt material the empirical formula  $B = 1.55 \exp(-\pi g/\lambda_p)$  describes the magnetic field reaching 1 T only for very small gap to period length ratios  $g/\lambda_p$  of about 0.1. This means that the undulator period length has to be quite large compared to the magnetic gap to obtain a high field. Although the undulator strength  $K$  can achieve desirable values. The period length of the undulator has to be increased resulting in an increase of the radiation wavelength which is a cause of photon energy shift to low value. However, keeping a small  $\lambda_p$  to get the  $K = 2$ , the magnetic gap  $g$  has to be reduced to 0.8 cm as shown in Figure 4.11. In practice, the magnetic gap is limited by the vertical size and thickness of the vacuum chamber. This allows a minimum gap only as small as the beam stay clear corresponding to the electron beam. For example, at the SPS ring, a minimum aperture of vacuum chamber is about 26 mm therefore the gap should be more than that value such as 30 mm to reach the  $K = 2$  resulting in a long period

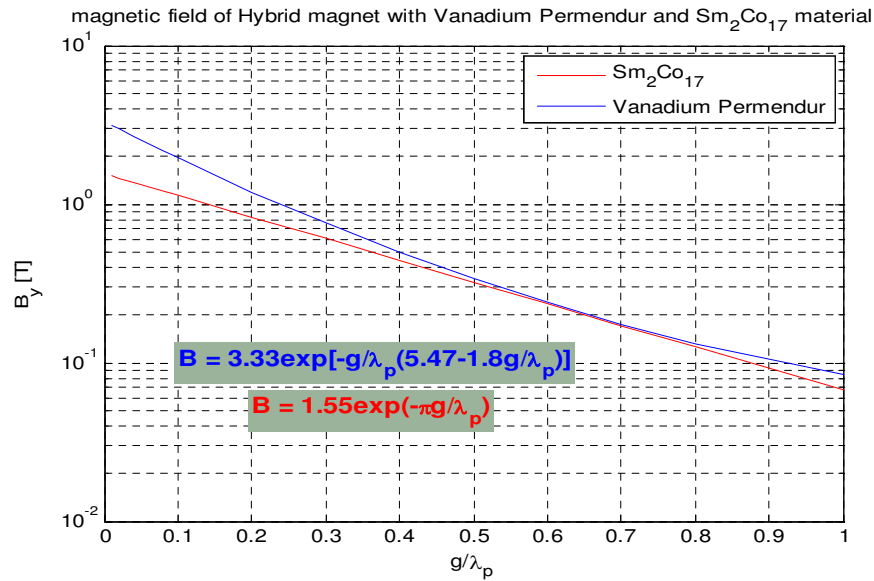


**Figure 4.10** Peak field in mid plane of a permanent magnet undulator made from  $\text{Sm}_2\text{Co}_{17}$  (red line) and for a hybrid with Vanadium Permendur poles (blue line) as a function of magnetic gap ( $g$ ) and undulator period length.

length of the undulator. Thus x-rays cannot be reached by a permanent undulator at the SPS ring. A superconducting wire can be used instead of Samarium-cobalt ( $\text{Sm}_2\text{Co}_{17}$ ) or Vanadium Permendur (SmCo) to produce a high magnetic field with a short period length of a few millimeters. This can be done in a superconducting undulator.

#### 4.4 Superconducting undulator with short period

Undulators are the most advanced sources to generate synchrotron radiation but the maximum field strength of undulators is limited by the material properties of the undulator poles. In a low energy storage ring, the permanent magnet material is replaced with a superconducting wire. Because the superconducting wire has zero electrical resistance, thus there are no Ohmic losses and heating. As a consequence, the wire can carry much higher current densities than a normal

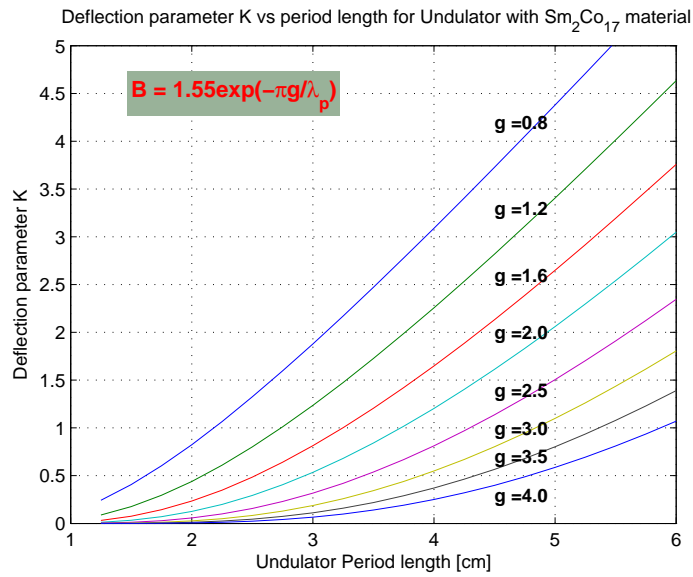


**Figure 4.11** Deflecting parameter  $K$  of different  $g$  in centimeter, as function of undulator period length for a Samarium-cobalt undulator.

conducting wire and a strong magnetic field strength in the Tesla range can be reached. To achieve a high magnetic field strength at short period length we still must use the smallest possible magnetic gap limited only by the electron beam lifetime and injection efficiency. There are several techniques of superconducting wire winding to get as small a period length as possible at a desirable field. A typical superconducting wire is wound around an iron pole as shown in Figure 4.12. The current in neighboring coils has opposite polarity to obtain an alternating vertical magnetic field along the axis. Radiation emitted by the superconducting undulators provides more angular flux density and brightness at high harmonics than emitted by permanent undulators. Figure 4.13 shows a comparison of the angular flux density produced from the permanent undulator and from the superconducting undulator.

In practice, finite tolerances are caused by manufacturing of coil winding into the grooves and position of wire racetracks which are superconducting wires in the grooves. Because of differences of the wire position the magnetic field am-

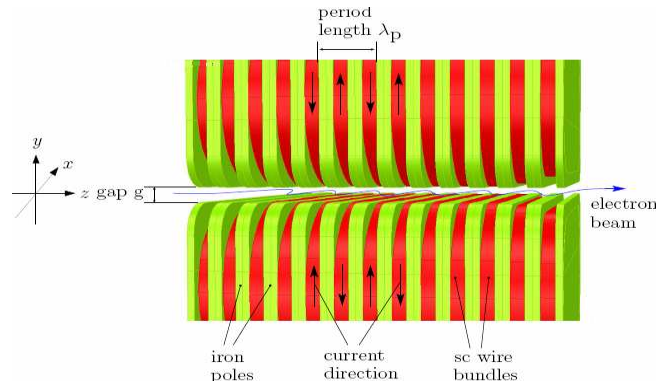


**Figure 4.12** Typical layout of a superconducting undulator (Wollmann, 2008) with iron poles (green), superconductive wire bundles (red), the gap width  $g$  and period length  $\lambda_p$ .

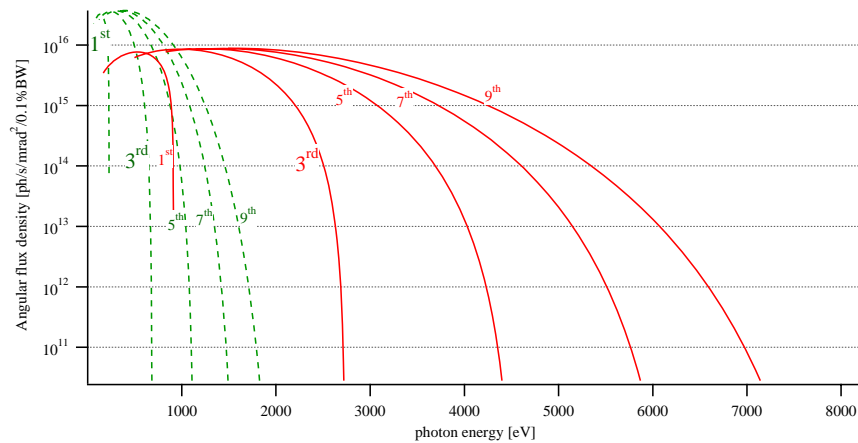


**Figure 4.13** Angular flux density as function of a photon energy, up to the 7<sup>th</sup> harmonic emitted from permanent undulator with period length of 60 mm and field strength of 0.55 T (dash line) and from a superconducting magnet with period length of 15 mm and field strength of 1.4 T (solid line) at electron beam energy and beam current of 1.2 GeV and of 0.2 A, respectively.

plitudes of whole periods are different. Changes in the field amplitudes introduce a disturbance of the pure sinusoidal electron trajectory passing through the undulator. It means that radiation emitted from an imperfect undulator field cannot be superimposed well on-axis resulting in a reduction of the angular flux density

and brightness especially at high harmonics. Furthermore, misaligned undulator poles may introduce a change in undulator period length which is related to the phase. Both the magnetic field and period length errors are cause of a brightness degradation at high harmonics. In this thesis project we propose several techniques to correct such as discussed in Chapter VII. The effect of each error on each harmonic of the radiation has been investigated and tolerance limits on acceptable errors have been derived for each harmonic.

## 4.5 Magnetic field and period length errors

The field and period length errors are important to measure the quality of the magnetic undulator field. To study the effect of the errors on the radiation emitted at harmonics up to the ninth, the undulator field is compared to an ideal sinusoidal magnetic field with a period length of 15 mm and a peak field amplitude of 1.387 T corresponding to the average magnetic field amplitude measured in the test undulator (SCU) and discussed in Chapter VI. The number of undulator periods is 20 consisting of 38 main poles and two end poles which are located at the entrance and exit of the undulator magnet. Field strengths of the end poles are only half those of main poles. Figure 4.14 shows the magnetic field distributed along the undulator axis ( $z$ -axis) as the pure sinusoidal wave.

First, we introduce an r.m.s field error  $\frac{\Delta B}{B_0}$  normalized to the ideal peak field amplitude of 1.387 T of one percent. The field error is converted into a field change  $\Delta B$  at each half period (at the pole number  $i$ ) to generate a real magnetic field. The field errors are introduced randomly at the  $i^{th}$  pole using the RANDN function in MATLAB. The RANDN function generates arrays of random numbers which are distributed as a Gaussian with a zero mean, variance  $\sigma^2 = 1$  and standard deviation  $\sigma = 1$ . Each time this function is called a different set of the random

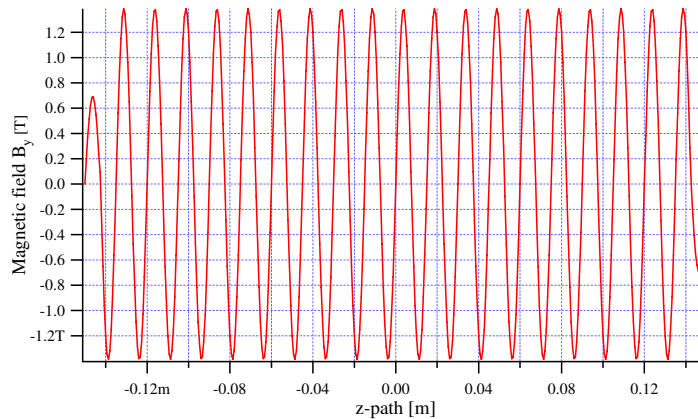


**Figure 4.14** An ideal magnetic field distributed along an undulator with a period length of 15 mm and a peak field amplitude of 1.387 T.

number arrays is generated. Because of the low number of periods and to get proper statistics we need many sets of random numbers to create a real magnetic field distribution along the z-axis. Then the angular flux density for each set of the real fields is calculated by introducing the real field with errors into the program B2E. Eventually an average value of the angular flux at each harmonic is used to calculate a relative reduction in the flux density. The field change generated with a vector of  $2*N$  elements is defined as

$$\Delta B = B_0 \text{randn}(1, 2 * N) \frac{\Delta B / B_0 [\%]}{100} \quad (4.28)$$

Thus the real field including randomly distributed field errors is

$$B_{\text{real} - B} = (B_0 + \Delta B) \sin(kz) \quad (4.29)$$

Figure 4.15 performs a ratio of the real to the ideal angular flux densities as a function of harmonic number of the radiation and r.m.s field error. We can see clearly that the r.m.s field error of 1 % is quite a strong effect on the degradation of the flux density for high harmonics (up to the 7<sup>th</sup>) of the radiation emitted on-axis. It means that only a 1 % r.m.s field error is allowed for the real magnetic field to

still reach 90 % of the ideal angular flux density for harmonics up to 5<sup>th</sup> order. For higher harmonics less errors are tolerable. In other words, the angular flux densities at all harmonics should not be reduced by more than 10 % A r.m.s period length

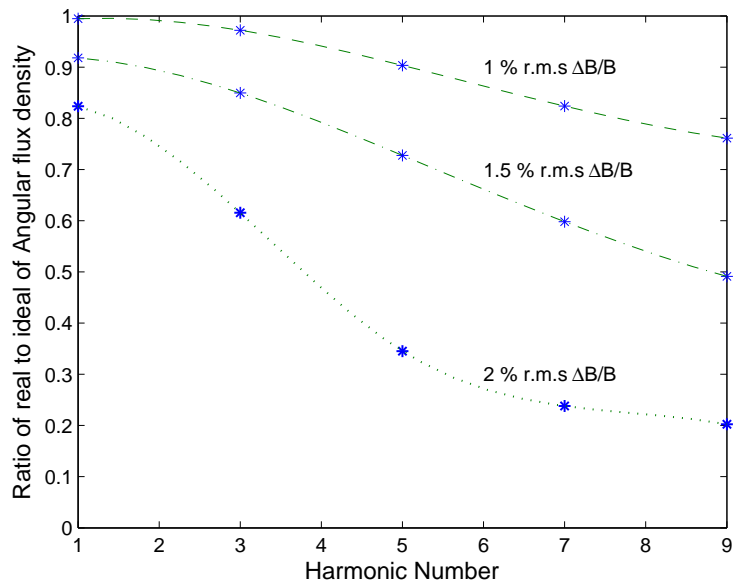


**Figure 4.15** Ratio of real to ideal angular flux densities for each harmonic of radiation emitted into a forward cone represented with stars as a function of r.m.s field error. Lines are used only to guide the eye.

error  $\Delta\lambda_p/\lambda_{p,0}$  is also introduced to the ideal magnetic field to calculate the ratio of the angular flux density for the harmonics of the radiation. The period length error is equivalent to a r.m.s phase error expressed by

$$\frac{\Delta\lambda_p}{\lambda_{p,0}} = \frac{\Delta\varphi}{\langle T \rangle} \quad (4.30)$$

where  $\langle T \rangle$  is an average of undulator period in one period. The average values are  $2\pi$  and 360 in units of radian and degree, respectively. Then we can define a change in undulator period length generated randomly of each period as

$$\Delta\lambda_p = \lambda_{p,0} \text{randn}(1, 2 * N) \frac{\Delta\varphi \text{ [degree]}}{360} \quad (4.31)$$

Finally we get a real magnetic field with a period length error by following

$$B_{\text{real} - \lambda_p} = B_0 \sin(k'z) \quad (4.32)$$

where  $k' = \frac{2\pi}{(\lambda_p + \Delta\lambda_p)}$  for each period. Eventually the ratio of the real to the ideal angular flux densities as a function of harmonic number of the radiation and r.m.s period length error is computed and shown in Figure 4.16.

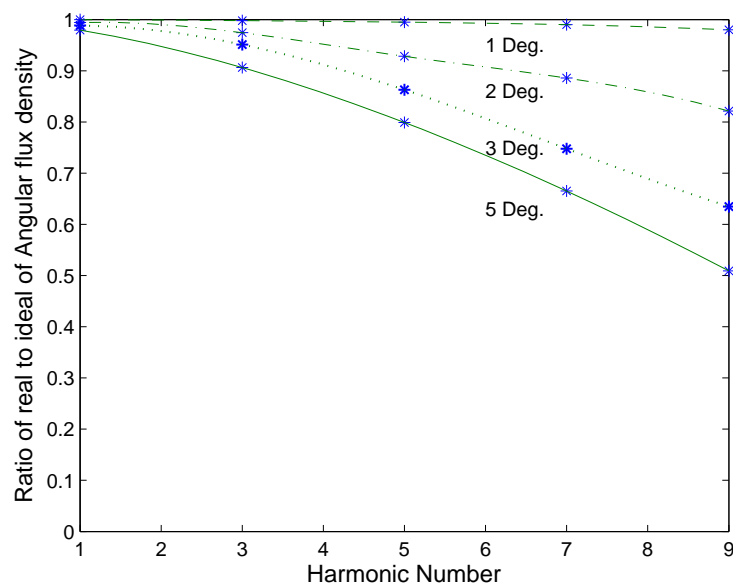


**Figure 4.16** Ratio of real to ideal angular flux densities for each harmonic of radiation emitted into forward cone represented with stars as a function of r.m.s period length error. Lines are used only to guide the eye.

Comparing the angular flux densities with field and phase (period length) errors, a strong reduction on the flux is caused by a change in the magnetic field especially at high harmonics. The electron beam experiences different field strengths from period to the next period while traveling through the undulator resulting in a displacement of the electron trajectory off-axis with a bump as shown in Figure 4.17. Since radiation emitted cannot be added up anymore coherently along the undulator into the forward cone, a reduction of the flux density at high harmonics

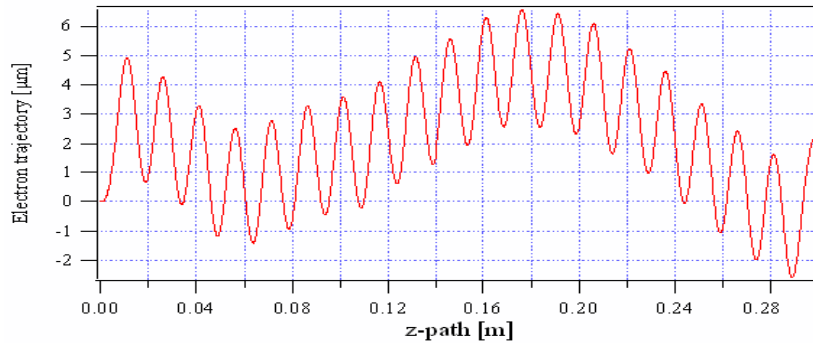


**Figure 4.17** Electron trajectory of 1.2 GeV electron beam when it travels through a real undulator field with a r.m.s field error of 2 %.

occurs. A period length or phase errors introduces less flux density reduction if the phase error is not more than 1 deg. It seems to retain the flux density as the ideal field because this change in period length only shifts wavelength or frequency of the radiation on the spectrum. In reality, the field may include both errors. To simulate the effect of such errors on the angular flux density for harmonics of the radiation both errors are added into the ideal field to generate the real field. The real field is expressed by

$$B_{\text{real} - B} = (B_0 + \Delta B) \sin(k'z) \quad (4.33)$$

In this study if the r.m.s field and phase errors are 3 % and 1 Degree, ratio of real to the ideal of angular flux densities is calculated and shown in Figure 4.18. From this simulation we conclude that the real magnetic field should be within 1 % and phase errors within 1 degree of ideal values to reach an angular flux density as high as 90 % for harmonics up to 5<sup>th</sup> order.

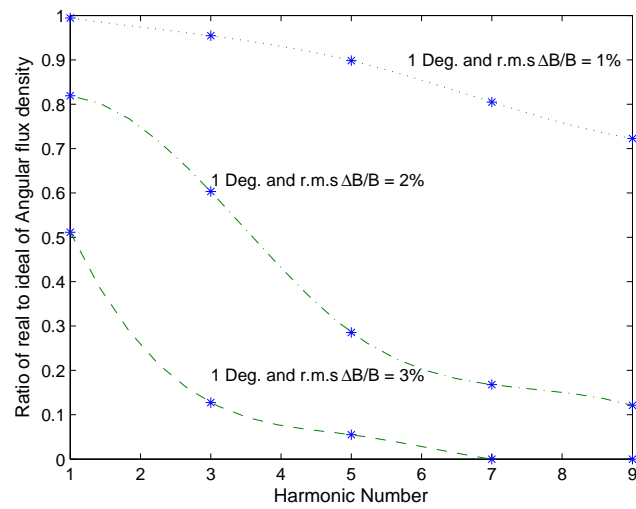


**Figure 4.18** Ratio of real to ideal angular flux densities for each harmonic of radiation emitted into forward cone represented with stars. Real field is generated with adding r.m.s field and phase errors of 1 % and 1 Degree (small dash line), 2 % and 1 Degree (dash-dot line) and of 3 % and 1 Degree (dash-line). Lines are used only to guide the eye.

# CHAPTER V

## REVIEW OF SUPERCONDUCTIVITY

Superconducting undulators were investigated in the 1970 (Farge, 1980) and it was found that the superconducting undulator can provide the hard x-ray especially for low and medium energy of storage rings. Superconducting materials can carry a large current at the high magnetic field as will be discussed in this chapter. We use a superconducting with made from NbTi surrounded by copper to facilitate handling of a quenching magnet. A specific winding method is discussed to achieve a high field in the magnetic gap since the coil winding relates to the achievable short period length. Protection systems are required to protect the magnet against quenching, which is the transition of a section of the superconducting wire to become normal conducting. Both passive and active quench protection systems will be discussed.

### 5.1 Theory of superconductivity

Since a complete disappearance of resistance of mercury below a specific temperature called critical temperature  $T_c$  was covered in 1911 by Heike Kamerlingh-Onnes at the University of Leiden in the Netherlands, this is known as superconducting state. The resistance of the mercury does not gradually decrease with lower temperature but drops dramatically to immeasurable values for temperature below  $4.2\text{ }^\circ K$ . The resistance of the mercury is related to the temperature as shown in Figure 5.1. Not only mercury many metals, but metallic alloys and compounds have this superconducting behavior. Each material has different properties

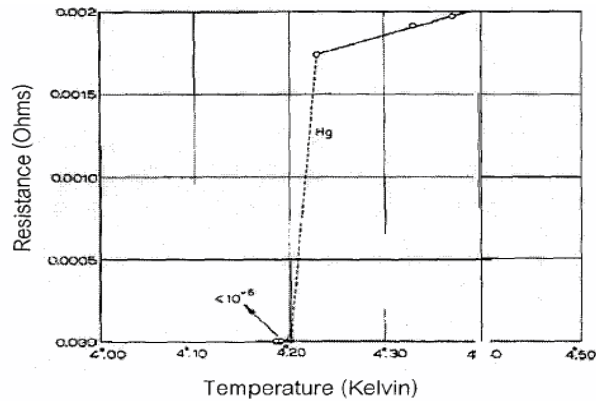


**Figure 5.1** Resistance of superconductivity of the mercury.

such as conductivity, diamagnetism, critical magnetic field, i.e. Superconductivity not only depends on the temperature but also on the surrounding magnetic field and is therefore often characterized by its critical magnetic field. Based on a theory proposed by J. Bardeen (Bardeen et al., 1957), superconductivity is a microscopic effect caused by condensation of pairs of electrons into a new bosonic state called Cooper-pairs; they form together with constructive interaction and well-defined phase (total spin of the copper-pair = 0). Based on BCS theory (Tinkham, 1996) assumption, a Cooper pair, electron in lattice will attract positive charges around it by the Coulomb interaction and the positive charges will, in turn, attract another electron. At low temperatures thermal vibration in the lattices are small enough to allow the forming of stable Cooper-pairs. The electrons pair-up at the temperature lower than a critical temperature ( $T_c$ ). Because the Cooper pairs act somewhat like bosons which condense into the lowest energy level below  $T_c$ , they lose electrical resistance. This means that in a superconductor the flow of electrical current is caused by Cooper pair rather than individual electron. Applying an external magnetic field, the Cooper pairs can set up electrical current on the superconductor surface, because the total spin of the Cooper pairs is always zero and creates by Lenz's law a field equal and opposite to the external field. In-

terior magnetic field produced by these electrical current cancel out the applied magnetic field within the bulk of the superconductor at below the  $T_c$ . Thus the applied field cannot penetrate into the bulk of the superconductor, which means that they become a perfectly diamagnetic. This phenomenon is known as Meissner effect. Base on the diamagnetic the superconductors are separated into two types; type-I superconductor and type-II superconductor. Most type-I superconductor are metal elements and type-II superconductor are most alloys and compounds.

### 5.1.1 Type-I superconductor

If an external magnetic field is applied to a type-I superconductor, then, due to the Meissner effect, an interior magnetic field is building up due to a shielding current on the surface of the superconductor directed against and compensating the external field. We call a superconducting state of this type-I as being in the Meissner phase. Since an exclusion of the interior field from the external field performs completely, the type-I superconductors are perfect diamagnetic with a zero value of the interior magnetic field density ( $B = 0$ ). Superconductivity will be broken down by any temperature which is higher than  $T_c$  but also if the external field is increased over the critical magnetic field strength  $H_c$  and the Meissner phase is changed into a normal conducting state. If the magnetic field is less than  $H_c$  the type-I superconductor is still in the Meissner phase. The critical field of the type-I directly relate to the critical temperature shown in Figure 5.2. The superconductor completely expels an external magnetic field which is lower than the critical magnetic field and critical temperature. Therefore the type-I will be in the superconducting state only at the temperature and the field strength are lower than the  $H_c$  and  $T_c$ , respectively, but if the temperature and field strength are exceed the critical values then they will be transited to a normal state. Table

5.1 shows the critical temperature and the critical field at  $T = 0$  for some type-I superconductor materials. Most of type-I are pure metallic materials.

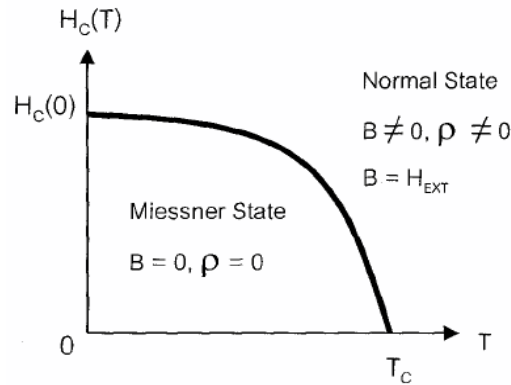


**Figure 5.2** Phase diagram of the type-I superconductor. Electrical resistivity  $\rho$  in superconducting state is zero.

**Table 5.1** Critical field strength and temperature of materials

Elements	$T_c$ [K]	$H_c$ [mT] at $T = 0$
Al	1.19	10
Hg	4.15	40
Nb	9.20	195
Pb	7.20	80
Sn	3.72	30.5
Ti	0.39	17

Based on a modification of classical Maxwell equation by Fritz and Heinz London, a penetration depth was proposed to predict the superconductivity in the type-I. Although the magnetic flux would be excluded from the superconductor, only a small depth in which the shielding current flow, known as penetration depth  $\lambda$ , allows penetration of the magnetic flux. The flux near the surface of the superconductor decays exponentially inward. As the result of  $\lambda$ , the type-I

superconductor performs superconductivity at low critical magnetic field strength  $H_c$  (less than 0.1 T) and temperature  $T_c$ . This limitation make the type-I superconductor impractical use for wire of accelerator magnets which desire a high magnetic field and temperature. Therefore technical developments for superconductors are required to fabricate other superconductor type which is metal alloy, complex oxide ceramic or compound. We know this as type-II superconductors.

### 5.1.2 Type-II superconductor

For a type-II superconductor only a region where a field strength is lower than  $H_{c1}$  at  $T = 0$  shows a similar behavior to the type-I by completely excluding an applied magnetic field. However, the superconductor enter a mixed state shown in Figure 5.3 (Bennemann, 1996) when the field strength is higher than the critical field  $H_{c1}$  and lower than a critical field  $H_{c2}$ . The mixed state which is either superconducting or normal states with an existing of a zero electrical resistance consists of several normal filaments as copper embedded in the type-II superconducting matrix. An external magnetic field applied to the type-II penetrates through the sample in form of quantized lines of magnetic flux or vortices at intermediate field strength region  $H_{c1} < H < H_{c2}$ . The quantized vortices form tubular regions parallel to the external field. These tubes are in the normal conducting state and surrounded by circulating current in superconducting region. The intermediate region sometime is called the Shubnikov phase. But increasing the field strength  $H_{c2}$  is as high as several Tesla, superconductivity transits to the normal conducting state. The type-II superconductor does not only produce shielding current also generates the circulating current around the vortices. To carry the currents throughout its volume, the vortices must somehow distribute non-uniform. In a uniform array of vortices the currents inside the superconductor cancel out on a

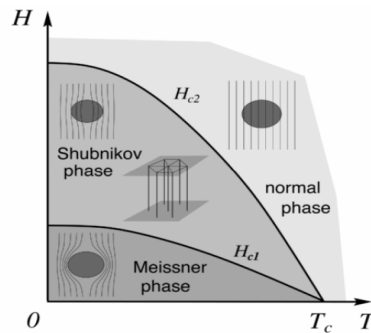


**Figure 5.3** Phase diagram of a type-II superconductor.

macroscopic scale while there are net currents in the inhomogeneity superconductors. It means that there is a macroscopic current or current density. The vortices interact with repulsive force equivalent to Lorentz force  $\vec{J}_c \times \vec{B}$  acting on a macroscopic current density  $\vec{J}_c$ . The Lorentz force is perpendicular to the applied field and current direction resulting in vortex motion through the superconductor. The motion of the vortices with viscosity-limited velocity  $v$  generates an electric field  $\vec{E} = [\vec{B} \times \vec{v}] / c$  which is parallel to the current exhibiting a finite resistivity causing energy dissipation. In order to avoid such process the vortices should be pinned. As long as remaining pinning in the type-II superconductor the vortices cannot move so that there is disappearance of resistance. The pinning vortices can obtain a high current density within bulk material or superconductor resulting in critical magnetic field rise. Many techniques are used in common such as cold working to dislocate cells and heat treatment precipitate finely particles. Typically the type-II perform superconductivity at higher temperature and magnetic field than type-I superconductors. Thus this allows the type-II superconductors to conduct higher currents which are obviously suitable high field magnet applications. Some type-II superconductors are listed in the Table 5.2.

Because of a high critical magnetic field  $H_{c2}$  of many type-II superconductors, both superconductors NbTi and Niobium-tin ( $Nb_3Sn$ ) are widely used in

**Table 5.2** Critical field strength and critical temperature of type-II superconductors.

Elements	$T_c$ [K]	$H_c$ [T] at T=0
NbTi (alloy)	9.6	16.0
$Nb_3Sn$ (compound)	18.0	24.0
$Nb_3Al$	18.7	31.0
$Nb_3Ge$	23.0	35.0
$MgB_2$	$\sim 40$	$\parallel$ to c : 2-5, $\perp$ to c :15-20
$YBa_2Cu_3O_7 - x$	$\sim 93$	$\parallel$ to c :110, $\perp$ to c :240
NbN (metalloid)	16.8	15.3

particle accelerators. Although the  $Nb_3Sn$  can operate at higher temperature and magnetic field strength with critical temperature and upper critical magnetic field of 18 °K and 27 T, respectively, simple fabrication and ductility have been made in the NbTi alloy. Thus the applications of the superconducting NbTi are primary in form of superconducting magnets. Moreover to increase stability and reduce persistent currents small filament diameter of the superconductor is required. Because of brittle of  $Nb_3Sn$ , it quite hard to draw to thin filament like NbTi, however it is formed in a final geometry by heat treatment with high temperature. Therefore most  $Nb_3Sn$  available nowadays, magnitude of filament diameter is larger than that in NbTi.

## 5.2 Niobium titanium

Niobium-titanium (NbTi) is the type-II superconductor consisted of an alloy of niobium and titanium. An upper critical field  $B_{c2}$  is about 13 T and critical temperatures range is limited at 10 °K due to depending on technique to fabricate for

the NbTi wire and chemical composite of the superconductor. Commercial NbTi have appropriate titanium and niobium about 46.5 weight% and 53.5 weight%, respectively because critical temperature and upper critical field  $B_{c2}$  are maximized at that weight of titanium. Since the magnetic field readily penetrated into the type-II superconductor, there is a greater stability and less diamagnetism. If the magnetic field is over the  $B_{c2}$  at localized region in the superconductor, this region will start to conduct local heat due to flux movement known as flux jump which is sudden rearrangement of magnetic field (or discontinuity of magnetization) in the superconductor. The localized heat causes quenching occurring. Then superconductor rapidly transits to the normal state. The ability to eliminate heat away from the localized regions is subdivided the NbTi superconductor into fine filaments embedded in a high conductivity matrix such as copper (Cu) and Al. Although the Al has more thermal conductivity than Cu, it is difficult to fabricate as the matrix of the composite NbTi wire. Thus the flux jump starts, generated heat will be carried away through the copper. In practical NbTi wire, oxygen-free high conductivity (OFHC) copper is mostly used because it consists of very small oxygen and impurities quantities causing by high electrical and thermal conductivities. Most commercial NbTi wires compose of the copper (Cu) in range from 55 to 70 % of wire volume. It means that a Copper (Cu)/Superconducting matrix (Sc) ratio should be more than 1. Furthermore in practical, amount and purity of the copper in the multifilament NbTi wire can be determined by a residual resistivity ratio (RRR) of the superconducting wire. The RRR is a ratio of electrical resistance at 293 °K (at room temperature in the normal state) to the resistance at 10 °K (maximum critical temperature of the NbTi). Because the resistance in the normal state is directly related to characteristic of quench propagation and maximum temperature reached in the NbTi wire during the quenching, the RRR of the superconducting wire is one major parameter to estimate the resistance at high

fields to avoid the quenching in the superconductor. Magnetic instability depends on the filament diameter. The instability causes by a self-field (Nishijima et al., 1997) which is generated by transport currents in superconducting wire. At higher current there are transport current penetrate in the wire and toward to a center not only in an outer shell of the wire as at low current. This result leads to the flux motion. The flux motion generates a heat conducted over the cross-section. In order to reach stability requirement, filament diameter (Wilson, 1983) is

$$d < \sqrt{8} \cdot \sqrt{\frac{k(T_c - T_0)(1 - \lambda)}{\lambda J_c^2 \rho}} \quad (5.1)$$

where  $k$ ,  $T_0$ ,  $\lambda$  and  $\rho$  are thermal conductivity, the cryogenic temperature (4.2 °K), the volumetric proportion of superconductor in a composition; filling factor and resistivity of a matrix which is the copper. If the filament diameter is large, inside of the wire will get hotter than the copper matrix. Finally a whole composition will have a high instability. Although the copper matrix with low resistivity and high thermal conductivity contributes toward the dynamic stability, it creates a coupling between filaments magnetically. As this result the composite behavior acts as a large single filament so that the whole composition will become unstable again to the flux jumping. The coupling and the flux jump instability can be decreased by twisting the composite. Generally superconducting magnets are wound with wire composed of twisted filaments as shown in Figure 5.4. Typically twist pitches should not be higher than eight times of the wire diameter and normally twist pitch is 10 to 20 times of the diameter wire.

For a high superconducting magnet, a high current can be achieved by cable which is stand with multifilament composite of the NbTi filaments in the OFHC matrix with filament size less than 100  $\mu\text{m}$  to achieve the stability. Nowadays, there are different characteristics of the NbTi wire are available from manufacturer. The wire has been chosen followed constrains of design. The constrain are to carry a

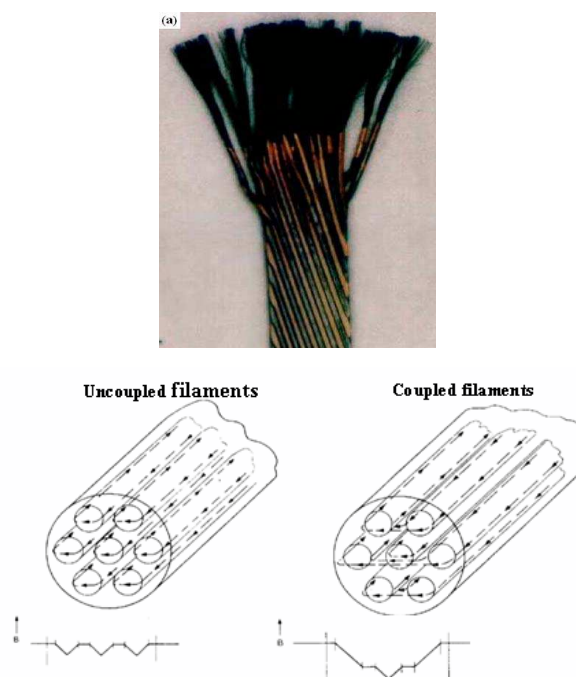


**Figure 5.4** (a) Filaments in an actual cable used for RHIC magnets with a filament size of  $6 \mu\text{m}$ . (b) Coupling and uncoupling in multifilamentary wire.

large current in a high magnetic field with practically zero resistance and to avoid flux jumping. Thus diameter of the composite NbTi wire, the ratio Cu/Sc, filament size and number of the filaments have been chosen to avoid the flux jump causing quenching. In the case of superconducting magnet used in accelerators dealing with multiple coils in complex geometries, the number of filaments in the wire ranges from 50 to 5000 and the diameter of filaments from 5 to  $50 \mu\text{m}$  (Peter, 1999). The multi-filamentary superconducting wire is typically twisted with a pitch varying from 5-30 times the wire diameter (Brazi, 1998).

### 5.2.1 NbTi specification for superconducting undulator

For superconducting undulators with magnetic field less than 10 T, a desirable field below critical field at  $4.2 \text{ }^\circ\text{K}$  can be achieved with the niobium-titanium

NbTi wire composed of several filaments embedded in the OFHC copper matrix. In addition a higher compaction or packing factor which is a ratio of conductor relative to voids is required in order to a greater mechanical stability and efficiency of winding coil. The packing factor range of an interest magnet design is 80-90 % in order to avoid a degradation of magnetic field on beam axis. By choosing a rectangular wire instead of round wire of the NbTi alloy, the packing factor over 90 % can be reached. In the other hand the rectangular wire is simple to control the wire position in grooves. A cross section of the rectangular wire can be sketched shown in Figure 5.5. For the designed superconducting undulator (Jan et al., 2008) to produce the magnetic field of 1.4 T with a period length of 15 mm, the superconductive wire NbTi with a ratio of copper matrix and the NbTi (Cu/NbTi) of 1.35 was selected. Major parameters of the NbTi wire is listed in Table 5.3 with the filament size less than  $60 \mu\text{m}$  to eliminate the flux jumping. A

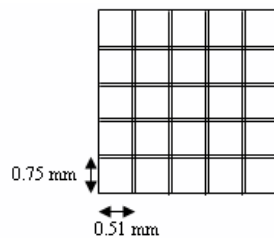


**Figure 5.5** A 2-D schematic dimension of NbTi wire with coated insulation.

critical current  $I_c$  or current density  $J_c$  related to a critical magnetic field of the NbTi superconducting wire was measured by experiment from a manufacturer with serial number of 86039. Measured critical currents of the short sample 86039 are 454, 385 and 318 A at 4, 5 and 6 T, respectively as shown in Figure 5.6. To reach the desirable without quench a current energized thorough the wire should be keep less than the critical current. The critical currents relate to the critical magnetic fields of the NbTi as a quadratic function. From the quadratic polynomial fit, we

**Table 5.3** Specification of NbTi at  $T_c \sim 10^\circ K$  multifilament superconducting wire.

Specification	Value
Composition	NbTi/Copper
Cu/NbTi	1.35
Rectangular wire without insulation	$0.46 \times 0.72 \text{ mm}^2$
Rectangular wire with insulation	$0.51 \times 0.77 \text{ mm}^2$
Filament size	$54 \mu\text{m}$
Number of filaments	54
Critical current	454 A at 4 T and $4.2^\circ K$
RRR	73

obtain the relation by following

$$I_c(B_c) = B_c^2[T] - 78B_c[T] + 750$$

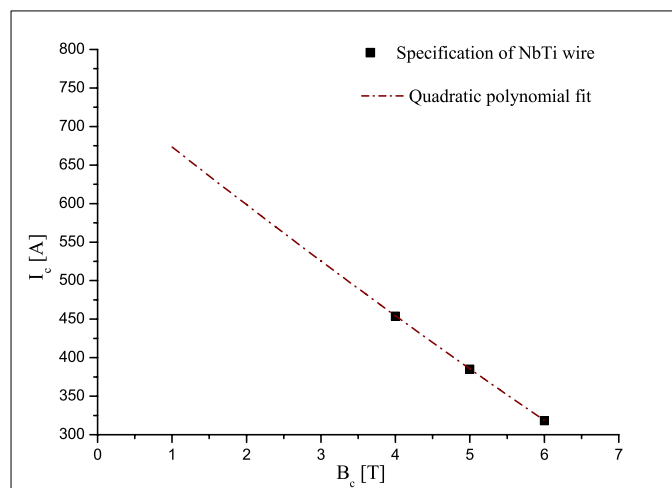


**Figure 5.6** Critical field and critical current relation measured by the manufacturer of a rectangular superconductive wire NbTi with a Cu/Sc ratio of 1.35.

### 5.3 Magnetic field design

The hard x-ray can be reach only with  $K$  close to 2 to 3 for the low energy storage ring, a superconducting undulator with a short period length is required resulting in a small magnetic gap requirement in a few millimeter. To prevent a reduction of maximum magnetic field the magnetic gap should less than the period length. However the magnetic gap cannot be freely tuned due to affects of electron beam lifetime and injection efficiency. A goal of magnet design is to reach a desired magnetic field on the beam axis. Here the desired field is 1.4 T with a period length and magnetic gap of 15 mm and 5.6 mm, respectively. There are various methods of winding superconducting wire on a racetrack-type iron pole to achieve 1.4 T in the gap. In this study, superconducting undulator pole designed at Synchrotron Radiation Research Center, NSRRC is as series of H shape (Hwang et al., 2006) without return yoke shown in Figure 5.7. The undulator pole with 40 pole number is fabricated to be only one piece. A low carbon steel with a content of C < 0.06 % is used to be the pole because of a low coercivity, high permeability at low field and high saturation induction and also to keep a small mechanical tolerance of the fabrication. There are no return yoke because here it is not helpful to increase the field strength in the gap. Array of the superconducting undulator consists

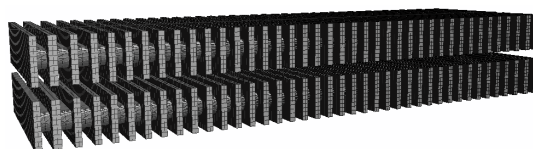


**Figure 5.7** 3-D model of poles of a superconducting undulator with grooves for superconducting wire. Two array of undulator poles are separated with magnetic gap of 5.6 mm.

of 32 main poles and 8 end poles. The main poles were energized with a main

power supply current to produce the magnetic field of 1.4 T while end regions of the undulator can deflect incoming electron and change electron trajectory. Thus it is important to compensate the end fields by adjust some parameters of end poles. Due to the pole shape in Figure 5.7 and wire winding around the pole turn by turn, magnetic flux lines sketched in Figure 7.19 are condensed only in vertical component causing production of vertical magnetic field  $B_y$  while in longitudinal component the magnetic flux are compensated together resulting in a zero longitudinal magnetic field  $B_z$  component disappearance. The main pole

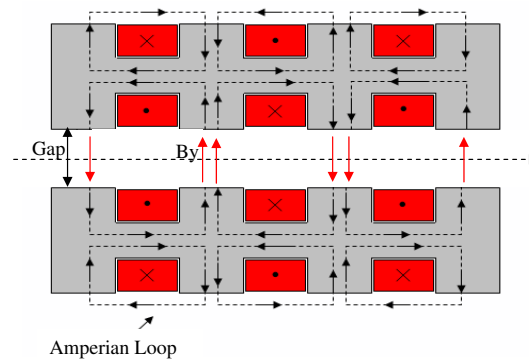


**Figure 5.8** Sketch of magnetic flux line generated only vertical magnetic field in the magnetic gap.

was wound with 55 turns consisting of 5 single turns and 11 layers in horizontal and vertical directions, respectively. The end poles have different number of turns to correct field integrals. The integral of the vertical magnetic flux density along beam axis ( $z$ -axis) within the undulator should be close to zero value. The numbers of turn of winding are 15 with 5 single turns and 3 layers, 42 with 6 single turns and 7 layers and 54 turns with 6 single turns and 9 layers for the first, second and third end poles, respectively. The fourth end poles of the winding has number of turn similar to the main pole. To maintain a winding precision a layer of epoxy insulation between pole and wire is eliminated. Dimensions of the coils in the superconducting undulator have to adjusted to dimension of an actual wire listed

in Table 5.3 and it is also necessary to use a realistic assumption of a working point of the superconducting NbTi wire at 70-80 % of the critical current instead of 100 % to avoid damage on the wire especially at a high excitation current through the coil. Figure 5.9 shows a 2-D model of the superconducting undulator with poles and coil dimensions listed in Table 5.4.

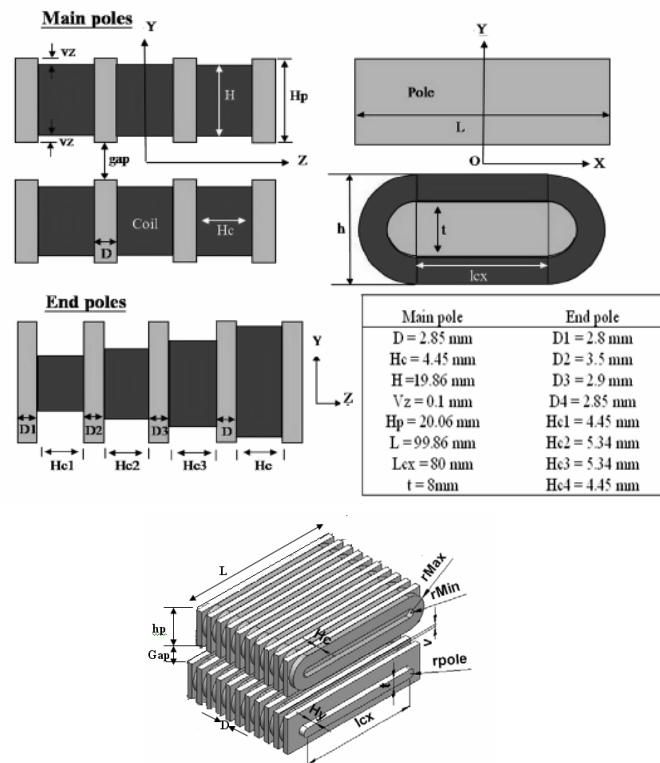


**Figure 5.9** A sketch in 2-D dimension (upper) of undulator poles (lighter part) wound with superconductive NbTi wire (darker part) and 3-D dimension (lower) of the superconducting undulator including coil racetrack.

Based on the dimension of pole and coil, vertical peak fields  $B_0$  on the beam axis in the mid plane of the undulator and maximum fields  $B_s$  in the superconducting coil have been calculated with period length of 15 mm and magnetic gap of 5.6 mm. The superconducting rectangular coil has dimension of  $0.51 \times 0.77$

$mm^2$ . The field in the coil  $B_s$  is defined with

$$B_s(x, y, z) = \sqrt{B_x^2(x, y, z) + B_y^2(x, y, z) + B_z^2(x, y, z)} \quad (5.2)$$

As reference coordinate  $x, y, z$  in Figure 5.9, the field in the coil has been calculated at any  $x, y$  and  $z$  to know an optimum dimension of superconducting wire and find the maximum field strength on the coil in order to keep the superconductivity of the wire at  $4.2 \text{ }^\circ K$ . If the field strength on the coil exceeds the critical field of the superconductive wire then there is a transition from a superconductivity state to a normal state. In the calculation, the positions on the coils are chosen such as at middle, around corners of the coil racetrack and position closed to the pole. Figure 5.10 is the vertical peak field  $B_0$  on the beam axis in the mid plane of the undulator (left axis) and maximum fields  $B_s$  in the superconducting coil (right axis) as a function of current in the coil racetrack. And also Figure 5.10 is shown the critical current  $I_c$  measured for the rectangular NbTi wire as a function of the critical field which is measured by manufacture like in Figure 5.6. A designed peak field of 1.37 T is calculated at a current density (excitation current) of  $1040 \text{ A/mm}^2$  (489 A), which is approximately 78 % of the critical current density of  $1336 \text{ A/mm}^2$  at the maximum field in the coil  $B_s$  of 3.02 T. As the result of the relation between the  $B_0$  and the excitation current through the coil in Figure 5.10 (left axis), we can note that because of magnetization effect of the iron-dominated pole there is a change in a slope at about  $100 \text{ A/mm}^2$  current density and the field strength of 0.40 T. At higher current density there is saturation in the iron pole. At the saturation region the field strength is as a quadratic polynomial function of the current density through the coil described by following

$$B[T] = -5.52 \times 10^{-8} J^2 + 0.00094J + 0.42$$

This relation is used only at  $J > 100 \text{ A/mm}^2$  while at current density less than 100

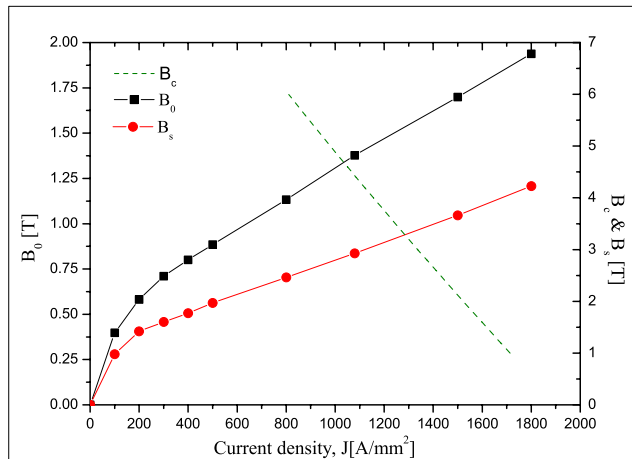


**Figure 5.10** Vertical peak field  $B_0$  (left axis) and maximum field in superconducting coil  $B_s$  (right axis) for a period of 15 mm for gap height of 5.6 mm are plotted as a function of excitation current  $I$ . Critical current  $I_c$  in the coil plotted under applied magnetic field (right axis) for rectangular wire ( $0.51 \times 0.77 \text{ mm}^2$ ).

$\text{A/mm}^2$ , the field strength depends linearly on the current density by following

$$B[T] = 0.00398J[\text{A/mm}^2]$$

Due to the saturation the magnetic field will not be linearly with the excitation current therefore to reach a desirable magnetic field, This B-I characteristic have been used to design the magnet. Magnetic field distributed along the designed undulator is shown in Figure 5.11 with the designed coil parameters for main and end coils in Table 5.4.

Homogeneity of the magnetic field should be sufficiently broad to tolerate errors in spectral phase and alignment of the magnet array and improve photon coherence condition. According to the field calculation, the field uniformity known as a roll-off  $\frac{\Delta B_y}{B_y}$  along the transverse axis (in x axis) is shown in Figure 5.12. The roll-off defined with

$$\frac{\Delta B_y}{B_y} = \frac{B_{\max}(x = 0, y = \text{gap}/2, z = 0) - B(x, y = \text{gap}/2, z = 0)}{B_{\max}(x = 0, y = \text{gap}/2, z = 0)} \quad (5.3)$$

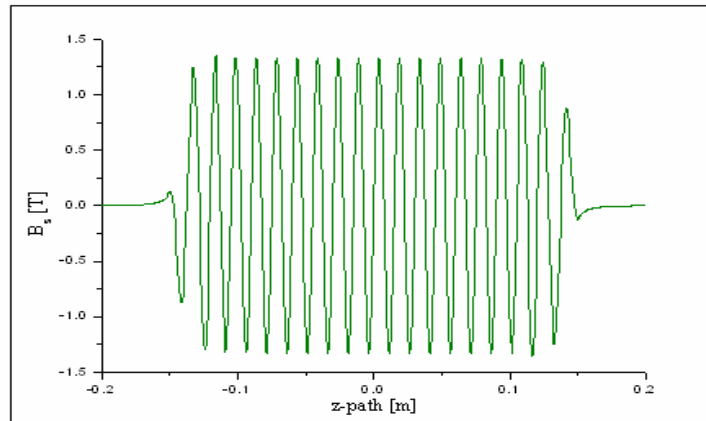


**Figure 5.11** Vertical magnetic field distributed along a beam axis (in z direction) on the axis. A maximum peak field of the main poles is 1.37 T.

The roll-off by  $\frac{\Delta B_y}{B_y}$  of 0.1 % occurs at transverse position of  $\pm 5$  mm. As this result the designed undulator has a symmetrical field distribution of the roll-off on both sides of the magnet along the x-axis. Furthermore the first and second

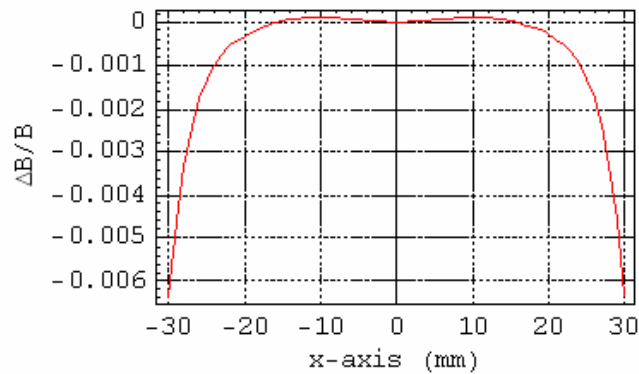


**Figure 5.12** A difference in field strength by  $\Delta B_y/B_y$  of occurring at the transverse position of  $\pm 5$ mm.

field integrals can be calculated by integration of the designed magnetic field distribution. From the designed undulator the first and second field integrals are  $1.86 \times 10^{-8}$  T.m and  $1.06 \times 10^{-8}$  T.m<sup>2</sup>, respectively. Figure 5.13 shown angle and position deviations of electron beam with the beam energy of 1.2 GeV are 4

**Table 5.4** Designed parameters of pole and coil of SCU prototype

Specification	Central	1 <sup>st</sup> end	2 <sup>nd</sup>	3 <sup>rd</sup>	4 <sup>th</sup>
No. of turn/layer	5/11	5/3	6/7	6/9	5/11
Total no. of turns	55	15	42	54	55
Coil dimension [ $mm^2$ ]	25.94	7.07	19.81	25.47	25.94
Pole thickness, D [mm]	2.85	2.80	3.50	2.90	2.85
Pole length, L [mm]	99.86	99.86	99.86	99.86	99.86
Lcx [mm]	80	80	80	80	80
Hp [mm]	20.06	20.06	20.06	20.06	20.06
Hc [mm]	4.45	4.45	5.34	5.34	4.45
Hy [mm]	4.65	4.65	5.54	5.54	4.65
v [mm]	0.1	0.1	0.1	0.1	0.1
t [mm]	8	8	8	8	8
rpole [mm]	4.0	4.0	4.0	4.0	4.0
rMax [mm]	9.93	5.64	7.81	8.87	9.93
rMin [mm]	4.1	4.1	4.1	4.1	4.1
Current density [ $A/mm^2$ ]	1037	1037	1037	1037	1037
Nominal current [A]	489	489	489	489	489

$\times 10^{-3} \mu\text{rad}$  and  $2 \times 10^{-3} \mu\text{m}$ . Since parameters of the end poles are not quite optimized the electron beam is displaced from the beam axis about  $-4 \mu\text{m}$  at an exit of the undulator. However this displacement can be compensated by using a dipole magnetic field produced from steering magnet at beginning and end of the undulator. As this design a prototype of the superconducting undulator is fabricated to measure a magnetic field distribution and investigate a field quality to reach high photon brightness. To reach the high brightness at higher harmonics of the photon radiation field error should be less than 1 % discussed in Chapter

IV. We will discuss more in detail how to correct the errors in the Chapter VII. To measure the field distributed along the undulator a protection system for prevent a damage on the superconducting coil also is required.

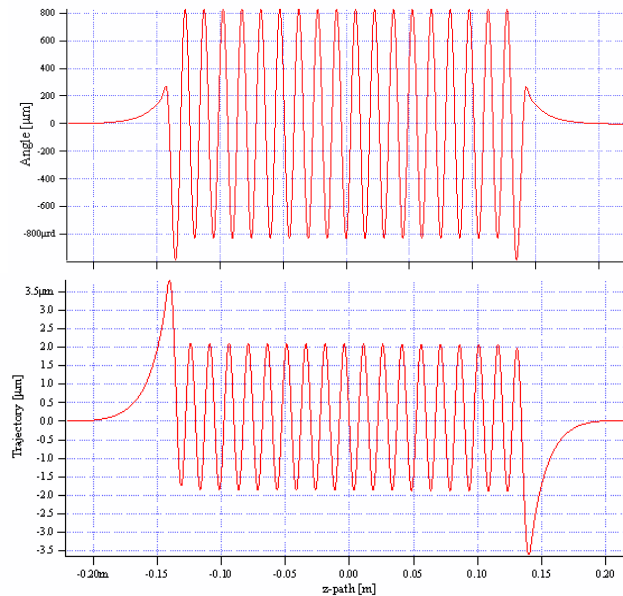


**Figure 5.13** Electron deviations in angle (a) and position (b) passing through the undulator with a period length of 15 mm, a magnetic gap and designed field of 5.6 mm and 1.37 T, respectively. Electron energy is 1.2 GeV.

Finally designed parameters given in Table 5.4 and the working point of 78 % of the critical current density of the superconducting rectangular wire ( $0.51 \times 0.77 \text{ mm}^2$ ) will fulfill design goal with the desired magnetic field of 1.4 T, period length of 15 mm and the gap of 5.6 mm.

## 5.4 Quench protection

If temperature, magnetic field and current density exceed critical values, the superconductor will quench and then it will be converted to a normal state. Sometime the magnet can be quenched spontaneously well below its critical current

due to limitation or deficiencies in design. This quench is known as degradation. Therefore we should know causes of the quench in order to prevent the magnet or at least to have a protection system for the magnet if the quenches occur. During the quench, the stored electromagnetic energy will be converted into heat and dissipated by non-uniformly spread throughout magnet winding. Thus the quench begins at a point and spread through the winding by an Ohmic heating and thermal conductivity process. Finally the superconducting wire will have resistance and then there is less current charged through the wire. As this result it causes a local temperature rise, resulting in melting the conductor. Due to the temperature rise, high voltage will be developed across the normal zone and may cause acting between turns. If the quench process starts, the normal zone will be rapidly grown through the magnet winding so that the stored energy in the magnet is rapidly dissipated resulting in boil off liquid helium in a cold mass (dewar).

To design a protection system, the temperature rise, voltage drop and spreading of the normal zone have been calculated theoretically. Characteristic time of the quench is typically less than a second so it can be described with adiabatical process. An analytic solution is used to solve a problem and approximation of the temperature increasing and voltage. Based on the approximation model of heat balance equation (Wilson, 1983) in one dimension, a solution can be expressed in partial differentiate as

$$\frac{\partial}{\partial x} \left( kA \frac{\partial T}{\partial x} \right) - \gamma C A_c \frac{\partial T}{\partial x} - hP(T - T_0) + GA_c \quad (5.4)$$

With a heat transfer coefficient  $h$ , wetted perimeter  $P$ , temperature reached thermal equilibrium  $T$ , cryogenic temperature  $T_0$  of  $4.2 \text{ }^\circ\text{K}$ , thermal conductivity  $k$ , specific heat  $C$  and generation curve between two regions  $G$ . By using boundary conditions of continuity of heat flow at interface between two regions and some assumptions the propagation velocity can be calculated. A goal of solving the quench

is self-protecting of the undulator by eliminating normal zone quickly. Therefore a maximum temperature rise and the internal voltage are within limits as estimated in a superconducting wiggler magnet (Mikkonen, 1996; Mikkonen, 1999). Although the quench can help the undulator to settle and to relieve induced structural stress, it will produce high temperature or excessive voltage caused on the superconducting wire. Only a small amount of energy require to start the quench therefore to reach the designed magnetic field several quenches are required, and the quenches occur at progressively higher field. The protection is needed to protect the magnet from damage caused excessive temperature and voltage resulted from the quenching. A good protection circuit is needed to dissipate the most of the stored energy in order to avoid the boil-off the liquid helium. Moreover the circuit should be designed to investigate voltages producing outside the magnet. There are several techniques to be made (Smith, 1963). A reliable passive technique shown in Figure 5.14 is used for high field magnets. To prevent the stored energy from being dissipated in the quench current will be flow bypass through shunt element (resistor). The resistors about  $0.5\text{-}2\ \Omega$  are connected to all the undulator coils in the cryostat. Diodes also are used to form a hardware quench protection circuit.

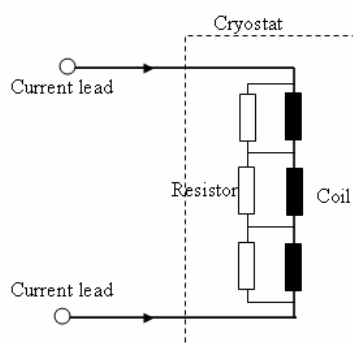


**Figure 5.14** A diagram of a passive quench protection circuit.

The passive technique is usually cheap, simple and reliable. It can reduce

the internal voltage and they produce no external voltage. However this technique must be set the energy dissipation when the magnet winding is charged, especially if short times are required and the fact that all the stored energy will be dumped in the cryostat when there are quenches. These are main source to boil-off the liquid helium.

Other technique known as an active protection needs reliable operation of detectors and switches. The switch must be opened promptly when the quench starts; it means that a sensitive detector is required. To make the detector which will respond to very small resistance present at the start of the quench while ignoring voltage spikes balance circuit. A potentiometer is used to adjust until the detector does not respond to  $dI/dT$  in the undulator. Based on assumption normal zone will create an out-of balance voltage which is detected. The switch is designed to open on full load. But if is a mechanical switch, it has to be rated as a d.c circuit breaker with suitable provision for extinguishing the arc. The quench is detected by the detectors then the resistors are switched on in series with the coil shown in Figure 5.15. If the resistor  $R_e$  has resistance higher than an internal quench resistance, the current will decay exponentially with a constant time  $\tau = L/R_e$

$$I = I_0 e^{-(t/\tau)}$$

A safe maximum for voltage over  $R_e$ ;  $V_e$  is usually kept a few kV which is rea-

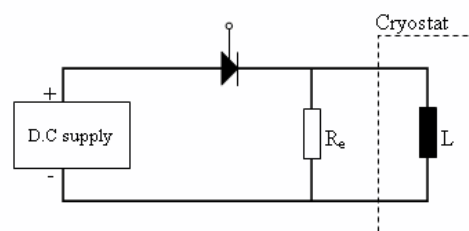


**Figure 5.15** A diagram of an active quench protection circuit.

sonable limits to avoid insulation problems. The normal zone is not quite easy to detect due to existing of a large inductive voltage. Thus the voltage detector should respond to very small the resistance. The active technique by using the dump resistor has some advantages of extracting the stored energy from the cryogenic enclosure. Therefore a high pressure resulting from explosive boiling off the liquid helium can be avoided.

A prototype of the superconducting undulator with designed parameters following the listed in Table 5.4 with current charged through the NbTi superconducting wire only about 82 % of the critical current density of  $1270 \text{ A/mm}^2$  was fabricated at NSRRC in order to measure magnetic field in a vertical test dewar composed of the passive protection system to prevent the quenches when the undulator is trained to reach the magnetic field of 1.4 T.

# CHAPTER VI

## MAGNETIC FIELD MEASUREMENT

A superconducting test undulator (SCU) built at NSRRC serves in this study as a reference for a realistic superconducting undulator which we will use to test the effectiveness of correction methods necessary to produce high intensity radiation at high harmonics. Before we apply corrections we must measure the actual magnet. The magnetic field of the SCU with a period length of 15 mm has been measured in a vertical cold bore to characterize the magnet field profile along the beam path. Field measurements must be integrated, like the first and second field integrals to define necessary corrections of the electron beam perturbation in the storage ring. In this chapter, the setup used for field measurements in a vertical test dewar will be described and the analysis of the measured fields will be discussed.

### 6.1 Introduction

There are a variety of techniques available to measure the magnetic field of undulator magnets in a storage ring (CERN School, 1992-2005). To determine specific undulator field characteristics, techniques like Hall probe measurements, straight wire methods and flipping coil arrangements can be applied at room temperature. Each technique offers advantages and we have to choose a suitable technique depending on the requirement of the measurement; point by point field distribution, integrated magnetic fields, speed, accuracy and geometric constrains etc pose experimental challenges. In case of the SCU with a period of 15 mm,

a magnetic field strength of 1.4 T and a magnetic gap of 5.6 mm the fields can be measured point by point with a Hall probe along the SCU magnet axis at a cryogenic temperature of 4.2 °K. The probe has been designed and constructed to work in the small magnetic gap of the SCU with high precision control of its location.

## 6.2 Hall probe

The Hall Effect was discovered by Edwin F. Hall in 1879. When a conductor with current flowing along one direction is placed in a magnetic field  $B$  the Lorentz force pushes the moving electrons to one side of the conductor. This causes a depletion of electrons on one side and a surplus of electron on the other resulting in a transverse electric field  $E_H$  known as the Hall effect. The electric field  $E_H$  is perpendicular to the directions of both the external magnetic field and the direction of the current flow. This buildup of charges on both sides of the conductor produces a measurable voltage called Hall voltage  $V_H$  and is defined with the electric field as

$$V_H = E_H w \quad (6.1)$$

where  $w$  is the conductor width as shown in Figure 6.1. The Hall field  $E_H$  is expressed in terms of the magnetic field while the electric and magnetic forces are related by

$$E_H = vB \quad (6.2)$$

The electrons in the Hall plate travel with a drift velocity  $v = I/neA$ , where  $I$  is the input current for the Hall plate,  $n$  is the electron density (number of electron per unit volume =  $8.5 \times 10^{28}$  electrons/ $m^3$ ) and the cross-section of the Hall plate  $A = wd$  (see Figure 6.1). The Hall voltage can now be expressed in terms of the

magnetic field by

$$V_H = \left( \frac{I}{ned} \right) B \quad (6.3)$$

and be used for calibration of the Hall sensor. The Hall voltage is proportional to the magnetic field and the coefficient of proportionality depends on the drift velocity and density of the conduction electrons in the Hall plate. The coefficient is negative for electrons but positive for holes. Because of the low electron density in semiconductors drift velocity is high and the Hall voltage is high. Therefore, semiconductors such as InSb and GaAs are good choices to be used for the material of the probe. However, the electron density and some geometric factors are not known to the desired precision and thus the proportionality factors have to be calibrated in a known uniform magnetic field.

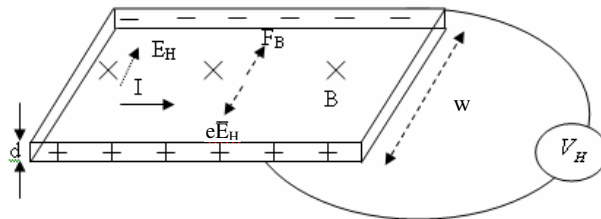


**Figure 6.1** A flowing current through the Hall probe generates the Hall voltage  $V_H$ .

During the measurement of the SCU, a transverse cryogenic Hall sensor has been used from AREPOC Ltd, Model HHP-MP as is shown in Figure 6.2, which is designed for measurements of perpendicular magnetic fields. The sensor is calibrated in a special calibration field generated by precision placed copper or superconducting coils (depending on the range of the calibration) in the arrangement of Helmholtz coils or by Nuclear Magnetic Resonance (NMR). For the calibration system a precise stable current source together with the coil, producing a highly uniform magnetic dipole field at a requested temperature as well as

a digital precision voltmeter for the Hall probe are required. The calibration coil (electromagnet) cannot contain any iron or ferromagnetic parts. Alike, the coil must be wound from a copper conductor (or superconductor) wire (not from a wide tape) to avoid magnetic field hysteresis. Finally, the coil is calibrated precisely to define its current dependence  $\text{dB}/\text{dI}$ . Then we can make the calibration of the Hall probe. Due to interaction between the nuclear angular momentum and

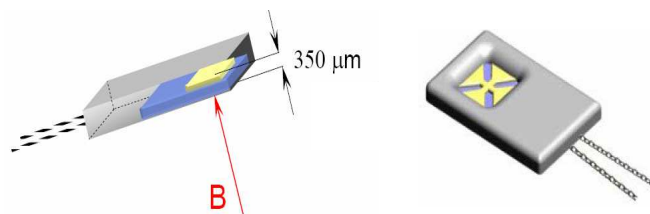


**Figure 6.2** Packaged transverse Hall sensor Model HHP-MP from AREPOC Ltd. with  $350 \mu\text{m}$  distance between active area and surface. The active area center is marked accurately to  $\pm 0.05 \mu\text{m}$  as per AREPOC information.

applied magnetic field, magnetic energy sublevels in a nucleus with non zero angular momentum will be split. A radio frequency (rf) magnetic field with a proper frequency is applied to induce a transitions between sublevels known as nuclear magnetic resonance. The transitions of a sample (NMR probe) can be observed by detecting the rf signal at the resonance frequency associated with the transition. Information of the sample is obtained when resonance occurs and the rf frequency is proportional to the applied magnetic field. This Lamor frequency is

$$\nu_0 = \frac{1}{2\pi} g\mu_N B_0 \quad (6.4)$$

where  $B_0$  is the static field applied to the sample,  $\mu_N$  is the nuclear magnetron and  $g$  is the g-factor for the nucleus (Preston, 1991). From this system the resonant frequency  $\nu_0$  corresponding to the magnetic field will be measured. The NMR sys-

tem typically composes of rf generator, amplifier, oscilloscope, multimeter, counter and readout circuit as shown in Figure 6.3. Signal produced in a generator is split into two signals; one goes to oscilloscope and the other goes to NMR probe sweep field coil. From a formula 6.4 the NMR frequency  $\nu_0$  can be calculated and set it

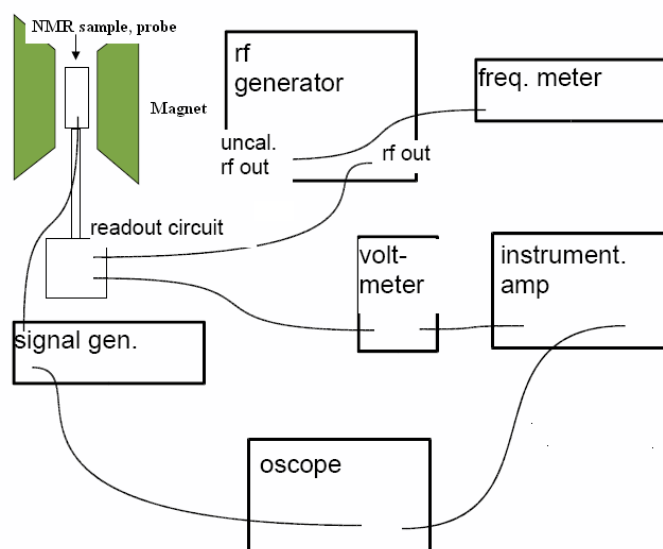


**Figure 6.3** A schematic of the NMR set up.

to search a peak in oscilloscope. At the given  $\nu_0$  the NMR peak will stay in phase with sweep field signal. The magnetic field is read with NMR Tesla-meter. The sweep field allows for the NMR signal to be seen in a narrow region around the central frequency as well as shows the transition between out of and into resonance.

The HHP-MP Hall sensor has an active area of  $0.1 \times 0.1 \text{ mm}^2$  and overall dimensions of  $7 \times 5 \times 1 \text{ mm}^3$  with characteristic data as shown in Table 6.1. The active area is kept small to allow high spatial resolution of the magnetic field measurement. This probe is covered by special synthetic resin and has a very high linearity from room to cryogenic temperatures within a magnetic field range of 0-5 T. The Hall sensor has to be calibrated at  $77 \text{ }^\circ\text{K}$  or room temperature although the field is measured at  $4.2 \text{ }^\circ\text{K}$  because of possible damage to the probe at cryogenic

**Table 6.1** Specification of the HHP-MP Hall sensor

Parameter	Unit	300 °K	77 °K	4.2 °K
Nominal control current, $I_n$	mA	20	20	20
Maximum control current	mA	20	50	50
Sensitivity at $I_n$	mV/T	139.7	-	-
Offset voltage at $I_n$	$\mu$ V	<-50	<150	-
Input resistance	$\Omega$	34	22.6	-
Output resistance	$\Omega$	34	21	-
Linearity error up to 1 T	%	<0.4	-	-
Temp. coefficient of sensitivity	$K^{-1}$	$2 \times 10^{-4}$	$5 \times 10^{-5}$	$5 \times 10^{-5}$

temperatures. The sensitivity of this sensor between 77 °K( $S_{77}$ ) and 4.2 °K( $S_4$ ) can be calculated by using a relation following with

$$S_{77}[mV/T] = S_{I_n} + TC_{300} \times S_{I_n} \times (\Delta T)$$

$$S_4[mV/T] = S_{77} + TC_4 \times S_{77} \times (\Delta T)$$

where  $S_{I_n}$  is the sensitivity at 300 °K given in the parameter sheet of the probe, the temperature coefficient at room temperature  $TC_{300}$  and 4.2 °K  $TC_4$  are  $2.1 \times 10^{-4}K^{-1}$  and  $5.1 \times 10^{-5}K^{-1}$ , respectively,  $\Delta T$  is the temperature difference. By using the above formulas the sensitivity at 77 °K can be approximately calculate to be  $S_{77} = 145.9$  mV/T and the same calculation procedure can be used at 4.2 °K  $S_4 = 146.5$  mV/T. We can see that the sensitivity between 77 and 4.2 °K increases only very little in comparison to the change of the sensitivity in the temperature range 300 to 77 °K. Finally, this calculated sensitivity cannot be used instead of calibration. The temperature coefficient may be slightly different for each piece of semiconductor wafer used for the Hall probe production, but should be very

close to the calculated ones. For the calculation of the HHP-MP Hall probe, the calibration magnet must produce a uniform field in the range of up to 3 T with a field uniformity of better than 1 T/m. Furthermore, a Metrolab Model PT2025 precision NMR-meter with five NMR probes and a multiplexer are used. The NMR-meter and the Hall sensor voltage are connected via an interface bus to a computer to record the voltage and the magnetic field. Usually to calibrate the Hall probe with the NMR probes a set up shown in Figure 6.4 consists of the NMR probes, Hall probes, Hall sensor current source meter model HP3458A, Hall voltage output meter, NMR read circuit and control recorder. By driving the NMR and Hall probes along a small length of the magnet in small steps both absolute magnetic field and Hall voltage associated with the field can be measured. The sensor is placed symmetrically in the magnet gap and close to the NMR probes in order to reduce errors caused by field inhomogeneities. Care must be taken to ensure that both, Hall and NMR probes are aligned normal to the field.

During the calibration, the Hall sensor is energized with a constant current of 10 mA from a Lakeshore-120 current source, Five different NMR probes with overlapping ranges from 0.047 T to 0.124 T, 0.0946 T to 0.221 T, 0.192 T to 0.508 T, 0.479 T to 1.02 T and 0.998 T to 1.59 T are used with the calibration system to measure the magnetic field strength in the magnet against the Hall voltage of the Hall sensor. Two electron paramagnetic resonance EPR probes are used at low fields in the range of 0.000964 T to 0.00124 T and 0.00304 to -0.00296 T. As the result of the calibration the Hall voltage is directly related to the corresponding magnetic field as shown in Figure 6.5. Each region of calibration data has been fitted by a polynomial function by minimizing the sum of square error (SSE). The SSE value or variance determines the quality of the fit. To represent the measured data points well, a polynomial fit of the fifth order is used in each calibration region. The fit equation covers the range from -1.59 T to 1.59 T expressed by the

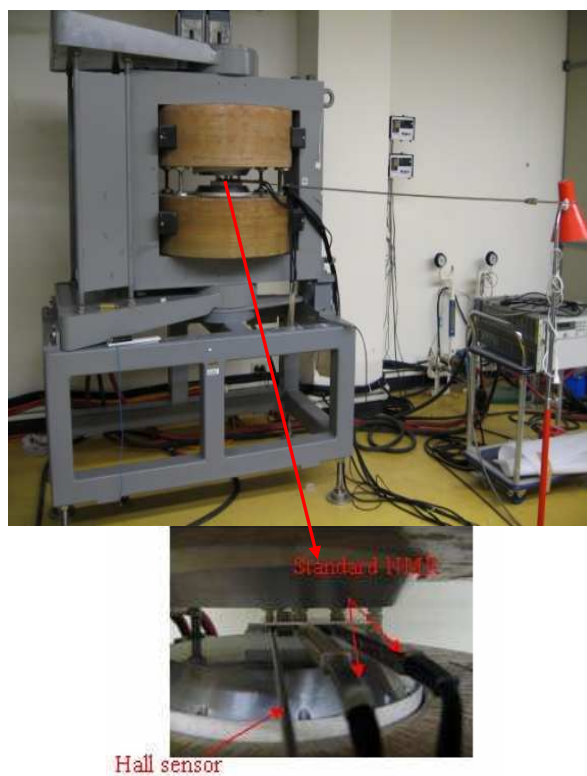


**Figure 6.4** Calibration system of the Hall sensor at NSRRC by using the standard NMR probes at room temperature.

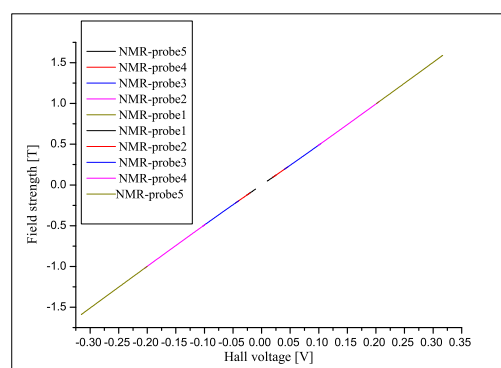


**Figure 6.5** Measured field strengths monitored with five NMR probes for different field levels as a function of the Hall voltage recorded by the Hall voltage output at a current through the Hall sensor of 10 mA.

Equation

$$B[T] = \sum_{i=0}^n p_i V_H^{n+1-i} \quad (6.5)$$

where  $p_i$  are the fit-coefficients and  $n$  is the degree of the polynomial (here  $n = 5$ ). The fit-coefficients separated into five sections are compiled in Figure 6.6. The most useful results for evaluating the fit are the residuals and SSE and we can use this information to select the order of the polynomial fit.

Section	Range	points	Coefficient of the fit
1	V=0.20009 to 0.3167 V B=1.0006 to 1.5902 T	199	$p_1=461.6, p_2=-587.8, p_3=299.8$ $p_4=-76.3, p_5=14.78, p_6=-0.51$
2	V=0.2007 to 0.0149V B=0.9982 to 0.0719 T	387	$p_1=61.15, p_2=-26.72, p_3=0.96$ $p_4=-1.44, p_5=4.76, p_6=3.91$
3	V=0.0146 to -0.0145 V B=0.0701 to -0.0698 T	39	$p_1=102740.6, p_2=-4321.1, p_3=-13.2$ $p_4=-1.5, p_5=4.8, p_6=1.2$
4	V=-0.0149 to -0.2001V B=-0.0717 to -0.9984 T	389	$p_1=57.2, p_2=26.3, p_3=1.4$ $p_4=-1.37, p_5=4.8, p_6=-1.2$
5	V=-0.2005 to -0.3154 B=-1.0007 to -1.5901 T	194	$p_1=858.4, p_2=1092.5, p_3=555.7$ $p_4=140.9, p_5=22.9, p_6=0.9$

**Figure 6.6** The polynomial fit-coefficients of the Hall sensor calibration

Comparison of the residuals between a first order (linear) and fifth order polynomial fit is shown in Figure 6.7. If the order of the fit is increased then there is little improvement on the SSE values however the higher order (7<sup>th</sup> up to 9<sup>th</sup>) may introduce wiggles in the calibrated data even though there is a small SSE value for a higher order polynomial fit. Therefore, the fit is used only up to the fifth order with the  $SSE = 5.2 \times 10^{-8}$  while the linear fit gives  $SSE = 1.395 \times 10^{-5}$ . From the calibration curve, the sensitivity at the control current of 10 mA of the Hall sensor can be calculated by the reciprocal for the coefficient of the first order (linear term), denoted  $1/p_5$  and called the sensitivity which is about 67.6 mV/T at room temperature. For calculations, the sensitivity is proportional to the control current. It means that if the Hall sensor has the sensitivity 139.7 mV/T at 20 mA, then the sensitivity will be only 69.85 mV/T of 10 mA control current. The difference in sensitivity at nominal current of 10 mA between calculation and calibration is not large and we use the calibrated data to convert Hall voltage to magnetic field

strength for this Hall probe. The small difference may be caused by the setting of the Hall sensor and NMR probes not being perfectly aligned on the mid plane. From the calibration data, the excitation curve relating the excitation current in

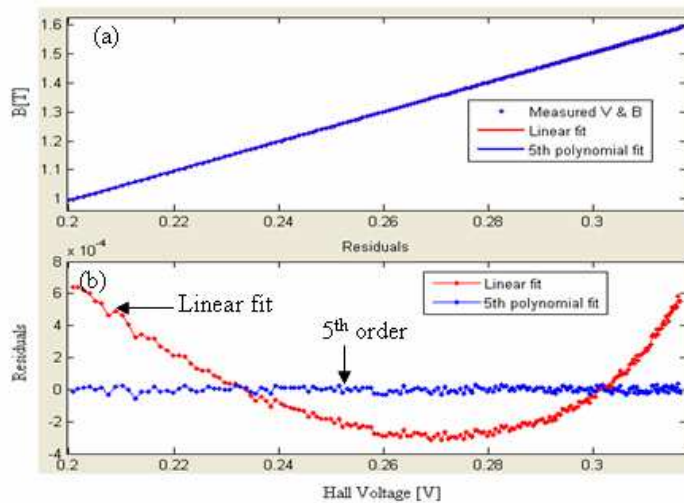


**Figure 6.7** Comparison of Hall voltage from the Hall sensor in the presence of a magnetic field (a). Differences between measurements and fits are shown as residuals (b), where the control current fed through the Hall sensor is 10 mA at room temperature (300 °K).

the test magnet to its magnetic flux density ( $B$ ) is determined. For instance, during magnetic training with varying excitation currents through the superconducting coil of the SCU, the Hall sensor will generate an output voltage corresponding to the field as given by the calibration data, thus the B-I characteristic will be obtained. For example, if the excitation current through the coil is 200 A and the Hall probe voltage is measured as 0.2 Volt by the volt meter then the magnetic field density is determined from the fit equation of the calibration curve ( $B - V_H$ ). The Hall sensor with a holder fabricated from non-magnetic stainless steel (SS316L) is positioned in the transverse direction by a probe guide (x-axis) and the magnet poles (y-axis) while guiding in the longitudinal axis is done with a

position controlled z-stage (z-axis). The probe guide length is about 580 mm and mounted to the Hall sensor as shown Figure 6.8. The Hall sensor is positioned along the x -axis by the probe guide including the SCU magnet array and along the y-axis by using the probe guiding.

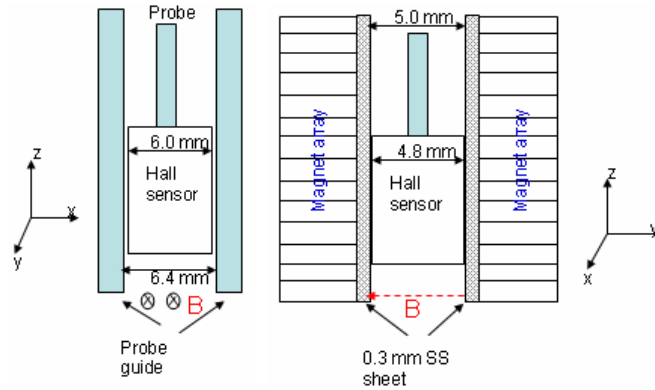


**Figure 6.8** Top view (left) and side view (right) of a Hall sensor holder (schematic) in housing made by SS316L steel and positioned by probe guide.

### 6.3 Beam duct

A 0.3 mm thick beam duct fabricated from the stainless steel 316L at NSRRC is used to support the SCU array and also to separate the Liquid Helium (LHe) from the vacuum of the storage ring. The beam duct has an aperture of 5 mm and is coated with a high purity copper on the inner surface to reduce heat load from image currents as shown in Figure 6.8 (a). Furthermore, the beam duct also includes a taper providing a smooth transition between the small aperture in the magnet array at 4.2 °K and the large regular beam pipe at 300 °K. The beam duct is glued onto the dummy array of the SCU poles by epoxy as shown in Figure 6.9 (b). Figure 6.10 (a), (b) shows the assembly of the beam duct and a schematic model of the cross-section view of the beam duct, respectively. At both sides of the magnet array the probe guide are fixed in the beam duct in order to precisely

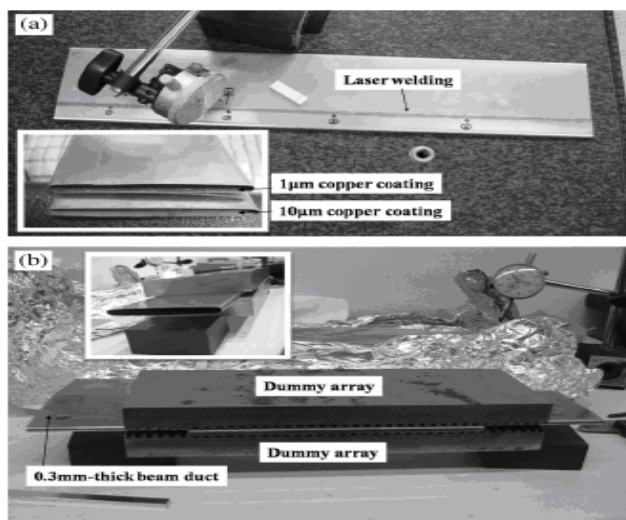


**Figure 6.9** (a) Beam duct has a cross section like a racetrack shape with an inner aperture of 5 mm and is coated with a copper layer on the inner surface. (b) the beam duct is glued with the magnet array.

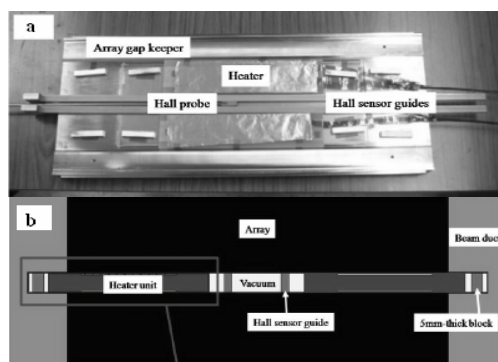


**Figure 6.10** An assembly of the magnet unit (a) and sketch of cross-sectional view of a beam duct (b).

guide the Hall probe through the SCU magnet.

## 6.4 Measurement setup

To train the SCU assembly and measure the magnetic field performance, the magnet has to be immersed in liquid Helium in a vertical test dewar with

special characteristic design to prevent a boil off of the Liquid Helium or a quench.

### 6.4.1 Vertical test Dewar

To train the superconducting coil up to high current generating field strength of 1.4 T the magnet unit has to be assembled in a vertical test dewar. The dewar consists of an inner liquid nitrogen reservoir within an outer liquid helium reservoir. The outer vessel is thermally shielded from the room temperature environment by an insulation layer in vacuum and the liquid nitrogen reservoir as shown in Figure 6.11. The dewar consists of a current lead, several valves to input helium as well as relief valves, several baffles placed to reduce radiative heat transfer to the magnet portion and to reduce natural convection in the vapor space and data acquisition system. In reality, the current lead is separated into two parts.

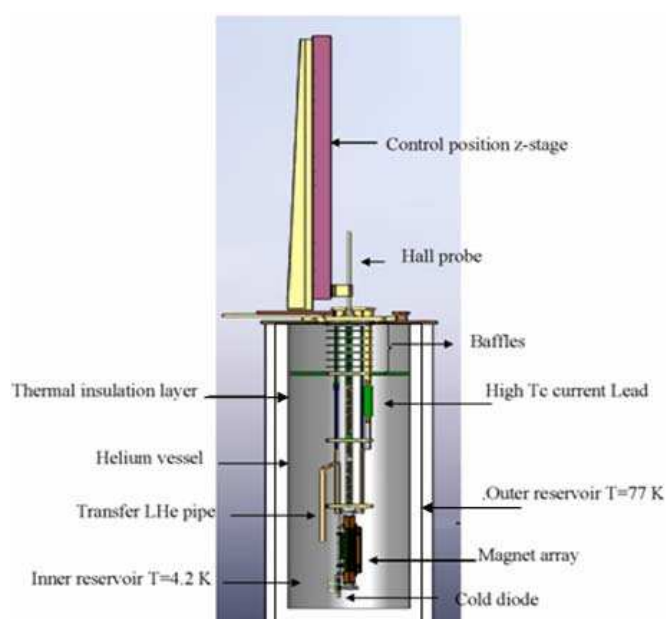


**Figure 6.11** Main components of the dewar lid in a vertical test dewar for training and field measurement of the SCU magnet with surrounding temperature of 300 °K.

A high temperature current lead HTS is a ceramic composition which is less thermally conductive than metallic material. It is used to feed a high current through the SCU coils in the LHe vessel. The last part is normal conducting copper rods. The purpose of the copper tubes are to provide a path for the helium vapor occurring from quenches or boiling off of the LHe to escape through the top of the dewar lid. The  $Nb_3Sn$  can be operated with high current at higher temperature of  $10\text{ }^\circ K$  and therefore it can be placed outside the LHe. It is connected to the HTS current lead and bare NbTi wire of the SCU coil. At connection between NbTi and  $Nb_3Sn$  has to be in the LHe to protect against a quench during test and measurement. In practical 1.37 m height the dewar consists of three baffles, four temperature sensors and a level sensor to monitor the liquid helium level. All main components of the dewar used to measure the magnetic field is shown in Figure 6.12.

The SCU is pre-cooled from the room temperature of 300 to  $77\text{ }^\circ K$  by using liquid nitrogen. After reaching that temperature cold helium gas is feed into the dewar first to increase the pressure for easily transfer the liquid He into the dewar until the temperature is down to  $4.2\text{ }^\circ K$ . Then the LHe is pored into the test dewar immersing the coils in liquid helium. The LHe should be filled in the dewar until most of the SCU is floated in the liquid.

#### 6.4.2 Magnetic training

When the cryogenic temperature of  $4.2\text{ }^\circ K$  is reached in the dewar and the level of is 60 cm (from the bottom of the dewar) to cover the whole magnet coils energized step by step to eventually reach the desirable magnetic field strength of 1.4 T. To achieve that field the coil is energized by a high current introducing a high Lorentz force. If that Lorentz force becomes greater than the restraining

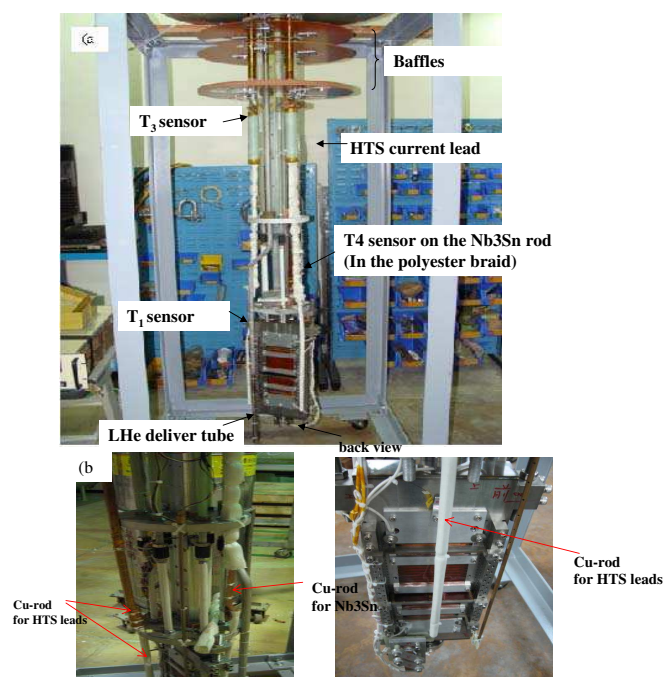


**Figure 6.12** The SCU15 array in the beam duct assembled mainly of components to be used for the training and the field measurement (a) and copper rod using along the magnet array in order to get rid off the heat source for LHe (b).

force of the packed coil then the wire can move. The movement of the wire results in frictional heating sufficient to destroy the superconducting wire and goes to the normal conductor which is called quenching. Quenching can pack the coil better together or shift the coil to a solid location. Thus when the coil is again at a temperature of  $4.2 \text{ }^\circ\text{K}$  can be reenergized with a higher current. Through this process it will train successively to higher magnetic fields before quenching. Increasing the current this way step by step is called magnet training leading to the desirable field. In the case of the SCU, the coils are charged up to a maximum with energizing current of 335 A, standby with small steps to the higher current until quenching. In order to stabilize the magnet coils, several quenches are required to get high current. The training is done in several cycles to obtain the maximum field with a well perform of the wire location. After 32 cycles of training the SCU

magnet coated with Teflon can be continuously energized to the magnetic field strength of 1.42 T at 527 A as shown in Figure 6.13.

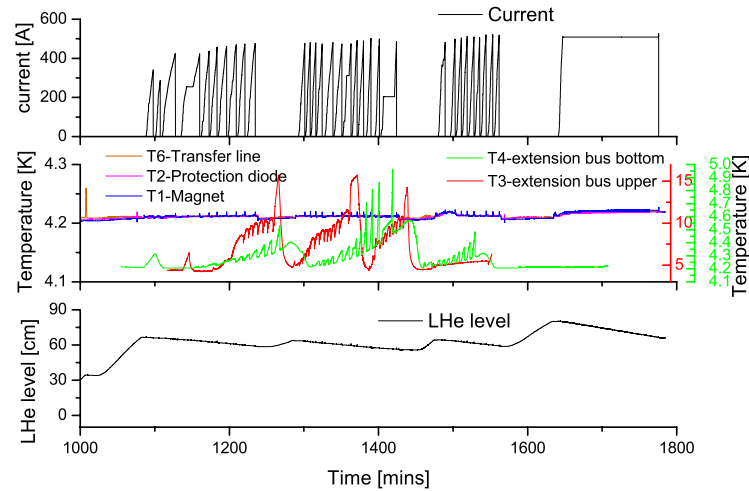


**Figure 6.13** The Training process of the SCU magnet in 32 cycles to achieve the maximum field strength of 1.42 T with a limited quench voltage of 0.3 V at 4.2 °K temperature for T6, T2 and T1. The temperature at the bottom and upper extension bus are as high as 5 and 15 °K , respectively.

During training temperatures have to be monitored to keep the magnet at cryogenic temperatures by using the temperature sensors T1, T2, T3, T4 and T6. The sensor T1 is at the magnet array, T2 is used to measure the temperature at the diode placed on the bottom of the magnet to eliminate incorrect current directions through the SCU coil. If there is current in the wrong direction the current will be stored through the diode. Besides monitoring the temperature at the magnet we also record the temperatures at the HTS current lead with T3 and T4 sensors. Because the  $Nb_3Sn$  carries sufficient current at high temperature (at least 10 °K) or above the liquid helium level to produce that field strength it is used to deliver the current powering at HTS lead to the NbTi wire. Therefore, during training and measurement the temperature of T4 can go up higher than 4.2 °K. From the training process the relation between the magnetic field density B

and excitation current  $I$  energized through the SCU coil corresponding to the Hall voltage of the Hall sensor can be determined. For example, the excitation current is 200 A corresponding to a Hall voltage of 0.1 V. According to previous calibration of Hall voltage and field density  $B$  can be related and the B-I curve is obtained by the training as shown in Figure 6.14. With the B-I relation we can determine the magnetic field strength at any excitation current through the superconducting coil.

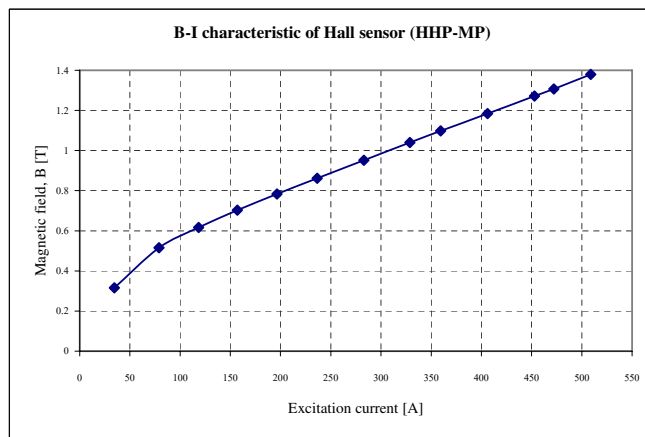


**Figure 6.14** The B-I characteristic of the Hall sensor (HHP-MP type).

## 6.5 Magnetic field measurement

The hall probe can read the field strengths with a resolution of 0.1 mm over the entire undulator. The total scanning distance for the magnet is 450 mm starting outside the undulator at zero field. A vertical magnetic field  $B_y(z)$  of the undulator with a period length of 15 mm and 20 periods is scanned along the z-axis at an excitation current of 510 A at cryogenic temperatures. The excitation current corresponds to a field strength of 1.387 T calibrated with the NMR and electron paramagnetic resonance (EPR). The field distribution is shown in Figure 6.15 and minimum, average and maximum field amplitudes are 1.352 T, 1.387 T

and 1.428 T, respectively. The measured field distribution deviates by  $\Delta B_i$  from

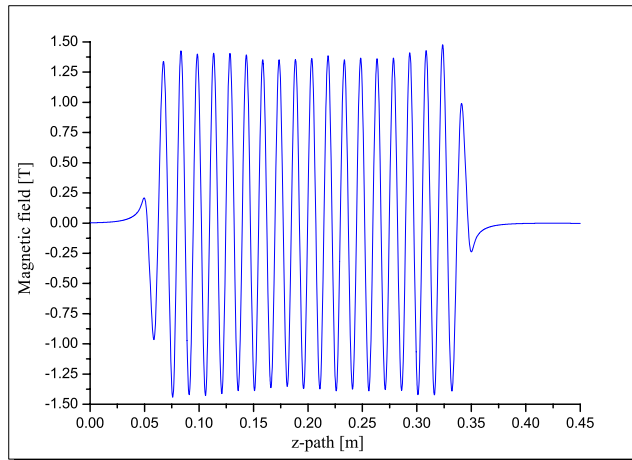


**Figure 6.15** Measured field of the SCU15 along the beam axis using a Hall probe at a temperature of 4.2 °K.

the designed value of  $B_0$  defined as

$$\Delta B_i = B_{i-meas} - B_0 \quad (6.6)$$

Similar deviations apply to the period length

$$\Delta \lambda_{p,i} = \lambda_{p,i-meas} - \lambda_{p0} \quad (6.7)$$

where  $B_{i-meas}$  and  $\lambda_{p,i-meas}$  are the measured peak field strength and period length at the  $i^{th}$  pole, respectively. The ideal peak field  $B_0$  and period length  $\lambda_{p0}$  are desirable values that we want to achieve. From the measurement of field amplitudes we can identify zero crossing points with a MATLAB program. The zero crossing is the point where the sign of the magnetic field changes and is represented by a crossing of the z-axis. In the case of small z-steps while measuring the field, a linear interpolation can be used to find exactly the crossing point with the z axis. From these crossing points the maximum and minimum peak fields and period length  $\lambda_p$  are determined. If the step size is not fine enough the field profile will be determined by a Fourier transform to the frequency domain and then fit all

the measured points in two adjacent poles by the sinusoid. This sinusoid fits all points involved in that zero crossing. To find the zero crossing point some algebra is needed. The measured peak field and period length containing 20 periods are performed in Figure 6.16. If the ideal field distribution is sinusoidal with the

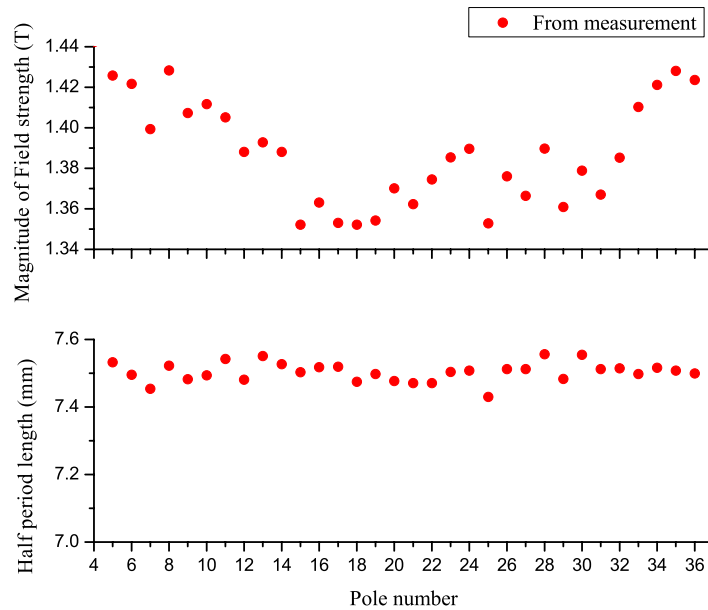


**Figure 6.16** The measured field and period length of the SCU poles at a current of 510 A.

desirable field amplitude and period length, the field and period length errors normalized to the values will be determined by following

$$\frac{\Delta B_i}{B_0} [\%] \text{ and } \frac{\Delta \lambda_{p,i}}{\lambda_{p,0}} [\%]$$

Figure 6.17 shows the field errors normalized to the minimum field amplitude of 1.3521 T, to the average value of 1.387 T and to the maximum field amplitude of 1.4283 T respectively. We will use different error deviations depending on the field correction method used. For the period length errors have been normalized to the average value of 15.007 mm and shown in Figure 6.18 because after the field error correction we would like to keep the period length only at the average value.

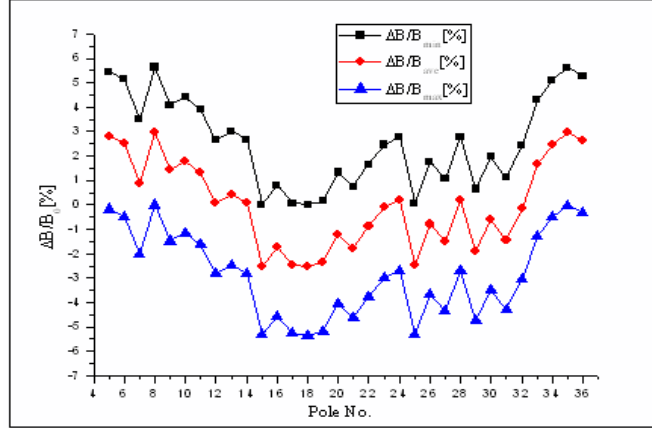


**Figure 6.17** Field errors normalized to the minimum (black square), to the average (red dots) and to the maximum (blue triangles) field amplitude.

**Table 6.2** Field errors

Normalized to	$\Delta B/B_0$	
	Minimum	Maximum
Minimum	0.0	5.63
Average	0.08	2.97
Maximum	-5.33	0

Both maximum and minimum field deviations are computed in Table 6.2 with an expression of the field deviation following Equation (6.7).

Standard deviations or root-mean-square (RMS) of the relative errors are good candidates to describe the field quality of the undulator. The standard deviations are defined by

$$\sigma_{\text{rms} - B} = \sqrt{\frac{1}{N} \sum_{i=5}^{36} \Delta B_i^2} \quad (6.8)$$

$$\sigma_{\text{rms} - \lambda} = \sqrt{\frac{1}{N} \sum_{i=5}^{36} \Delta \lambda_{p,i}^2} \quad (6.9)$$

where  $N = 32$  is the number of SCU main poles. Because of the high r.m.s errors

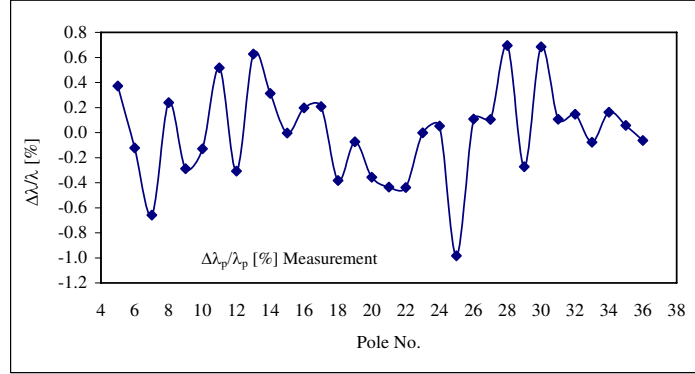


**Figure 6.18** Period errors  $\Delta\lambda_p/\lambda_{p0}$  normalized to the average (blue squares) value of 15.007 mm.

$\sigma_{\text{rms} - B}$  and  $\sigma_{\text{rms} - \lambda}$ , the ideal field  $B_0$  should be the minimum or the average values in order to reach the good field quality of the undulator. The errors  $\sigma_{\text{rms} - B}$  are 0.025 T and 0.04 T where the  $B_0$  is the average and minimum field amplitudes, respectively. The  $\sigma_{\text{rms} - \lambda}$  is 0.056 mm where the ideal period lengths are the average value.

### 6.5.1 Integral field measurement

Ideally, the total deflecting angle  $\alpha$  and displacement  $x$  of the electron beam from the axis should be zero at the end of the undulator. This total deflection angle is defined by an integral through all fields in the undulator as defined by

$$\alpha = -\frac{ec}{E} \int_{-\infty}^{\infty} B_y(z).dz = -\frac{e}{\gamma m \beta c} \int_{-\infty}^{\infty} B_y(z).dz \equiv x'$$

The factor  $\frac{e}{\gamma m \beta c}$  is normally defined in practical unit thus this factor becomes

$$\frac{e}{\gamma m \beta c} = \frac{0.2998}{\beta E(\text{GeV})}$$

This factor is a reversion of electron beam rigidity  $1/B\rho$ . As mentioned this angle should be zero for the whole undulator. In practice, however, a residual must be

expected and we call the first integral of the undulator

$$I_1 = - \int_{-\infty}^{\infty} B_y(z).dz \quad (6.10)$$

Any deflecting angle leads to a beam displacement  $dx = \alpha dz$ . This displacement also should be zero in an undulator. The residual displacement is determined by the second field integral which is the integral of the deflecting angle. A double integration of the magnetic field distribution is known as second field integral and defined as follows

$$I_2 = \int_{-\infty}^{\infty} dz \int_{-\infty}^z B(\alpha).d\alpha \quad (6.11)$$

Therefore, the residual displacement of the electron beam at the end of the undulator is from this

$$x = \frac{e}{\gamma m \beta c} . I_2 = \frac{e}{\gamma m \beta c} \int_{-\infty}^{\infty} dz \int_{-\infty}^z B(\alpha).d\alpha$$

and should also be zero. In real undulators this is not true due to manufacturing tolerances. In order not to perturb the electron beam for other users, both the first and second integral must be corrected by appropriately placed steering coils. There are several techniques used to measure the field integral; straight wire, flipping coil or using a Hall probe. In this thesis we use a straight wire and a Hall probe. In case of the straight wire the field integral can be directly measured but for the Hall probe the field integrals are obtained by an integration of the magnetic fields distributed along the whole magnet.

### **Integral field measurement**

First and second integral fields can be measured by a straight wire or flip coil system (Hwang et al., 2003) at room temperature. This technique is based on the induced voltage while moving a straight wire (Figure 6.19) across the magnetic

field. One side of the coil is stretched straight and held with two supports as shown in Figure 6.19. The induced voltage  $\frac{dV}{dt} \propto B\Delta x$  is integrated in the integrator, where  $B$  is the magnetic field density and  $\Delta x$  is the displacement of the wire. The

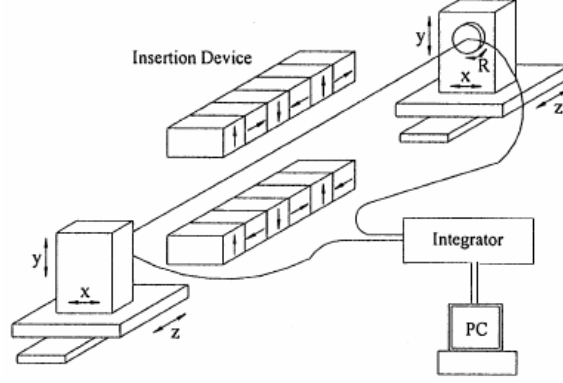


**Figure 6.19** Stretched wire diagram system.

first and second integrals can be measured by using this technique. The stretched part of coil cut the magnetic flux so then voltage is induced defined by

$$V = -N \frac{d\Phi}{dt} \quad (6.12)$$

where  $N$  is the number of turns of the stretched multistrand coil and the flux variation from moving the coil in the transverse plane is given by

$$\Delta\Phi = \iint B_y dx dz \sim \Delta x \int B_y dz \quad (6.13)$$

Assuming that the magnetic field is not changed while changing the horizontal position then the first field integral is

$$I_1 = -\frac{\int V dt}{N\Delta x} \quad (6.14)$$

Also the integral in the vertical axis can be obtained from induced voltage in time and the vertical displacement as in the horizontal axis. However the second field integral can be measured by moving  $x$  stage or  $y$  stage at the different side as

shown in Figure 6.20 and expressed by

$$I_2 = \frac{LI_1}{2} - \int_{-L/2}^{L/2} B_y(z) dz = \frac{L}{2} \left[ I_1 + \frac{L}{N\Delta x} \int V dt \right] \quad (6.15)$$

where  $\Delta x$  and  $\Delta y$  are the displacements on the transverse axis and  $L$  is the length of the stretch wire or length of the magnet. The first and second field integral

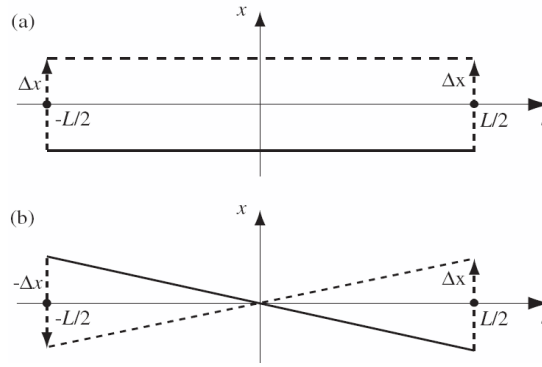


**Figure 6.20** Moving direction of the stretched wire to measure the first (a) and second (b) field integral.

can be converted to be the total deflection angle and displacement of the electron beam by dividing with the beam rigidity in the 1.2 GeV SIAM photon source (SPS)  $\beta E/ec$ , where  $E$  is the particle energy. The stretched wire is used mostly during multipole shimming of insertion device magnets because of the advantages of a simple measurement system and the speed of measurements at high precision.

### Integration of the field profile

To apply the wire technique in superconducting undulators is difficult due to the test dewar. The first and second integral fields can be directly obtained by integration of the measured fields in the transverse planes ( $B_x, B_y$ ) along the beam axes. Both, first and second field integral defined by (6.10) and (6.11), respectively can be obtained by integration over all measured vertical fields  $B_y$  along the beam

axis ( $z$ ). As a result, the measured first and second field integrals are  $-0.00114$  T.m and  $-0.00034$  T.m<sup>2</sup>, respectively. After dividing by the SPS beam rigidity  $\beta E/ec = 4.02$  T.m, the angular deviation and displacement of the trajectory are  $-285.1$   $\mu$ rad and  $-84.1$   $\mu$ m, respectively and are shown in Figure 6.21.

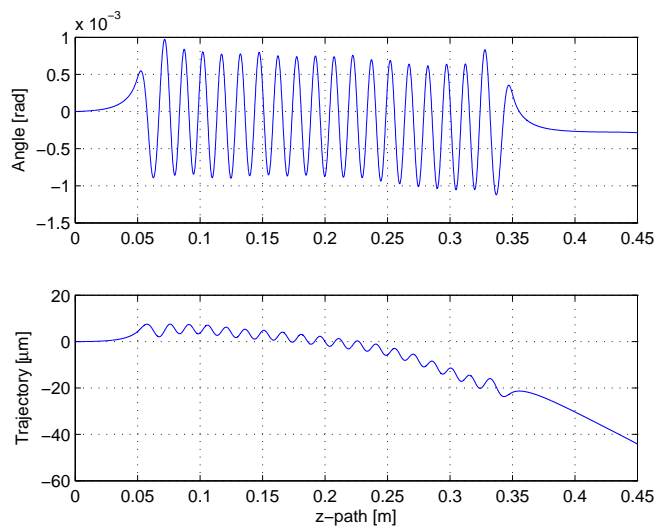


**Figure 6.21** Electron deviation in angle (a; first integral) and position (b; second integral) at an electron beam energy of 1.2 GeV ( $\gamma$  is about 2348).

Differences in the field amplitudes from period to period over the whole undulator are the cause of these residual integrals. It means that the electrons move through this undulator field with different deviations of the electron trajectory from the beam axis ( $z$ ) in each period. Thus the emitted radiations from each period cannot properly add up in the forward direction. The actual angular flux density for the real magnetic field of the SCU as measured at 510 A is calculated with B2E for an 1.2 GeV electron beam and a current of 200 mA and is shown in Figure 6.22. It is obvious that there are significant reductions on the flux density at the 3<sup>rd</sup> and higher harmonics due to magnetic field error of more than 1 %. Here the r.m.s field error normalized to the average and minimum field amplitudes are 1.8 and 2.9 %, respectively. In order to gain more flux density at all harmonics,

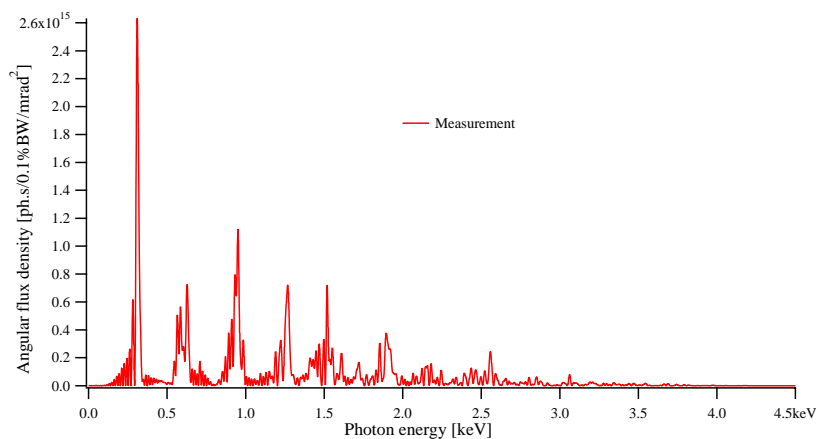


**Figure 6.22** Angular flux density calculated with B2E code at beam energy of 1.2 GeV and beam current of 200 A on-axis.

the field integrals and the field and period length errors must be reduced. It may be possible to reduce the errors by decreasing the mechanical tolerances by improved construction techniques of the SCU. This, however, requires time and money making the correction of an existing magnet all the more desirable. Different field correction techniques together with some measurements on a test magnet will be discussed and evaluated as to their usefulness as sources for high photon energies with high angular flux density.

# CHAPTER VII

## FIELD CORRECTION OF UNDULATOR

To reach hard X-ray photon energies in a low energy storage ring, superconducting undulators are desired. Only in superconducting undulators we may reach high field strength at  $K$ -values higher than unity. For  $K$ -values of 2 to 3 radiation is generated at higher harmonics, thus allowing to reach high photon energies. The angular photon flux density at such higher harmonics, however, will depend greatly on the quality of the undulator magnet. Ideal intensities require close to perfect superconducting undulator fields and we try to develop means to correct undulators to near perfect condition. For an undulator to work near perfect, all periods must be the same so that the radiation from each period can constructively interfere with radiation from other periods for high brightness quasi-monochromatic radiation. There are two kinds of errors, phase errors and field amplitude errors, both related to mechanical machining and assembly tolerances. More tolerances occur during cool down to cryogenic temperatures. Although the first and second field integrals are corrected close to zero, the errors on the field amplitude and period length per individual period still remain. A high photon flux density can not therefore be reached at higher harmonics of the radiation. Correction techniques are required in order to reach close to ideal photon flux densities at higher harmonics. Corrections used for room temperature undulators will not work for superconducting undulators and we will therefore only discuss possible correction methods for superconducting undulators in this Chapter including their advantages and limitations.

## 7.1 Introduction

Angular photon flux density and radiation brightness are adversely affected by amplitude and phase errors especially at higher harmonics of the radiation. Therefore those errors must be held within small tolerances over the complete length of the undulator. From field measurement, discussed in Chapter VI peak fields vary between 1.3521 T and 1.4283 T with an average value of 1.387 T. The average half period length from the same measurements at an excitation current of 510 A is 7.5036 mm for an average period length of  $\lambda_p = 15.007$  mm and the field deviations normalized to the average peak field  $\Delta B/B_0$  and  $\Delta\lambda_p/\lambda_{ave}$  are shown in Figure 7.1. From the measurements, we can see that there is a significant

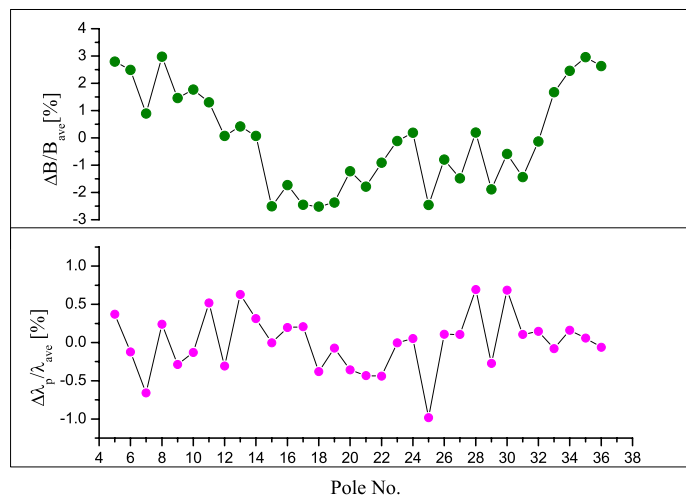


**Figure 7.1** Field amplitudes (upper) and period lengths normalized to the average field of 1.387 T and 15.007 mm, respectively.

peak field variation with an r.m.s field error of  $\sigma_{rms-B} = 1.8$  % normalized to the average peak field value. The variations in the period length are smaller with an r.m.s period length of  $\sigma_{rms-\lambda_p} = 0.37$  %. We will use this magnet as a reference undulator to evaluate different error correction methods. First, we define from this real magnet an idealized undulator with a perfect sinusoidal field distribution

and a peak amplitude of 1.387 T. The period length we choose is to be equal to the average period length  $\lambda_p = 15.007$  mm of the test magnet. The field profile of this reference undulator is shown in Figure 7.2 created mathematically by a sine wave with two end poles on either side of the undulator. Since the end pole field strengths contribute significantly to the field integrals we must adjust the magnetic field strength of these end poles such that the first and second integrals are zero within numerical round-off errors in order not to disturb the trajectory of the electrons passing through the undulator. Numerical integrations of the field in this idealized reference undulator in Figure 7.2 give values of  $3.96 \times 10^{-9}$  T.m and  $8.30 \times 10^{-9}$  T.m<sup>2</sup> for the first and second field integral, respectively. These values are negligible small for any real situation. Figure 7.3 shows the angle and lateral displacement of the electron beam at an electron energy of 1.2 GeV for the idealized undulator.

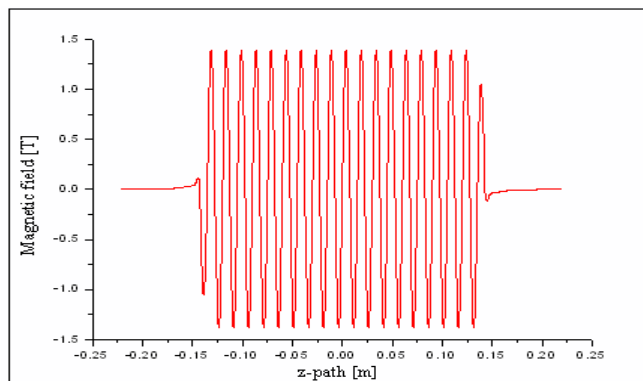


**Figure 7.2** Magnetic field distribution in the idealized undulator along the beam axis with field amplitude of 1.3870 T and a period length of 15.007 mm.

Our goal now is to correct the real undulator as close as possible to the idealized reference undulator. The two field integrals are important for the stability of the electron beam path in the storage ring. Even small changes can affect adversely the integrity of data by another experimenter although the beam proper

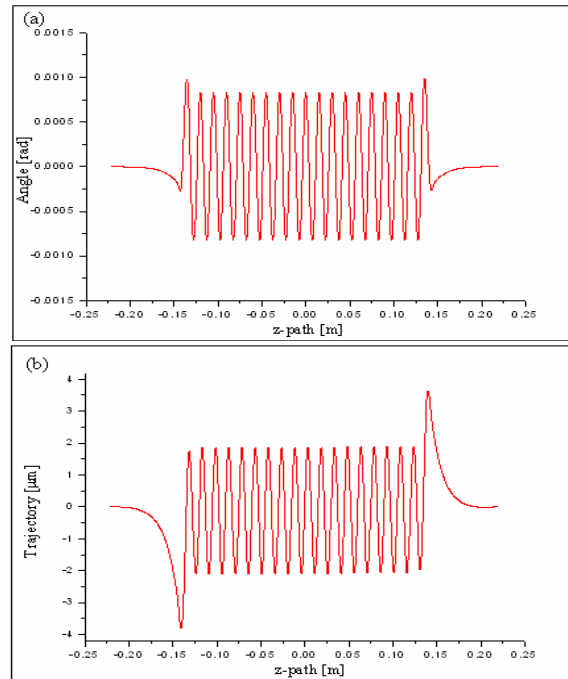


**Figure 7.3** Angle (a) and trajectory (b) deviation of the electron beam at an energy of 1.2 GeV passing through idealized undulator.

would not be lost. To get the maximum photon beam density, additional constraints must be observed. For best photon beam quality the peak fields and the period length in all periods must be equal within close tolerances. In essence, we require that the fields in each period must be the same. Errors appear as changes in the field amplitude and period length of the undulator as shown in Figure 7.4 and are the cause of reduction in angular flux density in the photon beam. As in section 4.5 we saw that the angular flux density at the 7<sup>th</sup> and the 9<sup>th</sup> harmonics of the radiation will be decreased by more than 10 % when the real period length or phase error exceeds about 1 degrees. Therefore the period length error should be less than 1 degree or about 0.25 % normalized to the average value. For the same reduction on the photon flux density at high harmonics the field amplitude error must be smaller than 1 %. However in our test undulator, the r.m.s field error is close to 2 % and the period length error is about 0.4 %. We may calculate

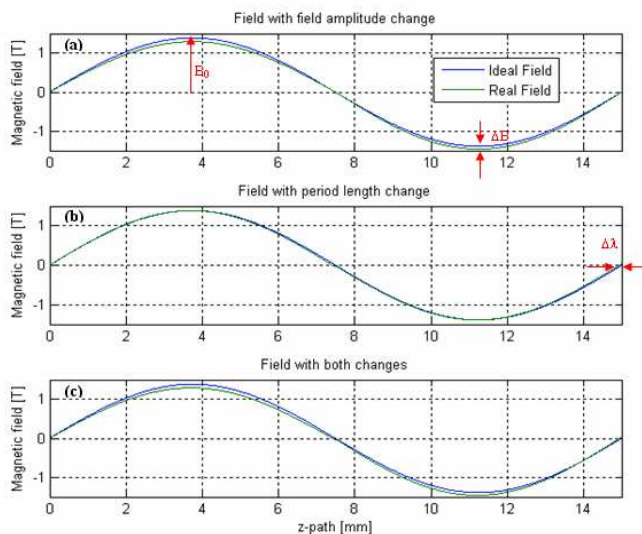


**Figure 7.4** Magnetic field distribution with a field strength of 1.3870 T and period length of 15.007 mm including field errors of 5 % (a) and a period length or phase errors of 3.5 degree (b) and both field and phase errors (c).

the angular flux density with the numerical computer program B2E for this real field and get a photon spectrum as shown in Figure 7.5 where the flux densities from the real and ideal magnetic field distribution are compared. The reduction of the flux density (and brightness), especially at higher harmonics is dramatic and emphasizes the need for field correction. There is a large reduction of about a factor of two at the fundamental harmonic caused by the r.m.s field errors of 1.8 % in addition to a large value for the first field integral. In reality, the r.m.s field error serves only to quantify the field quality but the actual field errors vary by as much as 3%. There are large field errors causing the reduction on the angular flux density even while the period length error is less than 1 %. Since the field integrals are large, the photon beam is not emitted in the forward direction and the radiation is emitted into an angle with respect to the axis thus leading to a red shift of the radiation. In B2E code the observation angle in horizontal axis is

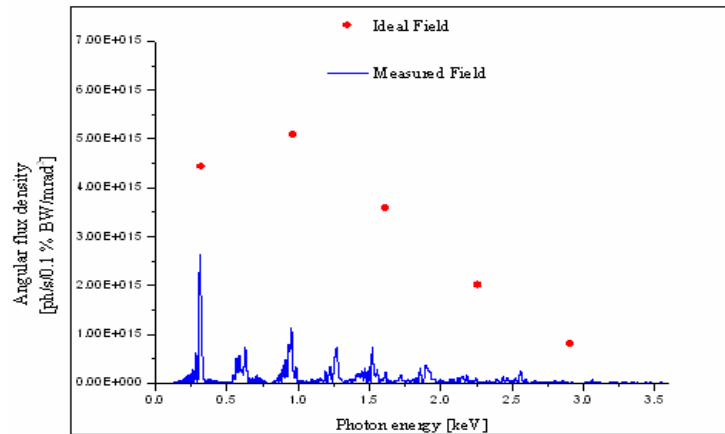


**Figure 7.5** Angular photon flux density for the real test magnet compared with the idealized undulator. Note the appearance of even harmonics due to field and phase errors.

multiplied with the relativistic factor  $\gamma$  and expressed by

$$\text{Horizontal angle} = \gamma \times \alpha$$

where  $\alpha$  is the change in the angle. If the horizontal angle is -0.14 to -0.22 the photon flux density at the 1<sup>st</sup> harmonic can be increased more by a factor of 1.2 of the flux density at the forward direction (zero observation angle). Due to unconstructive adding up of the photon the field integrals should be reduced close to a small value as possible.

## 7.2 Field integral correction

From measurements we observe that the beam displacement is progressively increasing within the length of the undulator exhibiting a curved appearance. This curvature as shown in Figure 6.21(b) must be corrected uniformly along the undulator with a long dipole field distributed along the whole length of the undulator. This can be accomplished with two long coils surrounding either all upper or lower

undulator poles. After elimination of the curved perturbation of the electron trajectory within the undulator we may use two more short dipole fields (coils) on either side of the undulator to correct for angle and position (first and second field integral) at the exit of the undulator. The long coil shown in Figure 7.6 has 4 turns in each of 4 layers with a wire diameter of  $0.89 \times 0.53 \text{ mm}^2$ , a coil length of 300 mm (in the  $z$ -direction) and a width of 100 mm (in the  $x$ -direction). Applying only the long coil field the first and second field integrals are reduced to  $1.39 \times 10^{-7} \text{ T.m}$  and  $1.01 \times 10^{-7} \text{ T.m}^2$ , respectively. The first and second field integrals are reduced by a factor of  $10^4$ . Figure 7.7 shows a comparison of the field integrals between before and after correction of the changes in position of the electron beam. Because of the remaining second field integral and other field errors still

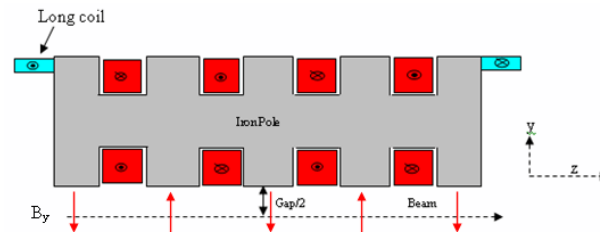


**Figure 7.6** A cross-section of the SCU (schematic) with the long coil energized with a current of 18 A (current density of  $40 \text{ A/mm}^2$ ).

not corrected only the first and the third harmonics of the radiation have more the angular flux density but not at the higher harmonics shown in Figure 7.8. Only at the  $1^{st}$  and  $3^{rd}$  harmonics, the flux densities are increased about 76.4 % and 67.7 % of the flux density of the ideal field respectively. To keep decreasing the second field integral a correction coil energized with an excitation current of 5 A is used to reduce this value to  $1.41 \times 10^{-8} \text{ T.m}^2$ . However there is no improvement on the flux density at higher harmonics due to variations in the field amplitudes and the period length each period. Thus to reach the high flux density as the ideal

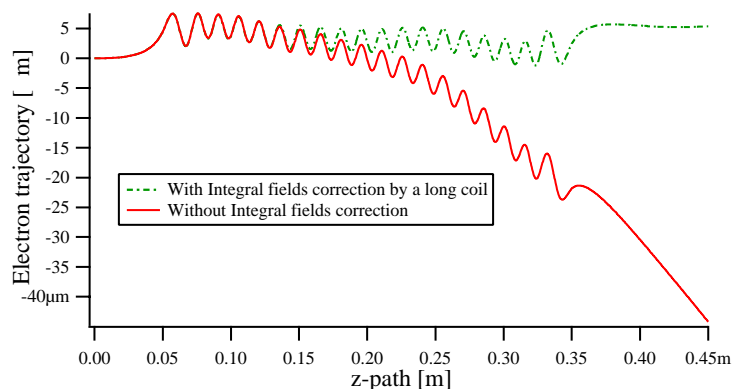


**Figure 7.7** Electron trajectory with (dash line) and without (solid line) the correction of first and second field integrals.

undulator we need to compensate the errors to be less than the 1 % the field error by using some correction concepts discussed later. In the following sections we will

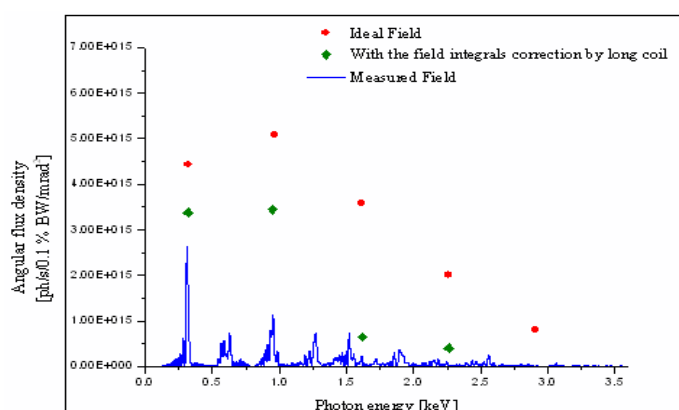


**Figure 7.8** Comparison of the angular flux density with and without field integral corrections.

discuss a variety of correction methods with varying degree of effectiveness.

## 7.3 Shimming method

Field correction by shimming is generally applied to permanent magnet undulators at room temperature by placing thin ferromagnetic material or iron foils on the surface of undulator poles in order to alter field and phase. The errors in permanent magnet undulators result from inhomogeneities of the magnetization inside the magnet blocks and can be reduced by either alignment of the magnet blocks, mechanical shimming or by placing iron pieces at the surface of the magnet. The iron becomes magnetized when the undulator is energized and contributes mostly to the local magnetization. A special approach to iron shimming has been used in our test SCU and measurements have been performed with the goal to improve the field homogeneity of the superconducting undulator like in permanent magnet. The magnetic field changes depend directly on the height and the location of the iron shims. We also used a shim coil wound around the trim pole to introduce further field variations which could be used for correction (Jan et al., 2009).

### 7.3.1 Simulation of iron-trim

To understand the iron shim effect on the change in the peak field the full-size shimming is simulated with the code RADIA. Figure 7.9 presents a 3-D configuration of the superconducting undulator with an iron shim placed on the 21<sup>st</sup> undulator pole which has positive field strength. This was done to find out the magnitude of the field correction possible, but also the spatial extend of the field alterations. Ideally, we would like to get a field change only in the pole of the undulator where we place the shim. All the simulated notations of the trim pole and shim coil are presented in Figure 7.10;  $vz = 0.1$  mm,  $t = 8$  mm,  $gap = 5.6$  mm,  $D = 2.85$  mm (equal to the pole width),  $dd = 0.1$  mm,  $dtp = 4$  mm and  $Hc = 4.45$  mm; varying  $hd$  (iron height). In the calculation the trim pole is made

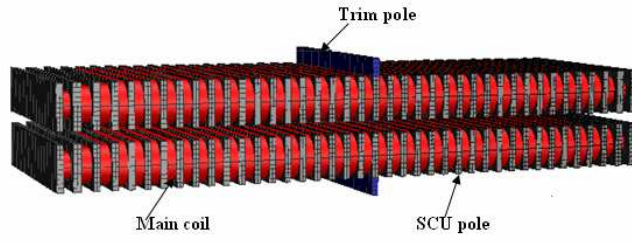


**Figure 7.9** The SCU array with the trim pole (blue), main coil (red) and the SCU pole (gray) as used in RADIA simulations.

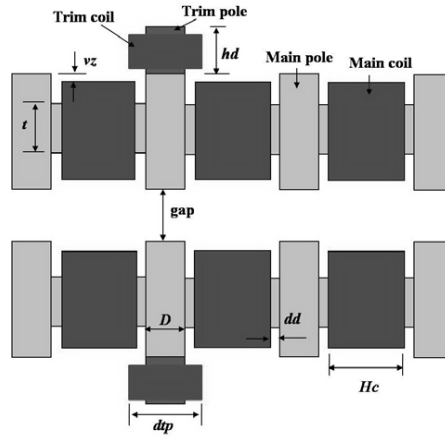


**Figure 7.10** Sketch of the trim pole and the shim coil mounted on the undulator pole used in the RADIA code.

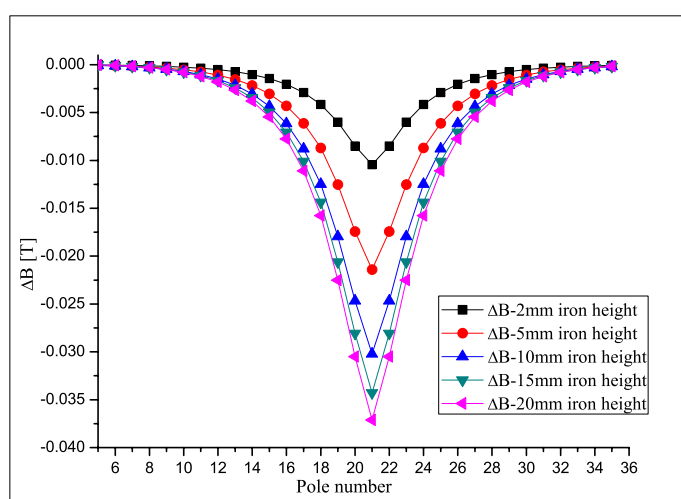
from low carbon steel (carbon content  $C < 0.06\%$ ) which is the same material as the undulator poles. The trim pole length and width are fixed at 99.86 mm and 2.85 mm, respectively matching the SCU pole dimension while the height of the trim pole is varied from 2, 5, 10, 15 to 20 mm. The field amplitude changes at the  $i^{th}$  poles  $\Delta B_{i,cal}$  is defined by

$$\Delta B_{i,cal} = B_{i,trim\ pole} - B_{i,ideal} \quad (7.1)$$

where  $B_{i,ideal}$  is the ideal field amplitude without the trim pole. Applying a single trim pole at the 21<sup>st</sup> undulator pole the field strength is reduced as shown in

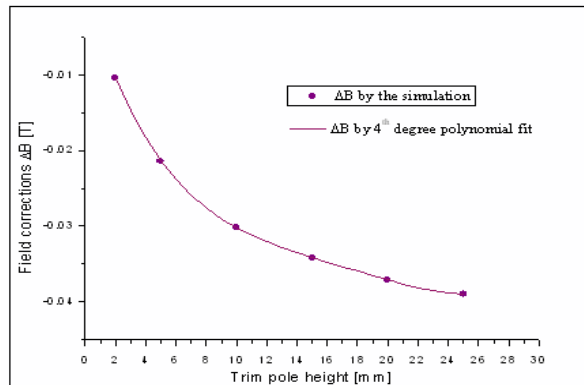
Figure 7.11 where we also observe a change in the field of nearby poles. The relative change in the field of neighboring poles is about 2.3 % for a 20 mm trim pole and less for smaller trim poles. In Figure 7.11 lines are drawn only to guide the eyes. We can see clearly that the trim pole cannot produce localized field changes. As a result the correction of a field error at one pole by the iron shim is accompanied by an almost equal field perturbation in neighboring poles. This makes the field correction by shimming non-practical in superconducting magnets.

Figure 7.12 shows the results of measurements. First, we notice that the



**Figure 7.11** Field deviations from the ideal field amplitude due to a trim pole attached to the 21<sup>st</sup> pole. The trim pole width and length match the width and length of the SCU pole but the thickness of the trim poles vary from 2 mm (black), 5 mm (red), 10 mm (blue), 15 mm (green) to 20 mm (pink).

field is reduced due to the trim poles and this field reduction is a function of the trim pole height. This dependence is fit with a 4<sup>th</sup> degree polynomial and using this relation the height of the trim pole can be obtained to perfectly correct the field error. Simulations with the code RADIA produce the same results as the measurements which give us the confidence to use simulations where measurements



**Figure 7.12** Field correction as a function of trim pole height. Dots represent simulated results and solid lines represent a 4<sup>th</sup> degree polynomial fit to the measurements.

are not available or difficult/expensive to obtain.

### 7.3.2 Simulation of trim coil

During tests of the SCU we also energized the trim poles with electrical coils. The effect of such trim coils can be simulated with RADIA. The trim coil is made of 0.33 mm diameter NbTi superconductive wire and is wound around the trim pole. The height and thickness of the windings on the trim coil are 19 mm (hs) and 1.5 mm with 222 turns, as shown in Figure 7.10. The trim pole with coil is attached on the 20<sup>th</sup> undulator pole. The relative field amplitude changes are defined by following

$$\frac{\Delta B_i}{B_{i,\text{trim}}} [\%] = \frac{(B_{i,\text{shim - coil}} - B_{i,\text{trim}}) \times 100}{B_{i,\text{trim}}} \quad (7.2)$$

and are shown in Figure 7.13. The  $B_{i,\text{trim}}$  represents the field amplitude in each pole with the trim pole mounted on the undulator pole and  $B_{i,\text{shim}}$  is for the field amplitude with trim pole winding by the shim coil energized with a current of 10 A (77.2 A/mm<sup>2</sup>) and 15 A (115.8 A/mm<sup>2</sup>). The field strength at the undulator pole is increased or decreased by the shim coil current. If the current flows in

the opposite direction of the main current the field strength at that pole will be reduced. Unfortunately, the field changes are again not localized but spread out over several nearby poles.

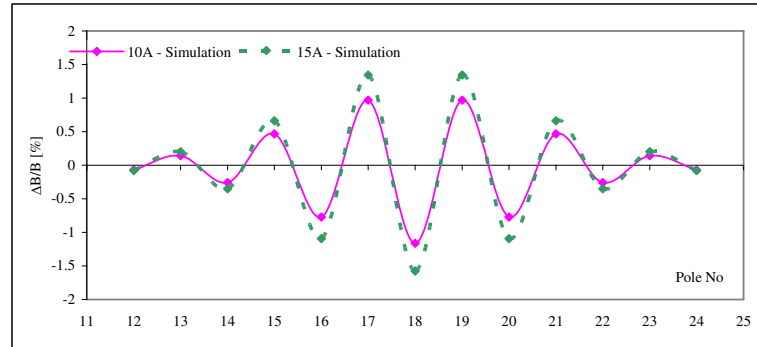


**Figure 7.13** Relative field amplitude changes due to an iron trim pole with coil as simulated in RADIA. The shim coil mounted at the 20<sup>th</sup> pole is powered with currents of 10 A and 15A.

### 7.3.3 Experimental setup and result

To investigate the effectiveness of the shimming technique to correct field errors in the superconducting undulator both simulation and experimental results should be compared. From experiments with trim poles we know that the fields are reduced. Some of the undulator poles like the 6<sup>th</sup> and 35<sup>th</sup> pole have high fields with amplitudes of 1.4283 T and 1.4281 T, respectively. We try to reduce those fields to the average field of 1.387 T. On the other hand, the field amplitude at the pole number 18 is at the minimum value of 1.3521 T and we attach here a coil to a 25 mm trim pole so that the field amplitude can be increased. The trim irons and coils shown in Figure 7.14(a) were directly mounted on the shimmed main pole using an SS316L clamp; each clamp fixes two pieces of trim iron and coil, as presented in Figure 7.14(b). Pin indicates the position between the trim iron and

the beam duct. Additionally, to test the field quality improvement trim irons of height 5, 25 and 15 mm are mounted on the 6<sup>th</sup>, 18<sup>th</sup> and 35<sup>th</sup> poles, respectively. The magnetic field distribution of the SCU magnet with the trim irons has to

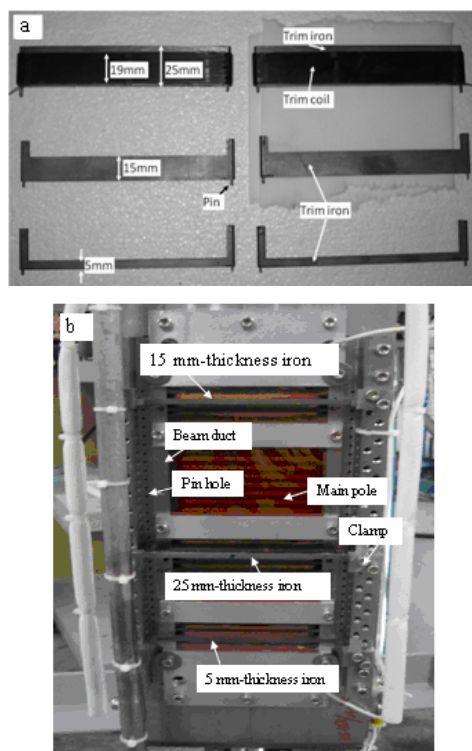


**Figure 7.14** Setup of the trim iron and coils (a) varying height of the iron-trim and profiles of the trim coils, (b) assembly of the iron trim pole winding with iron heights of 5, 25 and 25 mm mounted at the 6<sup>th</sup>, 18<sup>th</sup> and 35<sup>th</sup>, respectively on the beam duct.

be measured at an excitation current of 510 A through the main coils. All the conditions including the excitation current have to be the same as in previous field measurement presented in Chapter VI to allow comparison of the results with and without trim poles. During the field measurements the excitation current energized through the trim coils are set to be zero to study only the effect of the iron-trim on the field and period length deviations. After reaching a temperature of 4.2

°K the magnetic field is measured and compared with the field without the trim poles shown in Figure 7.15. The field differences normalized to the measured field without the trim pole are defined by following

$$\frac{\Delta B_i}{B} [\%] = \frac{(B_{i,\text{trim pole}} - B_{i,\text{without trim pole}})}{B_{i,\text{without trim pole}}} \quad (7.3)$$

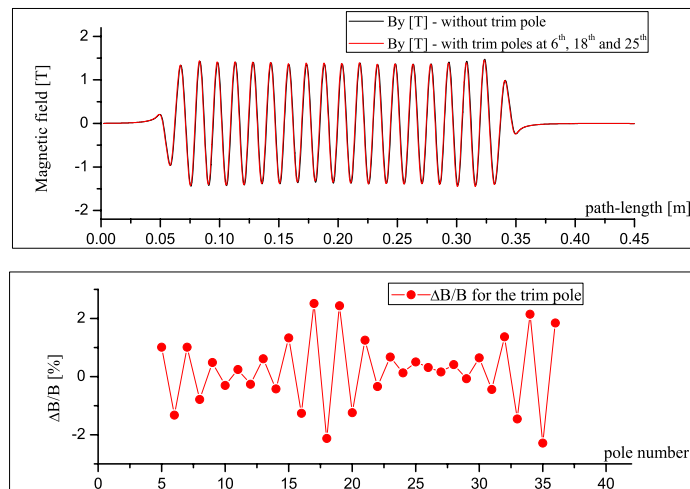


**Figure 7.15** Field measurement without shimming (blue solid line) and with trim-iron shimming (red solid line) presented in the upper part. Field deviations normalized to the non-shimming field amplitude are presented in the lower part. Trim iron of height 5 mm, 25mm and 15 mm are attached on the pole number 6<sup>th</sup>, 18<sup>th</sup> and 35<sup>th</sup>, respectively.

To predict all the simulated concepts used to improve the magnetic field correction the simulation result for the SCU with trim-irons should be compared with the measurement. In the RADIA code three iron pieces are attached at the same poles as in the measurements. The field strength and period length resulting from the experiment are compared with the simulated results as the height of the iron trim is varied and shown in Figure 7.16. The small difference between experimental and simulated results reflects the error in the setting of parameters

in the simulation and the mounting error of the trim iron on the SCU magnet. Differences between the experimental and simulation results may be caused by

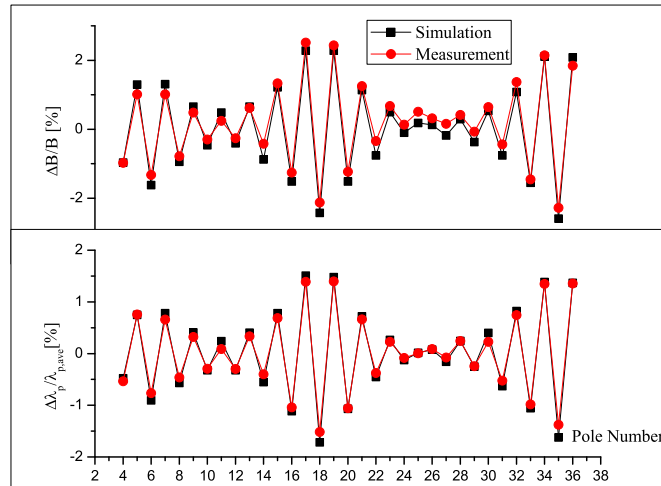


**Figure 7.16** Comparison between experiment and simulated results of trim-iron shimming at the pole number 6, 18 and 35.

the assembly of the trim pole with the undulator poles because the magnetic gap was slightly changed when the trim iron of height 25 mm was mounted. The experimental field-strength corrections (period length) are around -1.3 %(-0.8 %), -2.1 %(-1.5 %) and -2.3 %(-1.4 %) at the corrected pole with 5, 25 and 15 mm trim-iron height, respectively. After correction with trim poles shown in Figure 7.17 field errors normalized to the average field amplitude of 1.3899 T at the corrected pole (the 6<sup>th</sup>, 18<sup>th</sup> and 35<sup>th</sup>) can be reduced only at the pole number 6<sup>th</sup> and 35<sup>th</sup> because of the minimum field amplitude at the 18<sup>th</sup> pole. Therefore the error at the 18<sup>th</sup> pole will be reduced only by using the shim coil energized with negative currents due to the field strength has a negative sign at this pole.

Due to the effect of the trim poles on the neighboring poles the field errors can not be reduced to reach field errors of less than 1 %. The shimming technique does not work for this undulator. Also the changes in period length at the corrected

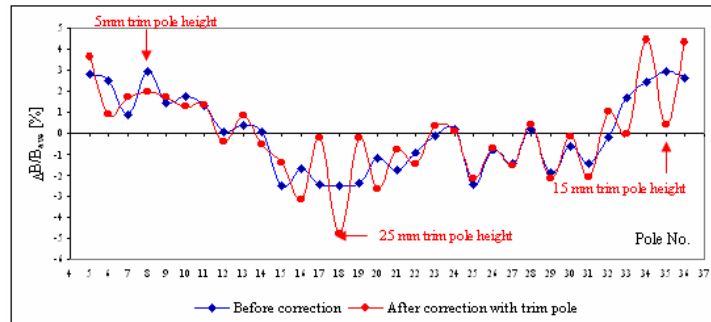


**Figure 7.17** Comparison of the field errors normalized to the average values before (blue dots) and after (red dots) correction. The average field amplitudes before and after correction with the trim poles are 1.3870 T and 1.3899 T.

poles normalized to the average values cannot be decreased to acceptable values. The maximum period length error actually increases to r.m.s  $\sigma_{r.m.s-\lambda_p}$  of 1.9 % normalized to average period length of 15.124 mm after correction as shown in Figure 7.18. We arrive at the result that correcting fields with trim-iron poles the

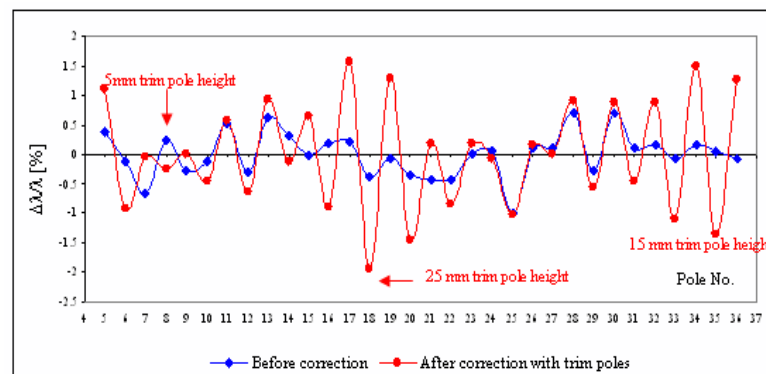


**Figure 7.18** Comparisons of period length changes normalized to the average values with and without correction by coil trimming. The average period lengths with and without shimming are 15.007 mm and 15.124 mm, respectively.

field and angular flux density cannot be improved even if the first and second field integrals are corrected to  $-4.11 \times 10^{-4}$  T.m and  $-4.31 \times 10^{-4}$  T.m<sup>2</sup>, respectively. This means that the shimming as used in conventional undulators does not work

for superconducting undulators. The value of this experimental exercise, however, is that we obtained a close match between measurement and simulation which gives us the confidence to rely on simulations alone since measurements are time consuming and very costly.

## 7.4 Field correction with additional coils

In this concept we consider additional coils wound around each pole. This will require many power sources and feeds from room temperature to cryogenic temperatures and the correction becomes rather complex in practice. We will, however, discuss this scheme because it is obviously the most effective. From Ampere's Law the magnetic flux density  $\vec{B}$  or its change is given by

$$\oint \vec{H} \cdot d\vec{s} = \int \vec{J} \cdot d\vec{A}$$

$$\frac{1}{\mu_r} \oint \vec{B} \cdot d\vec{s} = \mu_0 I_{tot}$$

where  $\vec{J}$  is current density and  $\mu_r$  is a relative permeability which is the ratio of the permeability of specific medium to the permeability of free spaced and given by

$$\mu_r = \frac{\mu}{\mu_0}$$

The field generated is proportional to the total electrical current  $I_{tot}$  enclosed by an Amperian loop. The Amperian loop has to be a closed path along  $d\vec{s}$  which, in the case of this undulator is shown in Figure 7.19. With the windings of the superconductive wire in a vertical plane a magnetic field  $\vec{B}_y$  is generated at the location of the electron beam in the mid plane at  $(x = 0, y = 0, z)$ . From the path along the loop, a pure vertical magnetic field deflecting exist only in the mid plane while the other components of the magnetic fields disappear. The additional coil can produce a uniform magnetic field when an electrical current is passed through

it. It is treated as the source to reduce or increase the magnetic field strength for a pole based on Ampere's Law and the right hand rule. Therefore to correct the errors, local additional coils powered with different currents are required. The total current in the coils depends on the number of turns and the maximum current on the size of the superconducting wire.

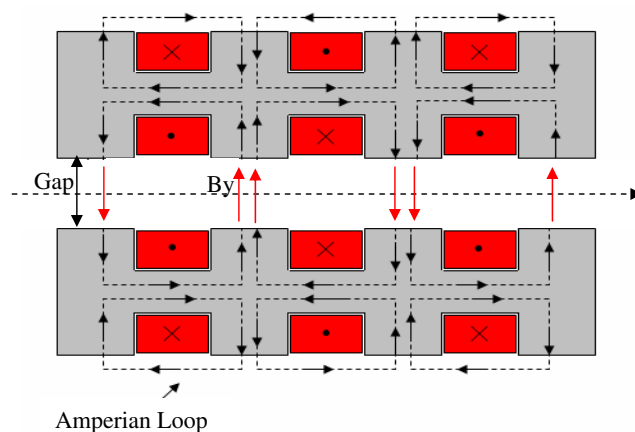


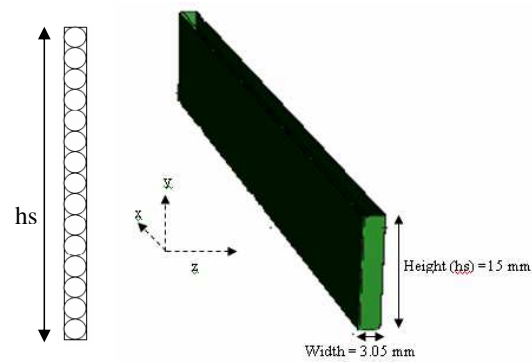
**Figure 7.19** Superconducting undulator (SCU15, schematic) in two dimensions with the Amperian loop producing a vertical magnetic field.

#### 7.4.1 Superconducting additional coil around the undulator pole

Due to the limited space between the main undulator coil and pole a superconducting wire made from NbTi with an insulated diameter of 0.1 mm and high current density capability is used. The NbTi wire is embedded in a copper matrix with a ratio of Cu to SC of 1.35. Some more parameters of the wire are shown in Table 7.1. A coil in form of a racetrack is shown in Figure 7.20 with a height of 15 mm. The coil is wound around the 21<sup>st</sup> pole to determine the field change there and in neighboring poles. A critical current of the NbTi wire directly relates to the maximum magnetic field as shown in Figure 7.21. Therefore, to avoid

**Table 7.1** Superconducting wire specification for the correction coil

Cu/SC ratio	1.35
Insulated diameter	0.1 mm
Bare diameter	0.08 mm
Number of filaments	54
Filament size	7 $\mu\text{m}$
RRR of Cu matrix	77

**Figure 7.20** Racetrack of the superconductive NbTi wire with 0.1 mm diameter.

quenching, the current through the correction coils should not be more than the critical current of 20.34 A corresponding to a current density of  $2050 \text{ A/mm}^2$  at 1.4 T and  $4.2 \text{ }^\circ\text{K}$ . In the RADIA code the correction coil is wound around the pole number 21 and is energized at different currents. The field changes  $\Delta B_{\text{correct-coil}}$  at the corrected pole (the 21<sup>st</sup>) is about 41.8 mT per 20.34 A as shown in Figure 7.22. The field change  $\Delta B_{\text{correct-coil}}$  is

$$\Delta B_{i,\text{correct-coil}} = B_{i,\text{correction coil}} - B_{i,\text{ideal}}$$

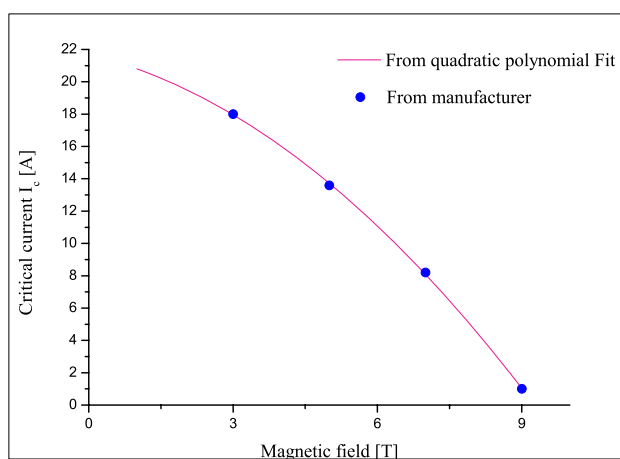


**Figure 7.21** Critical current of the NbTi wire with 0.1 mm diameter measured by the manufacturer (dots) and by a quadratic polynomial fit (solid line). The critical current at 1.4 T and 4.2 °K is 20.34 A.

The field changes by the correction coil are very localized and the field changes in nearby poles are only 8.7 % of the field amplitude change at the corrected pole. This provides an efficient way of correcting the field in individual poles. In addition, the correction also produces a local change in the period length. The current through

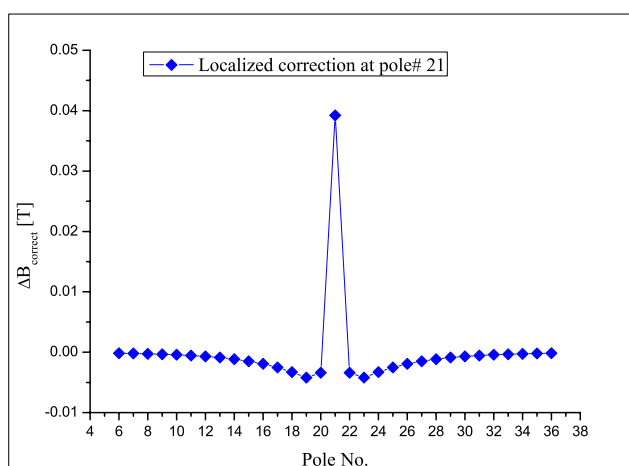


**Figure 7.22** Field variations due to a correction coil powered by a current of 20.34 A. The correction coil is wound around the pole # 21.

the correction coils is linearly proportional to the field changes when the currents

are adjusted. The relation between the current and field amplitude change is shown in Figure 7.23 and described with

$$I_{i,corr} = p_1(\Delta B_{i,correct-coil}) + p_0$$

By the linear fit, the constant  $p_1$  and  $p_0$  are  $7.539 \times 10^4$  and  $-990.6 \text{ A/mm}^2$ , respectively. This result is used to calculate the current required for the field correction at each pole. In general, the goal of field correction is to obtain equal

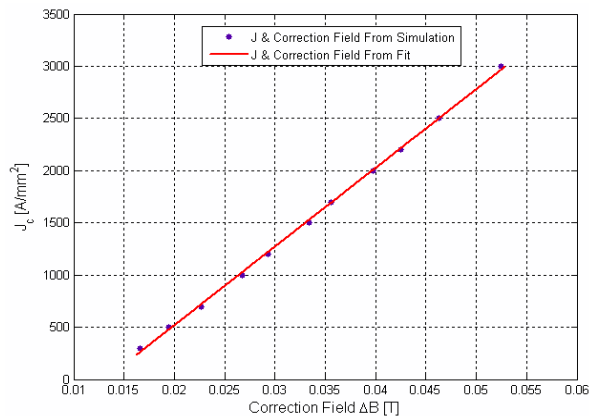


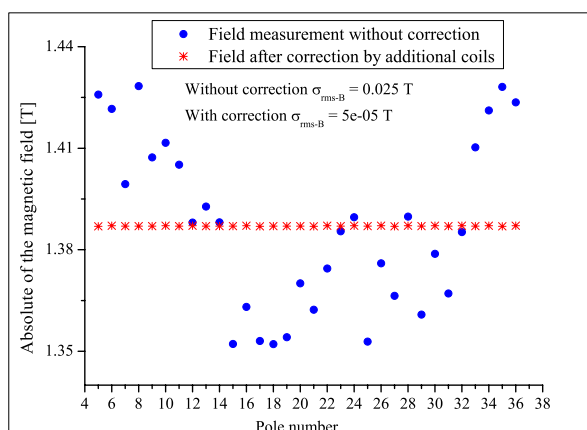
**Figure 7.23** Required current as a function of desired field correction. The correction coil has a diameter of 0.1 mm and 15 turns.

peak fields with a small r.m.s field variation  $\sigma_{r.m.s-B}$  as a result of an appropriate set of currents in the correction coils. It means that the peak field amplitudes in each half period are equal except for the sign. The correction field  $\Delta B_{i,correct-coil}$  at a particular pole is related, in principle, to the excitation currents in all poles through a matrix  $M_{ij}$ . The matrix has dimensions  $i \times j$  where  $j$  is the number of the corrected pole and  $i$  is the number of all poles with correction coils. In this study only the main poles but not the end poles have been corrected. Therefore, the total number of corrected poles is 32 and  $0 < i < 32$ . By inversion of the matrix we can determine the desired currents in each coil to correct for the perfect peak fields as discussed in the Chapter III. To avoid quenching in any part of the

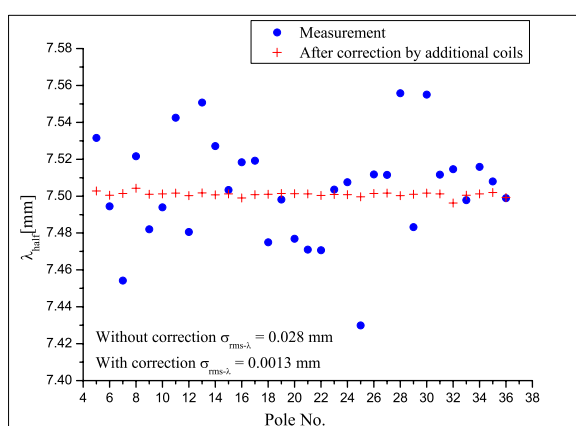
SCU the current density or the current in the correction coils should be well less than  $2000 \text{ A/mm}^2$  or 20 A, respectively. Since Maxwell's equations are linear, the fields generated by individual correction coils can be added to the real field and to create the perfect undulator the real field amplitude and the correction field are added together so that corrected fields at all the poles are obtained and described by following

$$B_{i,\text{correct}} = B_{i,\text{meas}} + \Delta B_{i,\text{correct} - \text{coil}}$$

After applying the correction to the main field  $B_{i,\text{meas}}$  at all undulator poles the peak fields in the whole undulator should be the same at the desirable field amplitude. The correction is limited though due to the superconducting performance limitation of the NbTi wire. According to simulation, the maximum field change as limited by the wire is about 0.04 T. To maximize the correction capability, we choose the average field amplitude as the ideal or desired field. A MATLAB program was used to correct the field errors to the least r.m.s field error  $\sigma_{r.m.s-B}$  which turned out to be less than 0.0001 T or about the magnitude of the earth magnetic field. In the calculation independent power supplies are required. Absolute field amplitudes at the main poles with and without correction coils are shown in Figure 7.24(a). In addition Figure 7.24(b) shows a comparison of the period length with and without correction. Using this local correction scheme both field and phase errors are reduced so that the field amplitude and period length after correction is close to the field of 1.387 T and close to the average period length of 15.007 mm. With perfect compensation the r.m.s field and period length errors are 0.0036 % and 0.02 %, respectively.



(a) Field Magnitude



(b) Period

**Figure 7.24** Comparison of the absolute magnetic field amplitude (a) and period length (b) with and without correction coils. The magnetic field is measured at 510 A.

### Model for a real magnetic field

In order to prove the concepts the improvement of the field and phase should eventually improve the angular flux density at high harmonics. To carry out experiments at cryogenic temperatures is very costly and simulations of the magnetic field profile along the beam axis has been generated to calculate an angular flux density to be confirmed that this concept achieve the high photon flux density at high harmonics of the radiation. In order to calculate the angular

flux density for a realistic field distribution, we need a model for the real magnet with errors. Using this real model in B2E we then can calculate the harmonic spectrum of the radiation based on the actual magnetic field. This we accomplish starting from an ideal undulator with specifications equal to the SCU as discussed in section 5.2.1. Then we modify the main coil currents such that the resulting fields are equal to the measured field before any correction. In essence we have assumed that the field variation has been caused by variations of the current in different main coils although this may actually be the least likely source of field errors. Since we do not know the exact source of the errors we proceed in the way described to generate a real undulator model magnet in RADIA and we will now use this model to test the efficiency of correction methods in terms of angular flux density with the program B2E. To compare both simulated and measured field errors they have to be normalized to the average value of the field amplitude. Figure 7.25 presents the field errors normalized to the average field amplitude obtained from the measurement and re-construction of the magnetic field in the mid plane. The field errors  $\frac{\Delta B}{B_{ave}}$  after correction with correction coils are shown in Figure 7.26 with an average field amplitude of 1.387 T and relative remaining field error of 0.0036 % normalized to that field. Due to the localized coil correction, the period lengths also are improved after correction as is evident in Figure 7.26.

We also calculate the first and the second field integrals for the corrected magnetic field distribution along the beam axis. Because of the improvement in each period field integral the first and second field integral for the whole undulator are reduced to  $6.403 \times 10^{-6}$  T.m and  $6.334 \times 10^{-6}$  T.m<sup>2</sup>, respectively. Since the magnitude of the period field integrals were made mostly to become the same along the undulator they result in a reduction of the first and second field integrals for the whole magnet. The first and second field integrals are now quite small but they are not exactly zero as in an ideal magnetic field. The electron beam passing

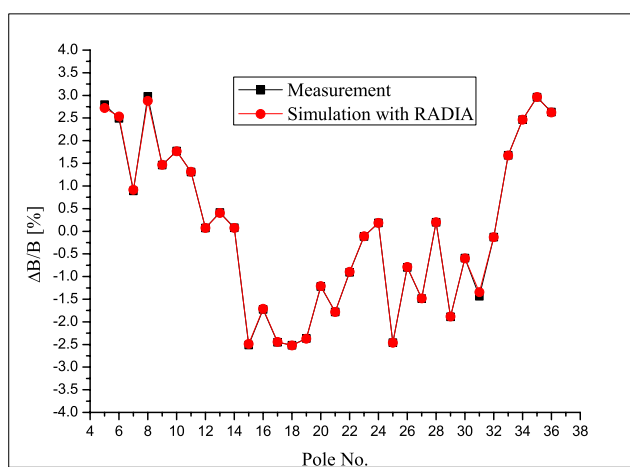


**Figure 7.25** Real magnetic field profiles as measured at an excitation current of 510 A and simulation with different current densities in the main coils corresponding to the field errors. The average field of the generated and measured magnetic fields are 1.3845 T and 1.387 T, respectively.

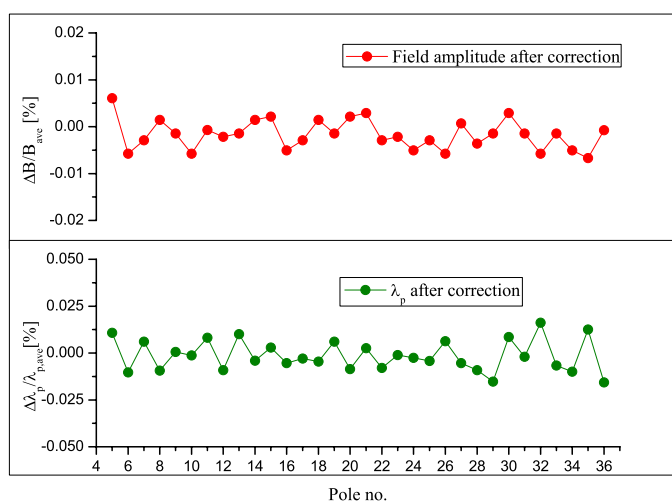
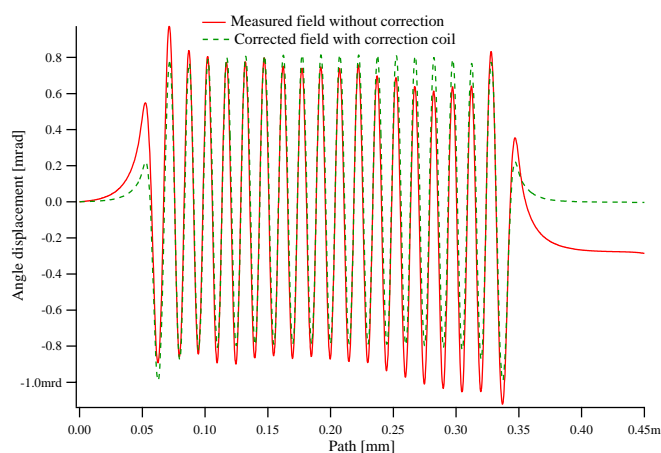
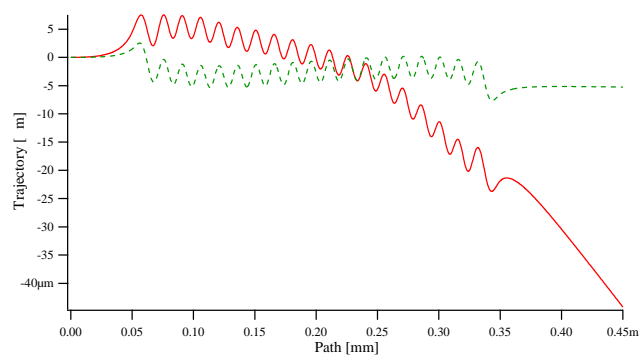


**Figure 7.26** Field (upper) and period length (bottom) errors normalized to a field of 1.387 T and 15.002 mm period length.



(a) Angle deviation



(b) Position deviation

**Figure 7.27** (upper) Angular deviation with (dashed) and without (solid) correction and (bottom) electron beam trajectory with (dashed) and without (solid) correction at 1.2 GeV.

through the undulator still exit with an angle and displacement from the beam axis. The actual effect on the closed orbit must be evaluated and possibly corrected by steering magnets before and after the undulator. By deviation of the first and second field integrals with the beam rigidity, the angle deviation and displacement of the electron beam at the end of the undulator after correction are  $1.59 \mu\text{rad}$  and  $1.58 \mu\text{m}$ , respectively. Comparisons of deviations in the angle and the position of the electron beam with and without correction are shown in Figure 7.27(b). With the field integrals we can calculate the angular flux density of photon beam with

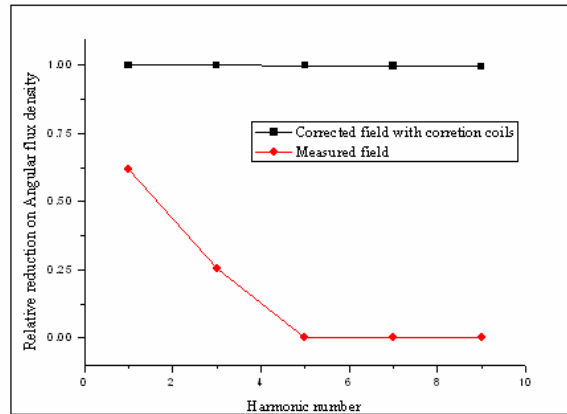


**Figure 7.28** Relative reduction of the angular photon flux density calculated with B2E for the measured field (dots) and corrected field with correction coils (squares).

the B2E code for the 1.2 GeV SIAM storage ring at all harmonics of the radiation. The most obvious reductions on the flux density occurs at the higher harmonics (5<sup>th</sup> up) because of phase and field errors on the real magnetic field as shown in Figure 7.28. The reduction is calculated by the ratio of the angular flux densities defined by

$$\text{Reduction} = \left( \frac{d^2 F}{d\theta d\psi} \right)_{B\text{-corrected}, B\text{-measured}} / \left( \frac{d^2 F}{d\theta d\psi} \right)_{B\text{-ideal}}$$

The quality of the undulator is greatly improved by the correction as evidenced by the significant increase in angular flux density especially at high harmonics. On the other hand, this method has the disadvantage of high cost and significant heat sources from many electrical connections to the cold mass.

## 7.4.2 Additional coils in the superconducting gap

The field changes strongly depend on the location of the trim coil and we try now to place the correction coil in the undulator gap as shown in Figure 7.29 and simulate this configuration with the code RADIA. The correction coil is assumed to have been made of wire with a diameter of 0.1 mm and energized with a current of

20 A. The correction coil active in the nominal gap of 5.6 mm produces a localized

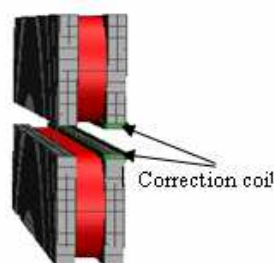


**Figure 7.29** Pole slice of superconducting undulator with correction coil placed in the gap. The diameter of the coil wire is 0.1 mm and the current feed through the coil is 20 A.

field change as shown in Figure 7.30. The field amplitude at the corrected pole (the 21<sup>st</sup> pole) is changed by about 0.07 T and field changes for neighboring poles are no more than 11 %. The field correction is thus very localized and all other field changes in the remaining undulator poles can be neglected. The correction coil at

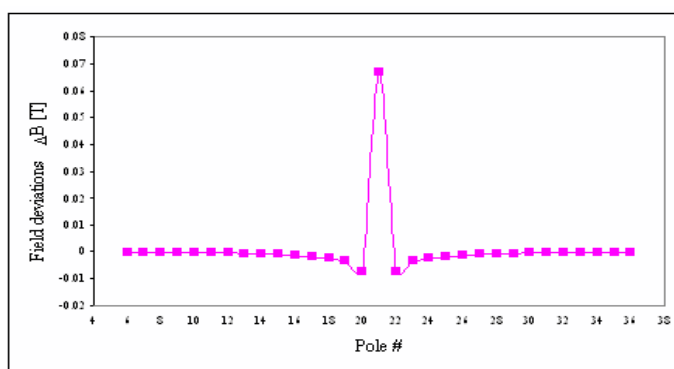


**Figure 7.30** Field changes caused by a correction coil in the undulator gap

this location in the gap provides also a very local correction of the period lengths making this method of a correction coil in the gap an effective way to compensate field errors. Because the correction coil is in the gap closed to the electron beam large field errors can be completely reduced. On the other hand, the cross-section

of the wire and number of turns are limited and should be adjusted to the actual correction needs. This technique may in some cases even not be practical because of the trim coil position in the gap. A major disadvantage for this method is the reduction on the nominal gap of 5.6 mm which causes a decrease of the beam stay clear so that the electron beam cannot survive in the storage ring. This negative effect can be minimized by using a very thin superconducting wire with high current densities. Simulation to correct the field errors follows also the same process as previously. To preserve the nominal gap at 5.6 mm, an air-core correction coil could be placed on the top of the undulator. The air-core correction coil has a diameter of 0.1 mm and is energized with a current of 30 A. This correction coil performs non-localized field corrections as shown in Figure 7.31. At the corrected

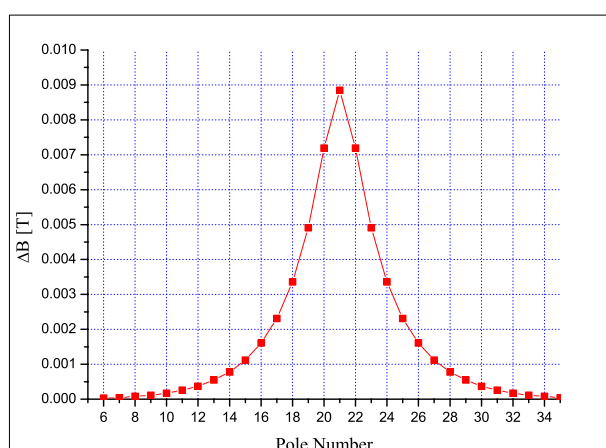


**Figure 7.31** Field deviations caused by a correction coil placed at the top of the pole surface. The total cross-section is  $0.1 \text{ mm}^2$  and the correction current is 30 A.

pole the change in field is about 0.0087 T and the effect on the field in neighboring poles is an almost equal 0.0072 T. Because the coil is placed far from the beam the change in the field amplitudes is small and to correct high field errors the current through the coil must be high which is not desirable especially in a cryogenic

environment. We need more practical correction concepts to achieve a reduction of field errors to less than 1 %.

## 7.5 Field correction by modification of the iron pole geometry

Besides using correction coils to compensate field errors of the superconducting undulator a new concept dealing with saturation in the iron of the undulator poles is proposed. This technique is based on a modification of the iron content in the poles. The poles in superconducting undulators are already partially saturated and are therefore sensitive to the iron content. Reversible variation of the iron content can be accomplished by varying making the poles hollow and then filling the hollows with adjustable amounts of iron pieces. For small corrections this could also be accomplished with ferromagnetic skews are inserted into the poles more or less. With this correction method we can only increase or decrease all fields. If the magnet is measured with hollow iron poles then adding iron would increase the field. Conversely, if the magnet is measured with full poles the field can be reduced by removing some iron. Once the exact relation of adding/removing iron and pole field change is known one can modify all poles to correct the field.

### 7.5.1 Simulation of iron content in the undulator pole

Modification of the iron content of undulator poles was simulated by the insertion of thick slits from the backside of the poles with a constant width ( $x$ ) and length ( $z$ ) but varying depth ( $y$ ) as shown in Figure 7.32. By implementing slits in the iron pole we create a localized field change depending the iron content in that pole. The field amplitude is reduced as shown in Figure 7.33. In simulations the slit depths at pole number 21 have been varied while the slit length is fixed at

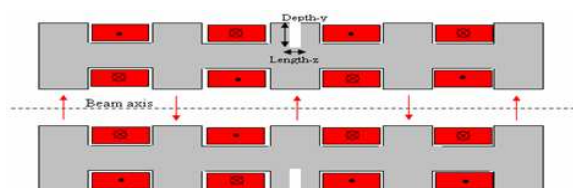


**Figure 7.32** Cross-section of the SCU15 with slit into backside of the poles for a pole length ( $z$ ) of 2.85 mm and pole width ( $x$ ) of 99.86 mm.

1.35 mm or 0.47 of the pole length. At the corrected pole the field amplitude is changed as a function of the slit height as shown in Figure 7.34.

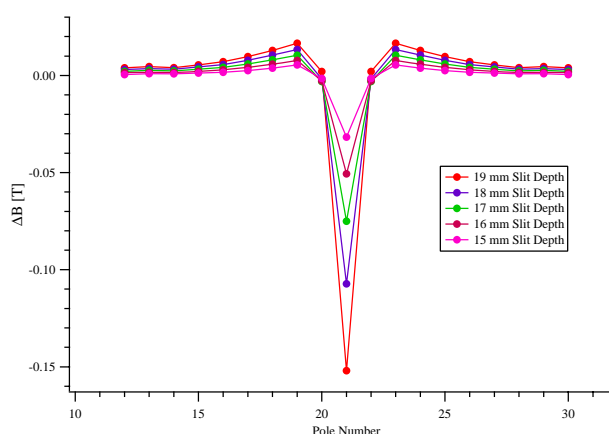


**Figure 7.33** Changes in field amplitude caused by implementing slits into undulator poles. The slit length is fixed at 1.35 mm while the height (depth) is varied.

The slit can be inserted into the undulator pole by taking some iron out from that pole. If we take out an iron piece with a height of 1 mm a depth of only 1 mm, the field amplitude at respective pole is increased about 0.0006 T. This increases the magnetic flux density at the corrected pole (with inserted slit), the field amplitude is actually increased. If however we remove more iron with a slit depth of 19 mm the field amplitude at the corrected pole is reduced by 0.152 T

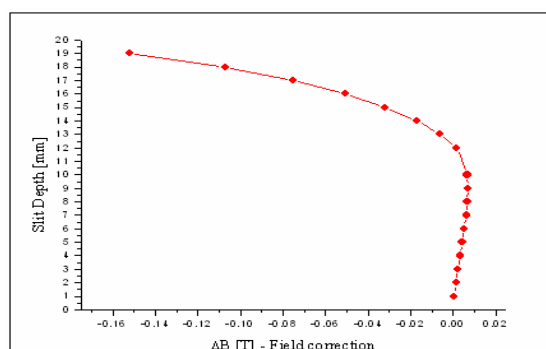


**Figure 7.34** Field changes at the corrected pole (the 21<sup>st</sup>) for different slit depths. Dots represent field amplitude changes calculated by POISSON.

because the iron content in the pole is significantly reduced for the main field which now has to pass through less iron cross section. Due to the reduced iron content in the pole saturation has been taken into account. The magnetic field strength at that pole is produced by the same current as in other poles but there is some modification on the pole geometry and the magnetic flux is redistributed into the remaining iron cross section. The field density in the remaining iron increases thus reducing the permeability and the field amplitude.

By varying the slit depths the field amplitudes change as shown in Figure 7.34. We use a cubic spline-interpolation to find the slit depths for any desired field amplitude correction  $\Delta B$ . Only the range from about 13 mm to 19 mm is of interest for correction and is shown in Figure 7.35. Corrections by removing iron can only lower the field and therefore the fields are corrected to the lowest value in the undulator. We can calculate the iron content for each pole to be corrected to reach a field amplitude of 1.3521 T. Different slit depths are implemented to modify the real field measured at 510 A. In practice the slit variations can be achieved by adding or removing flat iron of desired thickness. All iron pieces have the same length of 1.35 mm and width of 99.86 mm while the iron height is selected

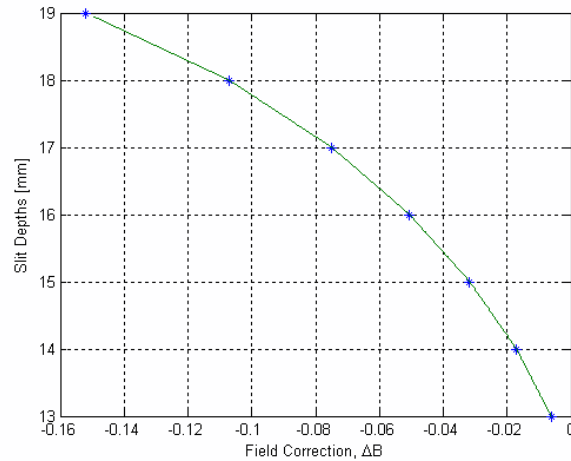


**Figure 7.35** Comparisons of slit depths in a range of about 13 mm to 19 mm related to the field changes between a simulation (stars) and interpolation (line).

to completely compensate the field errors. We can fill the iron content with the iron pieces corresponding to the field error at each undulator pole. Finally the assembly the undulator with different slit depths may be cooled down again to cryogenic temperature and we would expect that the fields will be corrected as expected from measurement and simulation. The actual dimensions of the iron pieces used here are not fundamental and could be chosen differently but of course the corrections depend on the dimensions used in simulations. The field amplitude changes with different slit depths have been checked both with the RADIA and POISSON code. Both simulated results at the pole number 21 agree well as shown in Figure 7.36. With the modification of the undulator poles (only main poles) as described, the fields can be improved with remaining r.m.s field error of only  $\sigma_{rms-B} = 0.0003\text{T}$  or 0.021 % of the peak field. The field changes  $\frac{\Delta B}{B_0}$  normalized to the ideal field amplitude with and without correction by adjusting the iron content in poles are shown for comparison in Figure 7.37. After iron content correction the average field amplitude is 1.3505 T.

This correction method also impacts the period length. Figure 7.38 shows

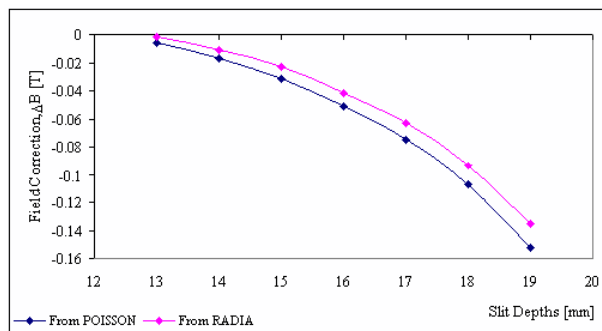


**Figure 7.36** Comparison of expected field corrections for various slit depths as calculated with RADIA (dots) and POISSON (dots).

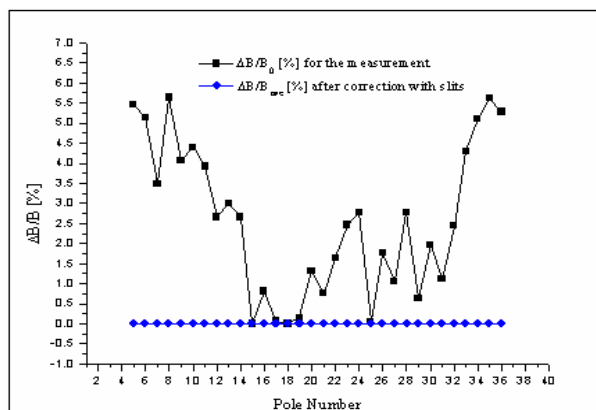


**Figure 7.37** Comparison of peak field deviations related to the average and minimum peak field of  $B_0 = 1.3505$  T and  $B_0 = 1.3521$  T with and without slit correction, respectively.

these changes normalized to the average period length. After the correction the average period length is reduced from 15.007 mm to 15.002 mm. Together with an improved field profile we also get a reduction in the phase errors to 0.024 %. Finally the first and second field integrals are calculated from the corrected magnetic field distribution. Since the end pole parameters are not perfectly designed in this prototype we do not achieve zero values in angle and position of the electron beam at the exit of the undulator. The first and second field integrals after slit

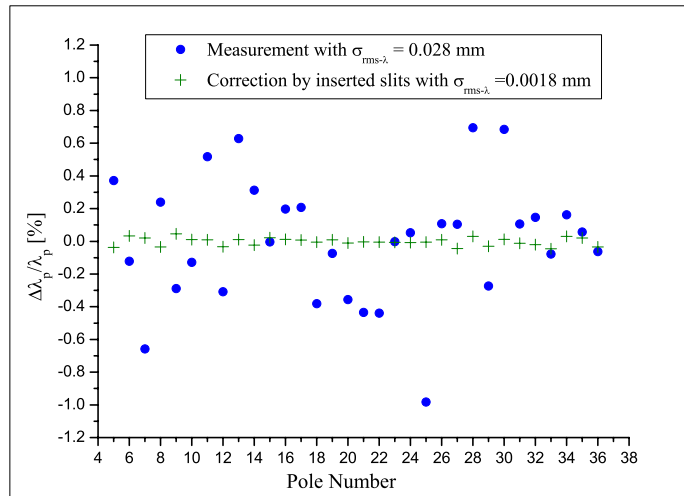


**Figure 7.38** The period length with and without field corrections by slits in the undulator poles. The average values of the period lengths before and after correction are 15.007 mm and 15.002 mm, respectively.

correction are very small being  $6.88 \times 10^{-6} T.m$  and  $6.85 \times 10^{-6} T.m^2$ , respectively. Division of the integrals by the beam rigidity the angular and position deviations of the electron beam at the undulator exit are  $1.72 \mu\text{rad}$  and  $1.71 \mu\text{m}$ , respectively for a 1.2 GeV beam. A comparison of the electron trajectory with and without correction is shown in Figure 7.39. After compensation of field errors by varying

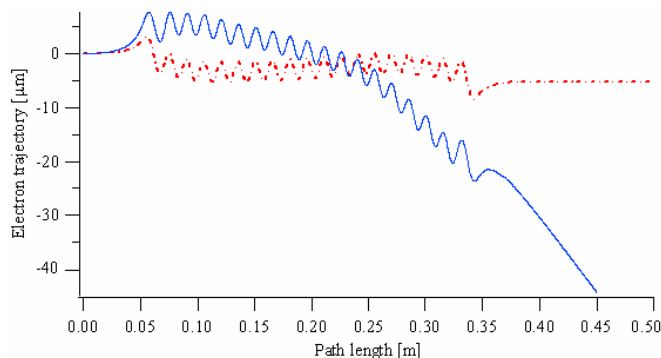


**Figure 7.39** Electron trajectory with and without field error correction with slits.

the saturation in the poles, angular photon flux densities in all harmonics up to

the 9<sup>th</sup> are increased significantly as shown in Figure 7.40. We can see clearly that this technique is a highly efficient correction method with small remaining field errors. The average field amplitude is reduced slightly to 1.3505 T after the correction which reduces slightly the photon energies. Of course, by increasing the main coil current this can be compensated again. To reach small field errors in a superconducting undulator was the goal of this Chapter. We do not need additional power supplies but require only one careful preparation of the undulator not unlike the shimming which is customary for permanent material undulators and is considered part of construction and quality control. After correction we may expect almost ideal angular flux densities as demonstrated in Figure 7.40. Using the slits to correct field error, the field can be improved to acceptable values

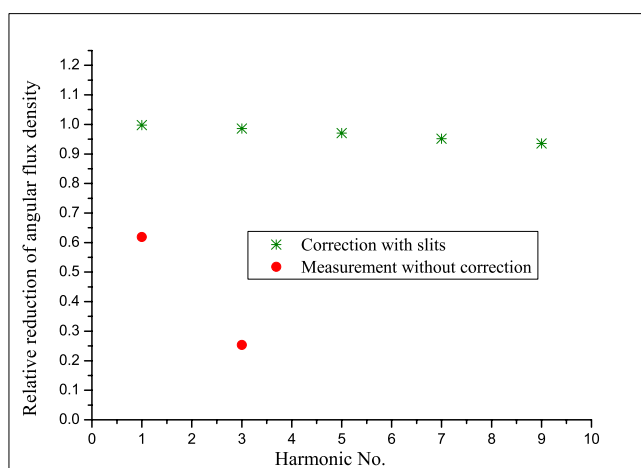


**Figure 7.40** Improvement of the angular flux density after slit correction in comparison to the uncorrected undulator.

with an enhancement of the angular photon flux density even at high harmonics. The correction process is somewhat complicated by the cryogenic requirements. The field distribution must be measured first, then the magnet must warm up for slit adjustments based on the measured fields. After correction the undulator will be cooled down again to 4.2 °K for field verification and experimental use. This

process is quite time consuming to obtain a good implementation of the field error correction and we need very precise predictions by simulations to correct the field error completely in one process.

### 7.5.2 Range of validity

The field correction by modification the iron pole is based on magnetic saturation in the iron and it is expected that this correction is useful only over a limit range in strength of the undulator. For much lower or much higher excitation we would expect the correction to lose its accuracy. Therefore, we have to determine the range of excitation permissible before the effect of field correction is lost again. In other words, we will now determine the range of validity or tunability of the undulator correction. Obviously, we would expect a reduction of tunability for low undulator strengths because there is no saturation at low fields and the correction is ineffective. Fortunately, this is not much of a concern for undulators which are designed for high photon energies in low energy storage rings. On the other hand there is a high field limit which is not very relevant since the undulator was designed for the highest field to begin with. We take the test undulator (SCU) and assume that we want to correct the field well enough to produce at least 90 % of the ideal photon beam brightness or angular flux density even at high harmonics up to 7<sup>th</sup> or 9<sup>th</sup>. At the 9<sup>th</sup> harmonic, for example, this would allow an r.m.s field error of no more than 0.8 %. Larger errors are allowed at lower harmonics. As discussed quantitatively in Chapter IV, the reduction of the angular flux density for the 5<sup>th</sup>, 7<sup>th</sup> and 9<sup>th</sup> harmonics is reduced by less than 10 % for ideal values if the r.m.s field errors are kept smaller than 1.0 %, 0.9 % and 0.8 %, respectively. To determine the range of excitation for which the field errors are within those limits, we use the undulator as corrected for a field of 1.35 T and then change the

excitation current in simulations in RADIA. By doing so, the field errors increase as shown in Figure 7.41. Here the r.m.s field errors are shown as a function of field excitation. Obviously, the errors are almost zero at the design field and increase as the field is increased or decreased. When these r.m.s errors reach the limits at 10 % photon flux density reduction we allow for each harmonic the end of the tuning range is reached. Acceptable ranges for the magnetic field in each harmonic in terms of undulator strength parameter  $K$  are:

$$0.91 < K < 2.55 \text{ for the } 5^{\text{th}} \text{ harmonic}$$

$$0.97 < K < 2.51 \text{ for the } 7^{\text{th}} \text{ harmonic}$$

$$1.02 < K < 2.44 \text{ for the } 9^{\text{th}} \text{ harmonic}$$

We note that there is a variation in the low field limits while the high field

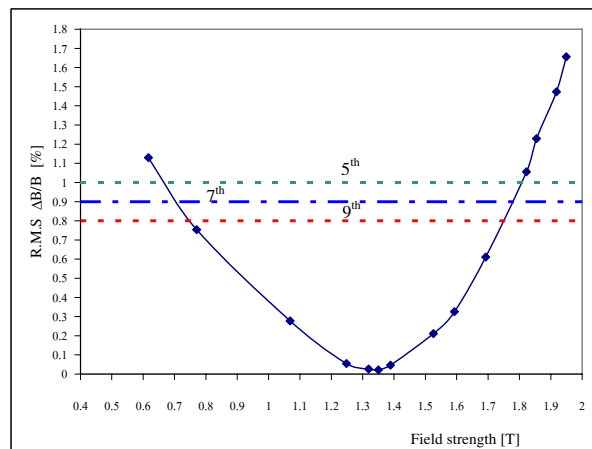


**Figure 7.41** Variation of r.m.s field errors and allowable r.m.s field errors as a function of field excitation for an undulator which has been corrected at a field of 1.35 T.

limitation vary little and are actual limited to the lowest value due to performance limitations in the superconducting wires. The ideal photon beam brightness or angular flux density is calculated with code SYNRAD (Wiedemann, 2002) and

B2E, respectively up to 9<sup>th</sup> harmonic by varying the K parameter within the limits just determined for each harmonic. Figure 7.42 shows the ideal brightness (a) and the angular flux density (b) of the radiation for the ideal undulator while the actual brightness and flux density for the corrected undulator would be within 90 % of these values. As a special result of this study, we find that the tunability is not much reduced due to the field correction applied and radiation from different harmonics overlap well thus allowing continuous scanning of photon energies for example, for spectroscopy. To achieve a perfect undulator with high brightness (and

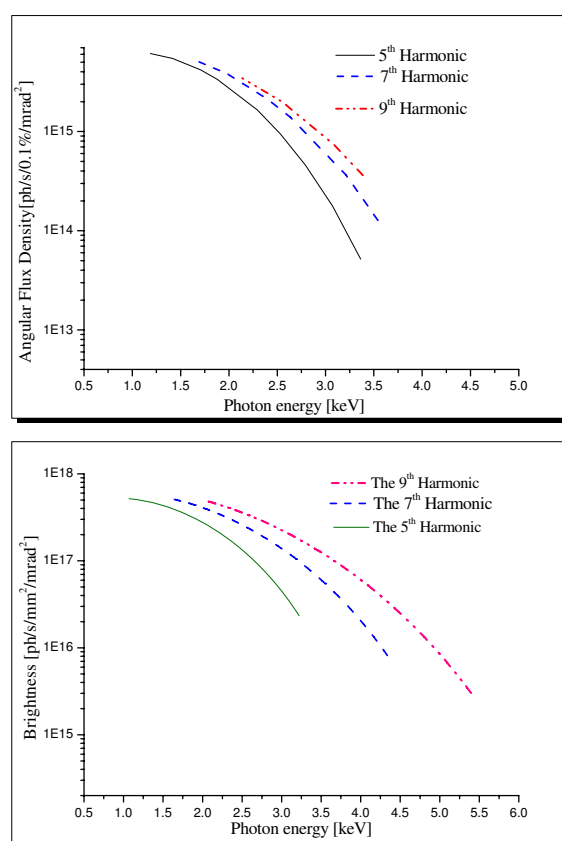


**Figure 7.42** Angular flux density (upper) and brightness (below) of photon radiation emitted from a superconducting undulator with field errors corrected in the SPS 1.2 GeV storage ring. The undulator parameter K is varied within acceptable limits as discussed in the text.

angular flux density) at each harmonic for the SPS ring which has electron beam parameter listed in 2.3, the r.m.s field errors should not exceed the permissible limits. Since some photon energy ranges have overlapped region of the brightness and the flux density, both brightness and flux density can be properly added up resulting in a wide photon energy range for users. It means that this correction technique can be used to compensate field errors of undulators with field range from 0.65 to 1.82 T, 0.69 to 1.79 T and 0.735 to 1.74 T with acceptable limitation of the angular flux density at the 5<sup>th</sup>, 7<sup>th</sup> and 9<sup>th</sup>, respectively.

Classical shimming by using iron pieces for a superconducting undulator can be only used to correct field errors not bigger than 0.5 % due to a strong influence of the shimming on neighboring poles. In this thesis, the superconducting undulator has a r.m.s field error of 1.8 % normalized to an average field amplitude of 1.387 T. Therefore, correction techniques by correction coils and modification of the undulator poles have been proposed and this efficacy has been described and discussed. We trust simulation results of the correction techniques because both theoretical explanation and experimented of the measurement shimming technique agree together. As simulation results show both correction coils and slits have a high potential for corrections of the field errors. A maximum current (current density) energized through the correction coil is 20.43 A (2050 A/mm<sup>2</sup>) limited by the critical current of the superconducting wire material NbTi. Thus a maximum correction fields change is about 0.040 T or 2.9 % normalized to the average field amplitude. With correction coils any sign of field errors can be corrected by selecting the direction of the current through the correction coils. To increase the field amplitude the correction should be energized by a current which has the same direction as in the undulator coil while the field is reduced if the current in the correction coil flows in the opposite direction. Use of correction coils is a quite flexible technique to adjust field amplitudes, however it has a significant and

electrical overheating. To correct the errors by slits or modification of geometry of the undulator pole the field amplitudes are only reduced because of a saturation in iron poles. However, increased field amplitude occurs only for small slits outside of the return yokes. This is force additional magnetic flux into the iron pole thus increasing the field strength. The increase of the field is only 0.005 T maximum and therefore is insignificant. We do not use this increase of the field amplitude. Cutting the slits deeper will reduce the field as shown in Figure 7.32. Because of the finite permeability in the low carbon iron (0.06 % in our case) saturation has been taken into account. The field amplitude at the pole with deep slits is reduced while the magnetic flux density is increased. A relative of angular flux density of the photon beam normalized to ideal values with correction coils and slits to correct field errors is shown in Figure 7.43. Both techniques have high potential for corrections of the field errors because the flux density even at the 9<sup>th</sup> harmonic is within 10 % of the ideal flux density. By the field correction, period length (or phase) errors are compensated automatically. The r.m.s field errors  $\sigma_{r.m.s-B}$  (field

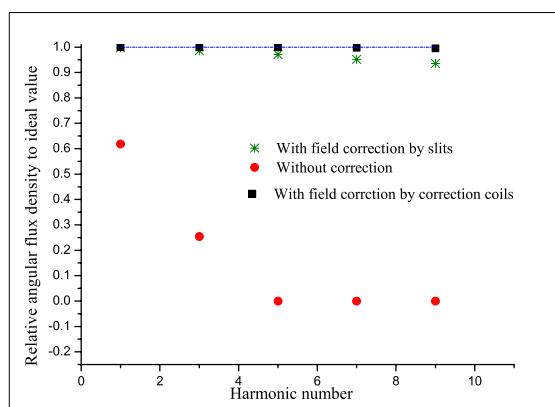


**Figure 7.43** Angular flux density relative to ideal (dash line) expectations in the forward direction for a measured field (dots), corrected field with correction coils (squares) and corrected field with slits (stars).

error normalized to the average value) after correction with correction coils and slits are 0.00005 T (0.0036 %) and 0.0003 T (0.021 %), respectively. The r.m.s period length errors  $\sigma_{r.m.s-\lambda}$  are 0.0013 mm (0.017 %) and 0.0018 mm (0.024 %), respectively. Average peak field amplitudes are 1.387 T with the correction coil technique while the modification of the pole gives the average field amplitude of 1.350 T demonstrating that we do not have to accept a significant reduction in field in lieu of correction.

## CHAPTER VIII

### CONCLUSIONS

The use of undulator magnets in low energy storage rings like the 1.2 GeV SIAM Photon Source (SPS) is limited in its ability to produce high energy photons. Short undulator period are desired for the generation of short wavelength photons. However, the period length is limited by the need to provide sufficient aperture for the electron beam. Reducing the period length to and below the gap height results in dramatic loss of field strength. Higher photon energies could be obtained at higher harmonics, which is only possible if the undulator strength is sufficiently high. Superconducting magnet technology seems to be the way to ameliorate these problems. Higher fields can be expected even for short period length and acceptable gap height.

In this thesis we discussed and studied the problems surrounding a superconducting undulator to produce short wavelength radiation from low energy storage rings. It is especially desirable to generate high harmonic radiation up to 7<sup>th</sup> or 9<sup>th</sup> order. The angular photon flux densities at such high harmonics is severely reduced by even small manufacturing imperfections in the magnetic field and periodicity of the undulator. Such imperfections are also apparent in conventional permanent material undulators, but can be corrected by applying thin ferromagnetic shims at specific locations along the array of magnet poles. This distribution is guided by instant magnetic measurements and control. Unfortunately, this cannot be done in superconducting undulators because of the limited access into a cryogenic environment. We have discussed in this thesis a variety of methods, each with its own advantages and disadvantages, which could be used to prepare a magnetically

corrected undulator at room temperature after first measuring the magnetic field in the cryostat. This is possible only if we can devise correction methods which are predictable. Among the correction methods discussed, the most promising seems to be one that modifies the magnetic saturation in each magnetic pole. Each magnetic pole is hollowed out and then backfilled with ferromagnetic iron such that the desired magnetic field is achieved. This method works quite locally with only small perturbations in neighboring poles. The correction in each pole is generally influenced by all corrections in all poles. A matrix can be established relating the amount of iron to be added or subtracted from a pole to the magnetic field change in each poles. A matrix inversion with SVD gives the change in iron content per pole as a function of the desired field correction. Simulations of this procedure show excellent results which restore the angular photon flux at high harmonics from noise level to more than 90 % of ideal values. We gained confidence in the simulations by comparison with measurements although not for this exact correction methods. To compare simulations with measurements for this variation of iron content would be desirable, but the high expense of cryogenic experimentation kept this so far only a goal. Applying this correction scheme to a real superconducting undulator we could imagine an undulator with 200 periods or a total length of 3 m to be installed in the 1.2 GeV SIAM Photon Source. Such an undulator is expected to produce high brightness radiation up and beyond some 3.5 keV at the 9<sup>th</sup> harmonics as shown in Figure 8.1. Higher harmonics may be possible.

The correction of the undulator is based on saturation characteristics and is therefore limited in its application. On the low field end the correction does not work because there is no saturation. This is of no practical consequence because this mode of operation does not allow the generation of higher harmonics. On the very high field end the saturation conditions are much different from that present when the corrections were done. This also is of no practical impact because we

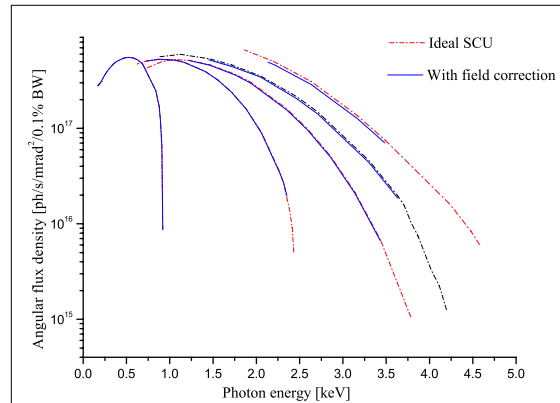


**Figure 8.1** A comparison of angular flux density emitted from an ideal (dotted line) and from actual SCU with field correction (solid line) consisting of 200 periods in the 1.2 GeV SPS storage ring.

**Table 8.1** Tunability range of field strength for an actual SCU

Harmonic no.	Field strength [T]	$K$ parameter
1	0.48 - 1.92	0.67 - 2.60
3	0.57 - 1.87	0.80 - 2.62
5	0.65 - 1.82	0.91 - 2.55
7	0.69 - 1.79	0.97 - 2.51
9	0.73 - 1.74	1.02 - 2.44

already push for the highest magnetic fields possible within the limitations of superconducting technology which, for example, limits the current density in the excitation coils. We therefore retain almost all the tunability of the undulator with the correction method employed. Figure 8.1 includes that tunability where we have assumed that the angular photon flux density should be at least 90 % of ideal. The range of undulator strengths for these limits are given in Table 8.1. Obviously, there is a significant change in the strength limits at low fields because decreasing harmonics are less and less sensitive to field errors. On the

high field side the limits are practically all the same as we would expect. The most urgent continuing study on this subject would be the actual construction of a superconducting undulator which allows the implementation of the iron content correction scheme as discussed. After measuring the raw magnet field corrections should be applied and the magnetic field should be measured again.

## REFERENCES



## REFERENCES

- Bardeen, J., Cooper, L. N., and Schrieffer, J. R. (1957). Theory of Superconductivity. **Phys. Rev.** 108(5): 1175–1204.
- Bennemann, K. H. (1996). **Superconductivity conventional and unconventional superconductors**. Springer.
- Brazi, E. (1998). Short sample measuring techniques. **Td-98-014**.
- CERN Accelerator school ( 1992-2005). Magnetic field measurement and alignment. **Report-CERN 92-05**.
- Chavanne, J., Elleaume, P., and Van Vaerenbergh, P. (1998). The ESRF Insertion Devices. **Journal of Synchrotron Radiation.** 5(3): 196–201.
- Chubar, O., Benabderrahmane, C., and Marcouille, O. (2004). Application of finite volume integral approach to computing of 3D magnetic fields created by distributed iron-dominated electromagnetic structure. **The 6th European Particle Accelerator Conference, EPAC04** .
- Chubar, O., Elleaume, P., and Chavanne, J. (1998). A three-dimensional magnetostatics computer code for insertion devices. **Journal of Synchrotron Radiation.** 5(3): 481–484.
- Clarke, A. J. (2004). **The science and technology of undulators and wigglers** (1st ed). Oxford University Press.

- Elder, F. R., Gurewitsch, A. M., Langmuir, R. V., and Pollock, H. C. (1947). Radiation from electron in a synchrotron. **Phys. Rev.** 71: 829–830.
- Elleaume, P. and Onuki, H. (2003). **Undulators, Wigglers and Their Applications**. Taylor and Francis Inc.
- Elleume, P., Chubar, O., and Chavanne, J. (1997). Computing 3D magnetic fields from insertion devices. **Particle Accelerator Conference, PAC97**: 3509–3511.
- Elleume, P. and Marechal, X. (1991). B2E, A software to compute synchrotron radiation from magnetic field data. **ESRF-SR/ID-91-54**.
- Farge, Y. (1980). Emission of photons by undulators. **Applied Optics**. 19: 4021–4026.
- Gilbert, S. (1988). **Linear Algebra and Its Applications** (3rd ed.). Brooks Cole.
- Grote, G. and Iselin, F. C. (1991). Experience with mad8 on cray, ibm, and apollo dn-10000 at cern. **CERN-SL-90-124-AP**.
- Grote, H. and Iselin, C. (1995). The MAD program. **CERN/SL/90-13**.
- Hwang, C. S., Jan, J. C., Lin, P. H., and Chang, C. H. (2006). Mini-pole superconducting undulator for X-ray synchrotron light source. **IEEE Transaction on applied superconductivity** 16: 1855–1858.
- Hwang, C. S., Lin, F. Y., and Fan, T. (2003). Integral magnetic field measurement using an automatic fast long-loop-flip coil system. **IEEE Trans. Inst. and Meas.** 52: 865–870.

- James, A. C. (2004). **The Science and technology of undulators and wigglers** (1st ed). Oxford University Press.
- Jan, J., Hwang, C. S., Lin, F. Y., Chang, C. H., Lin, P. H., and Chunjarean, S. (2009). Design of field trimming by iron pieces and coils for the superconducting undulator. **Applied Superconductivity Conference, ASC09** .
- Jan, J. C., Hwang, C. S., and Lin, P. H. (2008). Design and improvement of a Mini-pole superconducting undulator at NSRRC. **IEEE Trans. on applied superconductivity** 18: 427–430.
- Kim, K. J. (1986). Brightness, coherence, and propagation characteristics of synchrotron radiation. **Nucl. Instrum. Methods Phys. Res.A** 246: 71–76.
- Kwankasem, C. (2007). Design parameters for the Low emittance mode at 1.2 GeV SPS storage ring. **NSRC-TN-2007/02**.
- Mikkonen, R. (1996). A 6 T Superconducting wiggler for synchrotron radiation. **IEEE Trans. Magn.** 32: 2617–2620.
- Mikkonen, R. (1999). Philosophy of a quench; Two case studies-LTS wiggler magnet and HTS  $\mu$ -SMES. **IEEE Trans. Magn.** 2: 596–599.
- Nishijima, G., Okamura, T., Kabashima, S., Kurusu, T., and Yasawa, T. (1997). Magnetic stability of AC superconducting wire in self field. **IEEE Trans. on applied superconductivity** 7: 778–781.
- Peter, J. L. (1999). Abridged metallurgy of ductile alloy superconductors. **Wiley Encyclopedia of. Electrical and Electronics Engineering.** 21: 75–87.

- Preston, D. W. (1991). The art of experimental physics. **Report-CERN 92-05**.
- Sebek, J. (2009). Singular Value Decomposition lecture. **Lecture note**.
- Smith, P. F. (1963). Protection of superconducting coils. **Review of Scientific Instruments**. 34: 368–373.
- Soderlund, L. (1998). Design of a Three pole Superconducting Planar Wiggler. (Master dissertation, Department of Electrical Engineering, Tampere University of Finland).
- Swatloski, T. L. (1993). Graphical user interface for AMOS and POISSON. **CAP93/CA 71**: 22–26.
- Tinkham, M. (1996). **Introduction to superconductivity**. McGraw-Hill Book Co.
- Tortschanoff, T. (1984). Survey of numerical methods in field calculation. **INTERMAG Conf**.
- Wallen, E. (1998). Commissioning of a 6.4 T Superconducting Wavelength Shifter at Max-Lab. **Nucl. Instr. and Meth.A** 495: 58–64.
- Wiedemann, H. (1998). **Particle Accelerator Physics II**: 64.
- Wiedemann, H. (2002). Private communication.
- Wiedemann, H. (2007). **Particle Accelerator Physics**. (3rd ed.) Springer.
- William, H. P. (2007). **Numerical Recipes** (3rd ed.). Cambridge University Press.
- Wilson, M. (1983). **Superconducting Magnets**. Oxford University Press.

Wollmann, D. (2008). A novel concept for phase error correction in superconductive undulators. (Docteral dissertation, University of Karlsruhe, Germany).

# CURRICULUM VITAE

**NAME** Miss Somjai Chunjarean  
**DATE OF BIRTH** April 26, 1977  
**PLACE OF BIRTH** Uttaradit, Thailand  
**PERSONAL ADDRESS** 36, Tha-it Sub-district,  
Muang district, Uttaradit 53000, Thailand  
Mobile. 66-81-5303922  
**E-MAIL** pae055@hotmail.com, chunjarean@gmail.com

## EDUCATIONS

Degree of Doctor of Philosophy (2006 - present)

School of Physics, Suranaree University of Technology, Nakhon Ratchasima,  
Thailand

Title of Thesis: High field insertion devices for low energy electron storage  
rings

Supervisors: Prof. Dr. Helmut Wiedemann and Dr. Saroj Rujirawat

Master of Science (1998 - 2001)

School of Physics, Chiang Mai University, Chiang Mai, Thailand

Supervisors: Assoc. Prof. Dr Somsorn Singkarat and Dr. Somsak Dangtip

Bachelor of Science (1995 - 1998)

Department of Physics, Chiang Mai University, Chiang Mai, Thailand

Supervisor: Assoc. Prof. Dr Nara Jirapatpimon